

**DEVELOPMENT OF A GUIDELINE FOR
ESTIMATING TSUNAMI FORCES ON
BRIDGE SUPERSTRUCTURES**

Final Report

SR 500-342

DEVELOPMENT OF A GUIDELINE FOR ESTIMATING TSUNAMI FORCES ON BRIDGE SUPERSTRUCTURES

Final Report

SR 500-340

by

Solomon C. Yim
Sutaporn Boon-intra
Seshu B. Nimmala
Holly M. Winston
Mohsen Azadbakht
Kwok Fai Cheung

for

Oregon Department of Transportation
Research Section
200 Hawthorne Ave. SE, Suite B-240
Salem OR 97301-5192

October 2011

1. Report No. OR-RD-12-03		2. Government Accession No.		3. Recipient's Catalog No.	
4. Title and Subtitle Development Of A Guideline For Estimating Tsunami Forces On Bridge Superstructures				5. Report Date October 2011	
				6. Performing Organization Code	
7. Author(s) Solomon C. Yim, Sutaporn Boon-intra, Seshu B. Nimmala, Holly M. Winston, Mohsen Azadbakht, and Kwok Fai Cheung				8. Performing Organization Report No.	
9. Performing Organization Name and Address Oregon State University and University of Hawaii School of Civil & Construction. Eng. Dept. of Ocean & Resource Eng. 350 Owen Hall 2540 Dole Street, Holmes Hall 402 Corvallis, OR 97331-3212 Honolulu, HI 96822				10. Work Unit No. (TRAIS)	
				11. Contract or Grant No. SR 500-340	
12. Sponsoring Agency Name and Address Oregon Department of Transportation Research Section 200 Hawthorne Ave. SE, Suite B-240 Salem, OR 97301-5192				13. Type of Report and Period Covered Final Report	
				14. Sponsoring Agency Code	
15. Supplementary Notes					
16. Abstract The Pacific Northwest is vulnerable to seismic events in the Cascadia Subduction Zone (CSZ) that could generate a large tsunami that could devastate coastal infrastructure such as bridges. In this context, this paper describes the development of a guideline for estimating tsunami forces on bridge superstructures along the Oregon Coast. A multi-physics based numerical code is used to perform numerical modeling of tsunami impact on full-scaled bridge superstructures of four selected bridges – Schooner Creek Bridge, Drift Creek Bridge, Millport Slough Bridge, and Siletz River Bridge – located on Highway 101 in the Siletz Bay area on the Oregon Coast. Two different types of bridge superstructure, deck-girder and box sections, are developed in the case of the Schooner Creek Bridge to study the effect of geometry of bridge cross-section. The results show that tsunami forces on box section superstructures are significantly higher than the forces on deck-girder sections; therefore, the box section design might not be appropriate to be used in a tsunami run-up zone. Moreover, numerical simulation of a deck-girder bridge with rigid rails and with open rail spacing, subjected to identical tsunami loads, was performed to examine the effect of rails on tsunami forces. The results suggested that horizontal and vertical tsunami forces on bridges with rails are larger than those on bridges with open rail spacing, up to 20% and 15%, respectively. These numerical results are finally incorporated into the mathematical formulations from the existing literature to develop a simplified method for estimating tsunami forces on bridge superstructures. Appropriate empirical coefficients for bridge superstructures under tsunami loads were evaluated based on an average value of the scattering data from the numerical results. The developed guideline is intended to be used as a preliminary guidance for design only as it did not account for uncertainties; thus, an appropriate load factor must be included in the calculations. A previous analysis of tsunami forces on the Spencer Creek Bridge on the Oregon Coast is revisited to examine the applicability of the guideline developed in the present work. This paper also presents the results of a study on the optimal number of CPUs for running fluid-structure interaction (FSI) numerical models of bridge superstructures using LS-DYNA on high-performance computing (HPC) systems.					
17. Key Words bridges, tsunami, forces, model			18. Distribution Statement Copies available from NTIS, and online at http://www.oregon.gov/ODOT/TD/TP_RES/		
19. Security Classification (of this report) Unclassified		20. Security Classification (of this page) Unclassified		21. No. of Pages 146	22. Price

SI* (MODERN METRIC) CONVERSION FACTORS

APPROXIMATE CONVERSIONS TO SI UNITS					APPROXIMATE CONVERSIONS FROM SI UNITS				
Symbol	When You Know	Multiply By	To Find	Symbol	Symbol	When You Know	Multiply By	To Find	Symbol
<u>LENGTH</u>					<u>LENGTH</u>				
in	inches	25.4	millimeters	mm	mm	millimeters	0.039	inches	in
ft	feet	0.305	meters	m	m	meters	3.28	feet	ft
yd	yards	0.914	meters	m	m	meters	1.09	yards	yd
mi	miles	1.61	kilometers	km	km	kilometers	0.621	miles	mi
<u>AREA</u>					<u>AREA</u>				
in ²	square inches	645.2	millimeters squared	mm ²	mm ²	millimeters squared	0.0016	square inches	in ²
ft ²	square feet	0.093	meters squared	m ²	m ²	meters squared	10.764	square feet	ft ²
yd ²	square yards	0.836	meters squared	m ²	m ²	meters squared	1.196	square yards	yd ²
ac	acres	0.405	hectares	ha	ha	hectares	2.47	acres	ac
mi ²	square miles	2.59	kilometers squared	km ²	km ²	kilometers squared	0.386	square miles	mi ²
<u>VOLUME</u>					<u>VOLUME</u>				
fl oz	fluid ounces	29.57	milliliters	ml	ml	milliliters	0.034	fluid ounces	fl oz
gal	gallons	3.785	liters	L	L	liters	0.264	gallons	gal
ft ³	cubic feet	0.028	meters cubed	m ³	m ³	meters cubed	35.315	cubic feet	ft ³
yd ³	cubic yards	0.765	meters cubed	m ³	m ³	meters cubed	1.308	cubic yards	yd ³
NOTE: Volumes greater than 1000 L shall be shown in m ³ .									
<u>MASS</u>					<u>MASS</u>				
oz	ounces	28.35	grams	g	g	grams	0.035	ounces	oz
lb	pounds	0.454	kilograms	kg	kg	kilograms	2.205	pounds	lb
T	short tons (2000 lb)	0.907	megagrams	Mg	Mg	megagrams	1.102	short tons (2000 lb)	T
<u>TEMPERATURE (exact)</u>					<u>TEMPERATURE (exact)</u>				
°F	Fahrenheit	(F-32)/1.8	Celsius	°C	°C	Celsius	1.8C+32	Fahrenheit	°F

*SI is the symbol for the International System of Measurement

DISCLAIMER

This document is disseminated under the sponsorship of the Oregon Department of Transportation and the United States Department of Transportation in the interest of information exchange. The State of Oregon and the United States Government assume no liability of its contents or use thereof.

The contents of this report reflect the view of the authors who are solely responsible for the facts and accuracy of the material presented. The contents do not necessarily reflect the official views of the Oregon Department of Transportation or the United States Department of Transportation.

The State of Oregon and the United States Government do not endorse products of manufacturers. Trademarks or manufacturers' names appear herein only because they are considered essential to the object of this document.

This report does not constitute a standard, specification, or regulation.

TABLE OF CONTENTS

1.0	ABSTRACT.....	V
2.0	INTRODUCTION.....	3
2.1	BACKGROUND.....	3
2.2	RUPTURE MODELS AND TSUNAMI SCENARIOS.....	4
3.0	LITERATURE REVIEW	7
3.1	WAVE FORCES EQUATIONS.....	7
3.1.1	<i>Wave Forces on Decks of Offshore Platforms.....</i>	<i>7</i>
3.1.2	<i>Wave Forces on Bridge Decks.....</i>	<i>7</i>
3.2	LITERATURE OF TSUNAMI FORCES.....	8
3.2.1	<i>Guidelines for Design of Structures for Vertical Evacuation from Tsunamis.....</i>	<i>8</i>
3.2.2	<i>Performance-Based Tsunami Engineering.....</i>	<i>8</i>
3.3	SUMMARY OF LITERATURE REVIEW	8
4.0	NUMERICAL MODELS OF TSUNAMI IMPACT LOAD ON BRIDGE SUPERSTRUCTURES.....	11
4.1	MODEL DESCRIPTION.....	11
4.2	BRIDGE DESCRIPTIONS AND TSUNAMI FLOW FIELDS.....	12
4.3	TSUNAMI FORCE TIME-HISTORIES	13
4.4	EFFECT OF CROSS-SECTIONAL BRIDGE GEOMETRY.....	15
4.5	EFFECT OF RAILS	19
4.6	CUMULATIVE PROBABILITY OF MAXIMUM TSUNAMI FORCES	29
4.7	COMPUTATIONAL EFFORTS	30
5.0	ESTIMATION OF TSUNAMI FORCES ON BRIDGE SUPERSTRUCTURES	35
5.1	HORIZONTAL FORCES	35
5.2	VERTICAL FORCES.....	37
5.3	DISCUSSION AND LIMITATION OF RECOMMENDED APPROACH.....	38
6.0	CASE STUDY OF THE SPENCER CREEK BRIDGE – REVISITED.....	43
7.0	ACCURACY COMPARISON OF THE RECOMMENDED APPROACH WITH OTHER EXISTING METHODS.....	45
8.0	COMPUTATIONAL PERFORMANCE.....	49
9.0	CONCLUDING REMARKS	53
10.0	FUTURE RESEARCH.....	55
11.0	REFERENCES.....	1

APPENDIX A: SIMULATION MODELS

APPENDIX B: TSUNAMI TIME-HISTORY FORCES OF THE SELECTED BRIDGE SUPERSTRUCTURES

APPENDIX C: EXAMPLE CALCULATIONS OF TSUNAMI FORCES ON BRIDGE SUPERSTRUCTURE

APPENDIX D: A CASE STUDY OF SPENCER CREEK BRIDGE, OREGON – REVISITED

APPENDIX E: DRAWING OF SELECTED BRIDGES

APPENDIX F: MODELING OF 500-YEAR CASCADIA TSUNAMIS AND INUNDATION AT SILETZ BAY, OREGON

LIST OF TABLES

Table 4.1: Maximum forces and moments due to tsunami loads on superstructure of Schooner Creek Bridge 14

Table 4.2: Maximum forces and moments due to tsunamis on Drift Creek Bridge (with rigid rails) 15

Table 4.3: Maximum forces and moments due to tsunamis on superstructure of Millport Slough Bridge (including rails)..... 15

Table 4.4: Joint Probability of Rupture Scenarios (Cheung et al. 2011) 30

Table 4.5: Computational efforts for performing the simulation models 31

Table 7.1: Maximum values of horizontal forces on the Schooner Creek Bridge due to different tsunami scenarios 45

Table 7.2: Maximum values of vertical forces on the Schooner Creek Bridge due to different tsunami scenarios 45

Table 7.3: Maximum values of horizontal forces on the Millport Slough Bridge due to different tsunami scenarios 46

Table 7.4: Maximum values of vertical forces on the Millport Slough Bridge due to different tsunami scenarios 46

Table 7.5: Maximum values of horizontal forces on the Drift Creek Bridge due to different tsunami scenarios 46

Table 7.6: Maximum values of vertical forces on the Drift Creek Bridge due to different tsunami scenarios 46

Table 7.7: Maximum values of horizontal and vertical forces on the Spencer Creek Bridge 46

Table 7.8: Computed relative error of horizontal forces on the Schooner Creek Bridge for different methods 47

Table 7.9: Computed relative error of vertical forces on the Schooner Creek Bridge for different methods..... 47

Table 7.10: Computed relative error of horizontal forces on the Millport Slough Bridge for different methods 47

Table 7.11: Computed relative error of vertical forces on the Millport Slough Bridge for different methods..... 47

Table 7.12: Computed relative error of horizontal forces on the Drift Creek Bridge for different methods..... 47

Table 7.13: Computed relative error of vertical forces on the Drift Creek Bridge for different methods..... 48

Table 7.14: Computed relative error of horizontal and vertical forces on the Spencer Creek Bridge..... 48

Table 8.1: Summary of computational time 50

LIST OF FIGURES

Figure 2.1: Top view map of Siletz bay area and location of the selected bridges	4
Figure 2.2: Boundaries of Cascadia Subduction zone inferred from the National Seismic Hazard Map (2008) black line: locked Zone (LZ), yellow line: Midpoint of the Transition zone (MT), pink line: Transition Zone (TZ), blue line: Global Analog (GA).....	5
Figure 4.1: An example of numerical model of Millport Slough Bridge	12
Figure 4.2: Comparisons of numerical prediction of horizontal tsunami force (lb/in) time-history for different bridge geometry	16
Figure 4.3: Comparisons of numerical prediction of vertical tsunami force (lb/in) time-history for different bridge geometry	17
Figure 4.4: Comparisons of numerical prediction of overturning moment (kip-ft/ft) time-history for different bridge geometry	18
Figure 4.5: Time-Histories of numerical prediction of horizontal tsunami force (lb/in) for Schooner Creek Bridge (Deck-Girder)	20
Figure 4.6: Time-Histories of numerical prediction of vertical tsunami force (lb/in) for Schooner Creek Bridge (Deck-Girder)	21
Figure 4.7: Time-Histories of numerical prediction of overturning moment (kip-ft/ft) for Schooner Creek Bridge (Deck-Girder)	22
Figure 4.8: Time-Histories of numerical prediction of horizontal tsunami force (lb/in) for Drift Creek Bridge	23
Figure 4.9: Time-Histories of numerical prediction of vertical tsunami force (lb/in) for Drift Creek Bridge	24
Figure 4.10: Time-Histories of numerical prediction of overturning moment (kip-ft/ft) for Drift Creek Bridge	25
Figure 4.11: Time-Histories of numerical prediction of horizontal tsunami force (lb/in) for Millport Slough Bridge	26
Figure 4.12: Time-Histories of numerical prediction of vertical tsunami force (lb/in) for Millport Slough Bridge	27
Figure 4.13: Time-Histories of numerical prediction of overturning moment (kip-ft/ft) for Millport Slough Bridge	28
Figure 4.14: Water elevation time-histories at Siletz River Bridge.....	29
Figure 4.15: Cumulative probability of Maximum Horizontal Tsunami Force.....	32
Figure 4.16: Cumulative probability of Maximum Vertical Tsunami Force.....	32
Figure 4.17: Cumulative probability of Maximum Overturning Moment due to Tsunamis	33
Figure 4.18: Correlation between maximum flux momentums and maximum predicted horizontal tsunami forces using numerical modeling.....	33
Figure 4.19: Correlation between problem termination time and total number of cycles	34
Figure 4.20: Relationship between number of CPUs and consumed CPU time scaled for 300 seconds problem termination time	34
Figure 5.1: Parameters definition used in the recommended equations for estimating tsunami forces.....	39
Figure 5.2: Relationship between total horizontal force and flux momentum (flux momentum-dependent part).....	39
Figure 5.3: Comparison between formula estimation of maximum horizontal tsunami force and numerical prediction of maximum horizontal tsunami force.....	40
Figure 5.4: Correlation between horizontal water velocity with and without obstruction	40
Figure 5.5: Comparison between the formula estimation of maximum vertical force and the numerical prediction of maximum vertical force.....	41
Figure 5.6: Maximum percentage of pressure distribution under each girder along the cross-section at Schooner Creek Bridge.....	41
Figure 5.7: Maximum percentage of pressure distribution under each girder along the cross-section at Drift Creek Bridge	42
Figure 5.8: Maximum percentage of pressure distribution under each girder along the cross-section at Millport Slough Bridge	42
Figure 6.1: Empirical drag coefficients for Spencer Creek Bridge	44
Figure 8.1: Relationships between consumed computational time and number of computer CPUs	50
Figure 8.2: Relationships between computational time, unit cost, and number of computer CPUs.....	51

1.0 ABSTRACT

The Pacific Northwest is vulnerable to seismic events in the Cascadia Subduction Zone (CSZ) that could generate a large tsunami that could devastate coastal infrastructure such as bridges. In this context, this paper describes the development of a guideline for estimating tsunami forces on bridge superstructures along the Oregon Coast. A multi-physics based numerical code is used to perform numerical modeling of tsunami impact on full-scaled bridge superstructures of four selected bridges – Schooner Creek Bridge, Drift Creek Bridge, Millport Slough Bridge, and Siletz River Bridge – located on Highway 101 in the Siletz Bay area on the Oregon Coast. Two different types of bridge superstructure, deck-girder and box sections, are developed in the case of the Schooner Creek Bridge to study the effect of geometry of bridge cross-section. The results show that tsunami forces on box section superstructures are significantly higher than the forces on deck-girder sections; therefore, the box section design might not be appropriate to be used in a tsunami run-up zone. Moreover, numerical simulation of a deck-girder bridge with rigid rails and with open rail spacing, subjected to identical tsunami loads, was performed to examine the effect of rails on tsunami forces. The results suggested that horizontal and vertical tsunami forces on bridges with rails are larger than those on bridges with open rail spacing, up to 20% and 15%, respectively. These numerical results are finally incorporated into the mathematical formulations from the existing literature to develop a simplified method for estimating tsunami forces on bridge superstructures. Appropriate empirical coefficients for bridge superstructures under tsunami loads were evaluated based on an average value of the scattering data from the numerical results. The developed guideline is intended to be used as a preliminary guidance for design only as it did not account for uncertainties; thus, an appropriate load factor must be included in the calculations. A previous analysis of tsunami forces on the Spencer Creek Bridge on the Oregon Coast is revisited to examine the applicability of the guideline developed in the present work. This paper also presents the results of a study on the optimal number of central processing units (CPUs) for running fluid-structure interaction (FSI) numerical models of bridge superstructures using LS-DYNA on high-performance computing (HPC) systems.

2.0 INTRODUCTION

2.1 BACKGROUND

The Oregon coast is vulnerable to large seismic events in the Cascadia Subduction Zone (CSZ), which shares common seismic characteristics with those at Sumatra that generated large tsunamis in the Indian Ocean in December 2004. Studies of tsunami deposits and evidences of coastal subsidence indicate that on average a large seismic event in the CSZ occurs once every 500 years (Goldfinger et al. 2003). The most recent large seismic event in the CSZ occurred in 1700; therefore, there is a relatively high probability that a large seismic event will occur in the near future that could damage the infrastructure along the coastal area in the Pacific Northwest.

The bridges along the Oregon Coast are an important part of the transportation and lifeline system in the area. Any major damages to these bridges would result in traffic disruption and impede post-event emergency response. Since these bridges, mostly built in the 1950-70's, were not designed to resist such large seismic or tsunami loads, they are at risk of being severely damaged during large seismic events. However, unlike seismic loads, currently there is no specific design standard for estimating tsunami forces on bridge superstructures in the US in general and in Oregon in particular. An understanding of tsunami impact on bridge superstructures is of major interest to the practicing engineering community. Consequently, the Oregon Department of Transportation (ODOT) initiated a research program to develop a guideline for estimating tsunami forces on bridge superstructures in the tsunami run-up zone along the Oregon Coast. This guideline is also expected to be applicable in other locations under similar situations.

Nonlinear finite element analysis (NL-FEA) is an essential analysis tool that can be a less expensive alternative to prototype model testing. While laboratory experiments on prototype models provides globally important results, NL-FEA can provide time-history responses that are not readily measurable such as stress, strain, reaction forces, and other variables. Therefore, NL-FEA was used to analyze tsunami impact on bridge superstructures and to determine time-history forces on the bridges under various tsunami load conditions in this study. The numerical models were developed by using a multi-physics finite element based code, LS-DYNA, which was software for accurately analyzing fluid-impact on structures with free surfaces.

This study was divided into two major parts. The first part was to develop numerical models to perform full-scale simulation of tsunami impact on bridge superstructures and calculate reaction forces due to tsunami loads on four selected bridges on the Oregon Coast. The four bridges – Schooner Creek Bridge, Drift Creek Bridge, Millport Slough Bridge, and Siletz River Bridge – are located on Highway 101 in the Siletz bay area as shown in Figure 2.1. The second part was to develop a guideline for estimating tsunami forces on bridge superstructures to be used as preliminary guidance for design of bridges in the tsunami run-up zone. The developed guidance was based on existing literature and the time-history results obtained from the numerical models calculated in the first part.

This research was an extension of a previous case study of tsunami design criteria on the Spencer Creek Bridge, Oregon, conducted by Nimmala et al. (2006). The Spencer Creek project was conducted by developing numerical models of tsunami impact on a bridge deck to determine the time-history forces on the bridge by using LS-DYNA software. The analysis was revisited to examine the applicability of the guideline developed in the present work.



Figure 2.1: Top view map of Siletz bay area and location of the selected bridges

2.2 RUPTURE MODELS AND TSUNAMI SCENARIOS

The input tsunami flow fields, defined as water surface elevation and water velocity time-histories for the simulation models, were obtained from tsunami numerical models developed by Cheung and associates from the University of Hawaii (Cheung et al. 2011). The nonlinear shallow-water model by Yamazaki et al. (2009) was utilized to capture hydraulic processes – wave overtopping, hydraulic jump formation, and bore propagation – describing flow conditions at the interested bridge sites. The development of a rupture model based on 500-year return period CSZ earthquake scenarios from the National Seismic Hazard Maps is illustrated in Figure 2.2. The rupture boundaries extend approximately 1,100 km from Cape Mendocino in northern California to Vancouver Island in British Columbia. The western boundary of the rupture is specified along the trench at the base of the continental slope. Additional conditions were provided by Wang et al. (2003) to define the eastern rupture boundaries at the midpoint of the transition zone (MT) and the base of the transition zone (TZ). Moreover, a global analog (GA) of shallow-dipping subduction zones, from Tichelaar and Ruff (1993), was used to define the eastern rupture boundary at 123.8°W at 30 km depth.

Flow field data of four hours duration for a 500-year Cascadia tsunami event at the Siletz Bay were provided in six different tsunami scenarios. These scenarios were based on four rupture configurations at moment magnitude (Mw) 9.0 and two additional rupture configurations at moment magnitude 8.8 and 9.2. The first configuration assumes the rupture occurs within the

locked zone (LZ, black line in Figure 2.2) only. The eastern rupture occurs at the midpoint of the transition zone (MT, yellow line in Figure 2.2) and at the base of the transition zone (TZ, pink line in Figure 2.2). The fourth rupture configuration is assumed to occur at 30 km depth based on global analog (GA, blue line in Figure 2.2). The Mw 8.8 and 9.2 rupture configurations were also based on the global analog.

A relative weight distribution probability of occurrence for the rupture configurations (0.1, 0.2, 0.2 and 0.5 for LZ, MT, TZ and GA, respectively) and moment magnitudes (0.6, 0.2 and 0.2 for Mw 9.0, 8.8 and 9.2) were assigned based on the logic tree in the Pacific Northwest seismic source model in Cheung et al. (2011). More detailed discussion on tsunami flow field data is provided in appendix F.

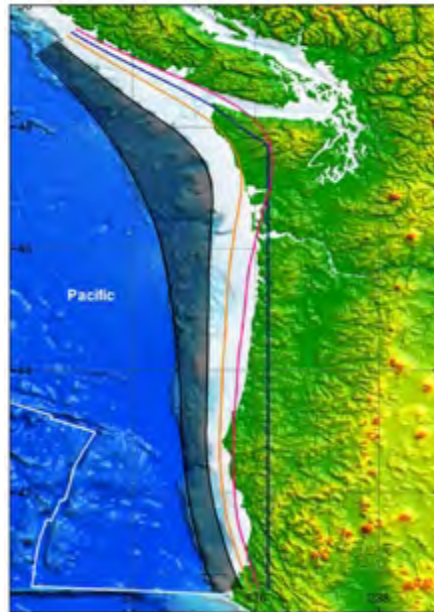


Figure 2.2: Boundaries of Cascadia Subduction zone inferred from the National Seismic Hazard Map (2008) black line: locked Zone (LZ), yellow line: Midpoint of the Transition zone (MT), pink line: Transition Zone (TZ), blue line: Global Analog (GA)

3.0 LITERATURE REVIEW

Currently, there is no specific code of practice to obtain the information of forces on bridge superstructures due to tsunami loads. However, there is an availability of some relevant literature of wave forces on highway bridge decks and offshore platforms, and some literature on tsunami forces for other types of structures such as vertical wall, elevated slab, and columns of different shapes.

3.1 WAVE FORCES EQUATIONS

3.1.1 Wave Forces on Decks of Offshore Platforms

Bea et al. (1999) presented a modification of the American Petroleum Institute (API) guidelines for estimating wind-induced wave forces on a platform deck of offshore structures by separating the total wave force into two components, horizontal force and vertical force. The horizontal force consisted of slamming force ($F_s = 0.5C_s\rho A_h u_x^2$), drag force ($F_d = 0.5C_d \rho A_h u_x^2$), and inertia force ($F_i = C_m\rho Va$). The slamming force and drag force depended on the horizontal velocity of the waves while the inertia force depended on the acceleration. The vertical force consisted of buoyant force ($F_b = \rho Vg$), and lifting force ($F_l = 0.5C_l\rho A_v u_y^2$), which depended on the vertical velocity of the waves. The coefficients and variables are defined in the notation section.

3.1.2 Wave Forces on Bridge Decks

Douglass et al. (2006) presented a method for estimating wave forces on typical U.S. coastal bridges with deck-girder system due to wind waves and storm surge to offer a preliminary guidance for design engineers. The estimated horizontal and vertical forces in that method mainly depend on the elevation of the wave crest (Δh) as shown in equation (3.1) and (3.2), respectively. Other than water elevation, the horizontal force also is depended on the number of girders supporting the bridge deck. This recommended approach was verified with post-storm damages on the U.S. 90 Bridge across Biloxi Bay, Mississippi by Hurricane Katrina.

$$F_H = ([1+C_r(N-1)] C_{h-va} + C_{h-im}) \gamma(\Delta h)A_h \quad (3.1)$$

$$F_V = (C_{v-va} + C_{v-im}) \gamma(\Delta h)A_v \quad (3.2)$$

where C_r is a reduction factor for forces distribution on the internal girders; N is number of girders supporting bridge deck; C_{h-va} and C_{v-va} are empirical coefficients for slow varying horizontal and vertical force respectively; C_{h-im} and C_{v-im} are empirical coefficients for horizontal and vertical impact force respectively. The other parameters are defined in the notation section.

3.2 LITERATURE OF TSUNAMI FORCES

3.2.1 Guidelines for Design of Structures for Vertical Evacuation from Tsunamis

FEMA P646 (2008), guidelines for design of structures for vertical evacuation from tsunamis, summarized the relevant design code and presented equations for estimating tsunami forces on vertical evacuation structures. It also provided some suggestions on how to combine tsunami forces with other loads such as dead load and live load. Load effects that had to be considered for tsunami forces consisted of hydrostatic ($F_h = 0.5\gamma b h_{\max}^2$), hydrodynamic ($F_d = 0.5 C_d \rho b (h u^2)_{\max}$), impulsive ($F_i = 1.5 F_d$), buoyant ($F_b = \rho V g$) and uplift forces ($F_1 = 0.5 C_u \rho A_v u_y^2$). The hydrostatic force depended on water elevation and would be considered to be zero when water fills up on two opposite sides. Unlike the wave forces due to storm surge, the hydrodynamic force due to tsunamis depended on flux momentum ($h u^2$) where h is elevation of water crest and u is horizontal velocity. The impulsive force due to tsunami could be estimated by taking 1.5 times the corresponding hydrodynamic force for conservatism.

3.2.2 Performance-Based Tsunami Engineering

Performance-Based Tsunami Engineering (PBTE, 2010) was developed by a team of ocean, hydraulic and structural engineers to establish guidelines for the design of future coastal infrastructure. In this research, laboratory experiments and simulation models were performed to obtain information of tsunami bore formation, energy dissipation, and coastal inundation. The obtained tsunami flow field was used to study interaction between tsunamis and structural components, such as vertical walls and elevated slabs. The equation for estimating hydrodynamic uplift force presented in this method was a function of horizontal water velocity. A study of sediment transportation due to tsunamis and scour was also included.

3.3 SUMMARY OF LITERATURE REVIEW

The existing literature did not provide adequate information for estimating tsunami forces on bridge superstructures. The existing approaches were mostly applicable for wave force and tsunami force estimation in specific situations. There are significant differences between storm-related waves and tsunami waves that need to be considered in deriving equations to predict storm surge forces and tsunami forces on bridge superstructures. The most important difference is that, in a storm situation, the structure faces a series of short-period waves in a specific time-period but in the tsunami case there are only a few large waves.

The method by Bea et al. (1999) was recommended in API guidelines to estimate wave forces on the lower deck of offshore platforms. The equations presented therein mostly depended on the wave velocity while neglecting the relevance of the wave crest elevation. Moreover, the empirical coefficients were evaluated from laboratory testing on platform deck models which may not be applicable in estimating forces on a highway bridge deck. Douglass et al. (2006) developed a method for the Federal Highway Administration (FHWA) to estimate wave forces on highway bridge decks due to storm surge. Their approach was developed based on laboratory experiments of a scaled bridge deck model in a 3D wave basin. The resulting predictions were

shown to be adequate for estimating the wave force induced by storms as verified by measured field damages from Hurricane Ivan and Katrina. However, the equations presented in that method depended only on wave crest elevation without considering the importance of water velocity, which is an important factor in tsunamis. Finally, the guideline for design of structures for vertical evacuation from tsunamis provided by FEMA P646 (2008) and PBTE (2010) presented details of load effects that had to be considered in estimating the tsunami design forces. These guidelines were developed for vertical structures and elevated slabs only; thus, it might not directly apply to horizontal structures such as bridge superstructures. Based on the equations 3.1 and 3.2 or equations 6.1 to 6.7 all from Douglass et al. (2006), we believe that although the slamming force takes into account the effect of the water velocity, there is no specific part in these equations explicitly related to water velocity to show the direct change in the estimated forces due to change in water velocity.

Even though the existing methods were not appropriate to use directly for estimating tsunami forces on bridge superstructures, they provided background knowledge on wave force characterization and a general idea on how to develop appropriate guidelines for fluid load estimation. These approaches, thus, were modified and incorporated with numerical tsunami force data to develop a guideline for estimating tsunami forces on bridge superstructures along the coast.

4.0 NUMERICAL MODELS OF TSUNAMI IMPACT LOAD ON BRIDGE SUPERSTRUCTURES

The models were developed to perform numerical testing of tsunami impact on realistic bridge superstructures to predict the magnitude of tsunami forces that could occur on specific types of bridge superstructure. This section presents details of the numerical models, bridge descriptions as well as time-history of fluid loads on bridge superstructures under various tsunami flow fields. The effect of different bridge cross-section geometries and the effect of bridge rails on fluid loads are discussed followed by cumulative probabilities of tsunami forces and overturning moments. Furthermore, computational efforts are also summarized and presented in this section.

4.1 MODEL DESCRIPTION

Two-dimensional (2-D) numerical models were developed using a finite-element based code. The provided tsunami flow velocities were assumed to be uniform over depth and resolved in the direction perpendicular to the longitudinal span of the bridge. The cross-section of the bridge superstructure normal to the longitudinal span was modeled by assuming simply supported external girders.

In general, a simulation model consists of two major material parts: a fluid part and a rigid structure part. The fluid part is a composition of water and air materials, each of which is demonstrated by an appropriate material type and an equation of state (explained in Appendix A). For computational efficiency, an approximating rigid body material was used to represent the bridge components, and reaction forces were determined by replacing four rigid elements at supports by elastic material. As mentioned earlier, this study focused on quantifying the maximum value of the horizontal force, vertical force, and overturning moment due to tsunami loads on the selected bridges; thus, it was appropriate to begin the simulation at a time immediately prior to first water impact of the superstructure and terminate the simulation after obtaining the peak values of the time-history of the loads.

The Lagrangian-Eulerian coupling algorithm combined with an Arbitrary Lagrangian-Eulerian (ALE) solver was used in the numerical models as it was the most mature formulation to simulate the problem involving interaction between fluid with high velocity and a rigid structure. The basic concept of the Lagrangian-Eulerian coupling algorithm was to track the relative displacements of the corresponding coupling points defined at the interfaced between the Lagrangian surface (bridge superstructure part) and inside the Eulerian elements (fluid part).

Figure 4.1 shows an example of the numerical model of the Millport Slough Bridge developed in this research. The model consisted of three material parts: water, air, and bridge parts. Material properties for each part – such as material mass density, pressure cut-off, fluid viscosity, modulus of elasticity, and Poisson's ratio – were specified appropriately as they were used in the ALE differential equation and in calculating of interface stiffness. Even though the numerical

model was two dimensional, it could be thought of as a three dimensional rectangular cross-section with unit thickness in the z-direction. The cross-section was composed of water and air material parts with a bridge part inside. Setting up the boundary conditions for the numerical models is described in Appendix A-1.

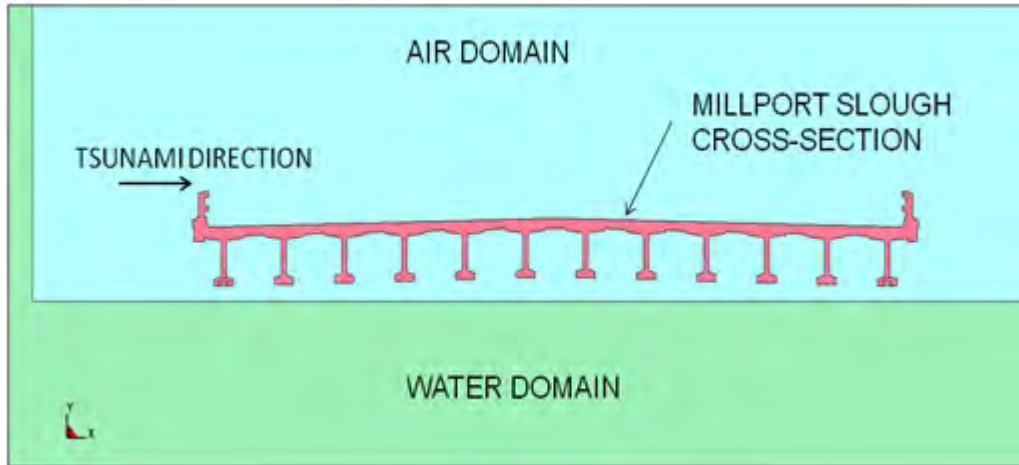


Figure 4.1: An example of numerical model of Millport Slough Bridge

4.2 BRIDGE DESCRIPTIONS AND TSUNAMI FLOW FIELDS

Numerical models of four selected bridges in the Siletz bay were developed for this tsunami load estimation study. The first was the Schooner Creek Bridge located close to the open channel of the bay facing directly toward the incoming tsunamis as shown in Figure 2.1. Two types of bridge geometry – deck-girder and box section – under identical tsunami flow fields were examined to determine the effects of bridge cross-sectional geometry. The cross-section of the Schooner Creek Bridge was not symmetrical as the west edge (tsunami impact face) was lower than the east edge due to a 4% slope for the deck-girder section and a 3% slope for the box section, as shown in Figure E.1 and Figure E.2, respectively. The reference bridge elevation measured at the support of the lowest (west-most) bridge girder was approximately 18 feet above mean sea level (MSL). This is the only skewed bridge among the four studied.

The second bridge was the Drift Creek Bridge located southeast of the Schooner Creek in a more open area. The bridge geometry was similar to that of the Schooner Creek Bridge (deck-girder section) with a smaller cross-sectional width and fewer girders supporting the bridge deck. The bridge was designed for a 2% slope with a reference elevation of approximately 14 feet above MSL, as shown in Figure E.3.

The third bridge was the Millport Slough Bridge located at the south end of the Siletz Bay on Highway 101. The bridge, which had a 2% slope crown with a reference elevation of 15 feet above MSL, as shown in Figure E.4 and Figure E.5, was under replacement construction (at the time of the writing, December 2010).

Finally, the fourth bridge was the Siletz River Bridge. This bridge, which was under design as a box section, with a reference elevation of approximately 33 feet above MSL, was high compared to that of the other three bridges.

As mentioned earlier, six different tsunami flow fields were provided for each bridge site (GA Mw 8.8, GA Mw 9.0, GA Mw 9.2, LZ Mw 9.0, MT Mw 9.0 and TZ Mw 9.0). However, the maximum water surface elevations generated in some scenarios were lower than the reference bridge elevation, so these scenarios were neglected because the tsunamis would not induce forces on the superstructures. In particular, five tsunami scenarios – GA Mw 9.0, GA Mw 9.2, LZ Mw 9.0, MT Mw 9.0 and TZ Mw 9.0 – were applicable to the Schooner Creek Bridge, and three scenarios – GA Mw 9.2, LZ Mw 9.0 and MT Mw 9.0 – were also applicable to the Drift Creek Bridge and the Millport Slough Bridge. On the other hand, all six tsunami scenarios could be neglected for the Siletz River Bridge as it was designed for such a high elevation that prevented the tsunami flow from reaching the superstructure. (While a finite-element model of the bridge was developed prior to receiving the tsunami flow field data, the Siletz River Bridge was removed from further tsunami impact load analysis.) The input tsunami flow fields of the applicable scenarios at each bridge site are shown in Appendix A-2. A set of Screen captures of different bridges under different tsunami scenarios are provided in the Appendix A-3.

4.3 TSUNAMI FORCE TIME-HISTORIES

Figure 4.2 to Figure 4.13 show the time-histories of the numerical prediction of reaction forces – horizontal force and vertical force – and overturning moments due to tsunami loads on the three affected bridges calculated from the numerical models. The maximum values of horizontal and vertical forces and also overturning moments due to different tsunami scenarios are provided in tables 4.1 to 4.3. Since it was assumed that the exterior girders are simply supported, the total horizontal and vertical forces on the bridges can be computed by applying the equilibrium of forces in the horizontal and vertical directions. In other words the reaction forces in these two supports show the total horizontal and vertical forces on bridge. The horizontal tsunami forces on the box section, black line in Figure 4.2, showed a pattern of a short duration high intensity force at the time immediately after the water impacted the bridge followed by fluctuating drag forces similar to those reported by Yeh et al. (2005). The impact forces on the box section were approximately 1 to 2.5 times the corresponding drag forces, whereas the maximum impact horizontal forces on the deck-girder section were sometimes smaller than the corresponding maximum drag force.

The simulated horizontal reaction forces on Millport Slough Bridge and Drift Creek Bridge are shown in Figure 4.8 and Figure 4.11, respectively. A comparison of the vertical tsunami force time-histories on both the box section and deck-girder at the Schooner Creek is shown in Figure 4.3. As will be shown in section 4.4, the vertical tsunami forces on both sections show a similar pattern as the forces rapidly increased at the time the water impacted the structure followed by considerably steadier forces until the water subsided.

To summarize, tsunami forces on the superstructure of the selected bridges were quite different given the same tsunami scenario. According to the results discussed above, the Siletz River Bridge could survive a 500-years Cascadia tsunami event because the designed reference

elevation of the bridge superstructure was sufficiently high to avoid tsunami loads while the other three bridges were inundated in some scenarios. Figure 4.14 shows the water surface elevation at the Siletz River Bridge compared to the designed reference elevation of the bridge. The Schooner Creek Bridge and the Drift Creek Bridge were subjected to large tsunami forces, compared to the forces on the Millport Slough Bridge, because they were located in an open area close to the inlet channel of the bay directly facing the incoming tsunamis while the Millport Slough Bridge was located far from the inlet channel.

According to the numerical results, the magnitude of the tsunami forces on a bridge superstructure generated from different rupture configurations and moment magnitudes can be significantly different. Mostly, the forces are extremely high and it may not be reasonable to design a bridge to resist such large forces that occur rarely. The joint probability distribution of the rupture configurations and their corresponding earthquake moment magnitude which provides a basis for probabilistic design for a 500-year Cascadia tsunami event is shown in Table 4.4 (Cheung et al. 2011). Observe that the GA rupture with Mw 9.0 has the highest probability of occurrence in the Pacific Northwest seismic event, and the numerical prediction of loads represent reasonable tsunami design forces.

Table 4.1: Maximum forces and moments due to tsunami loads on superstructure of Schooner Creek Bridge

Tsunami Scenario	Horizontal Force (kip/ft)		Vertical Force (kip/ft)		Overturning Moment (k-ft/ft)	
	Deck-Girder	Box Girder	Deck-Girder	Box Girder	Deck-Girder	Box Girder
GA 9.0	11.6	150	5.0	600	1570.0	40600
GA 9.2	80	150	370	720	18900	49600
LZ 9.0	71	200	360	840	18200	51700
MT 9.0	52	230	230	685	14200	47600
TZ 9.0	49.0	190	123.0	630	8200.0	43600

Table 4.2: Maximum forces and moments due to tsunamis on Drift Creek Bridge (with rigid rails)

Tsunami Scenario	Horizontal Force (kip/ft)	Vertical Force (kip/ft)	Overturning Moment (k-ft/ft)
GA 9.2	96.0	147	6090
LZ 9.0	77.0	156	6420
MT 9.0	29.0	120	5110

Table 4.3: Maximum forces and moments due to tsunamis on superstructure of Millport Slough Bridge (including rails)

Tsunami Scenario	Horizontal Force (kip/ft)	Vertical Force (kip/ft)	Overturning Moment (k-ft/ft)
GA 9.2	8.0	47.0	1760
LZ 9.0	8.0	34.0	1265
MT 9.0	5.0×10^{-3}	0.04	1.2

4.4 EFFECT OF CROSS-SECTIONAL BRIDGE GEOMETRY

The maximum horizontal and vertical reaction forces, and the maximum overturning moments on two different bridge types – deck-girder and box section – of the Schooner Creek Bridge are summarized in Table 4.1. It can be observed that the maximum forces and moments on the box section superstructure were significantly higher than those of the deck-girder section. One of the major load effects that must be considered for tsunami forces calculation is the hydrostatic pressure which is a function of distance between water surface elevation and the reference elevation of the bridge cross-section (Δh). Unlike the box-section, chambers between girders supporting the deck allow water to flow in, which help in reducing encountered hydrostatic pressures under the bridge superstructure. Moreover, a study of the effects of air compression to wave forces on coastal bridge decks (Cuomo et al. 2009) suggested that the air compression trapped in a chamber behaved as a cushion opposing the violent flow. Cuomo et al. (2009) suggested that wave energy was lost in compression of the air trapped which reduced wave impact pressures. Therefore, it is reasonable that tsunami forces on a box section bridge are higher than those on a deck-girder section under identical incoming tsunami flow fields. The time-histories of the horizontal and vertical tsunami forces on the box section and the deck-girder section, plotted in Figure 4.2 and Figure 4.3 respectively, appear to confirm the above observations. Note the tentative conclusions drawn here are based only on numerical simulations, experimental verifications including both girders and box sections are needed to confirm their validity.

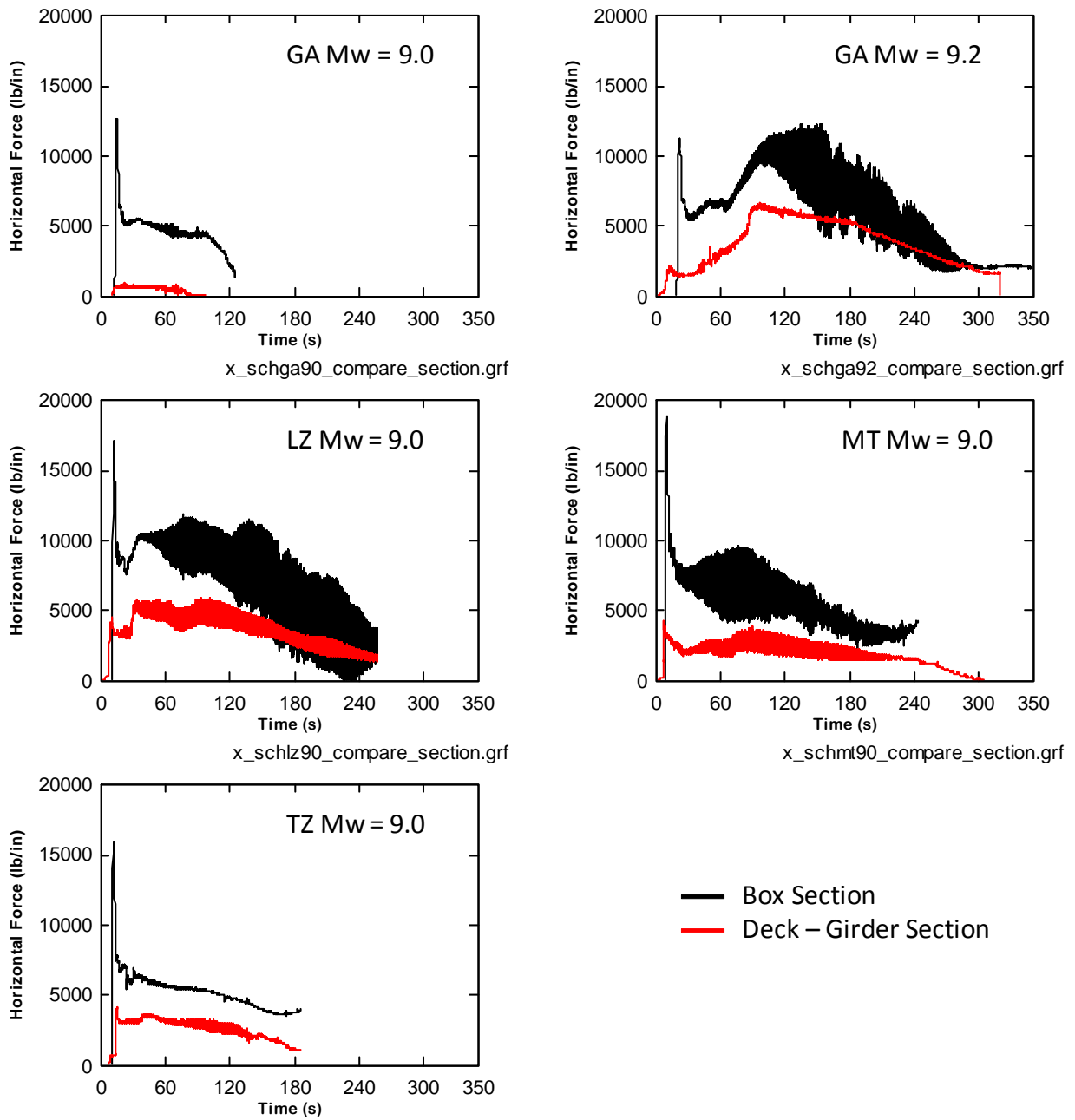


Figure 4.2: Comparisons of numerical prediction of horizontal tsunami force (lb/in) time-history for different bridge geometry

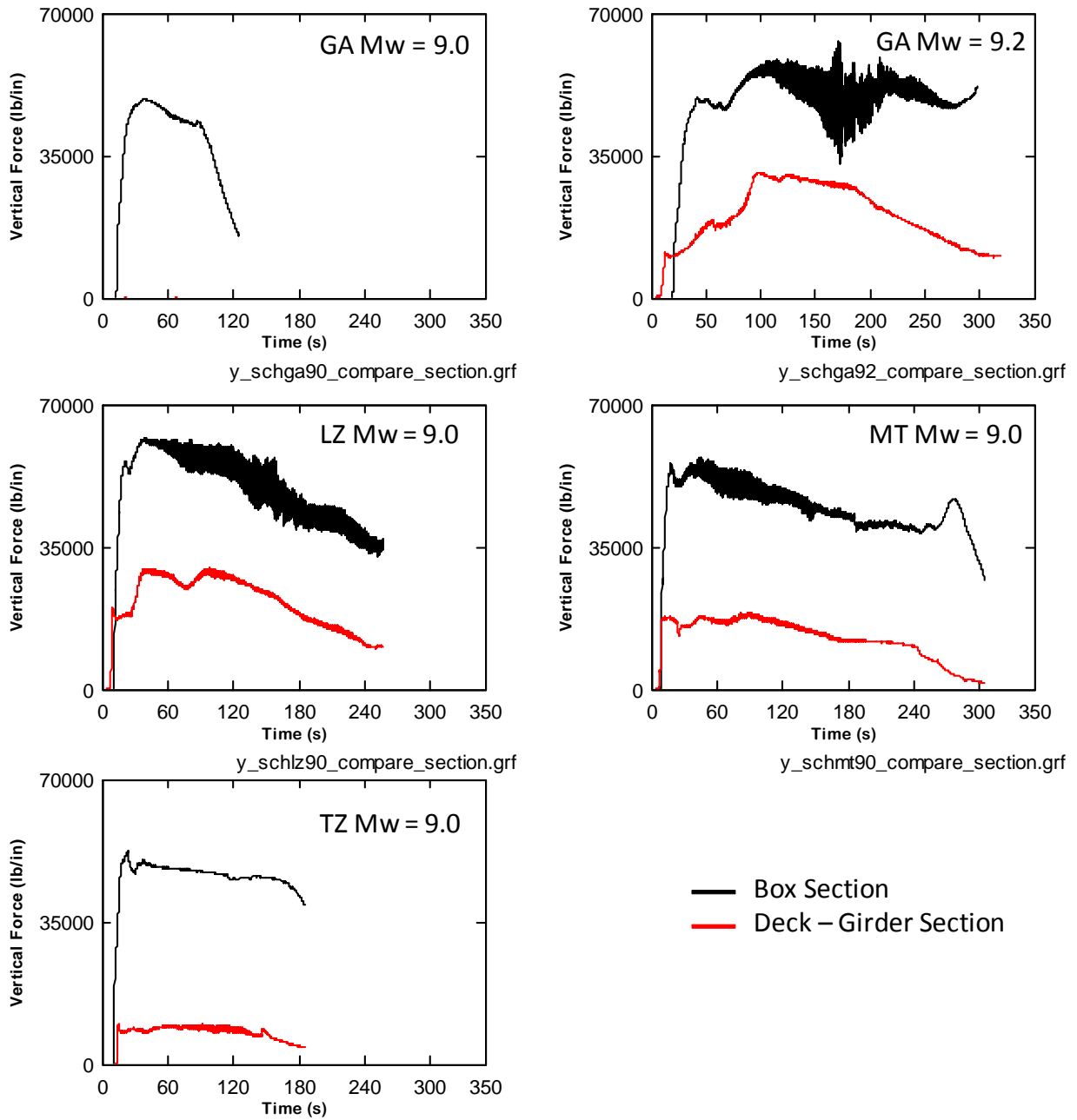


Figure 4.3: Comparisons of numerical prediction of vertical tsunami force (lb/in) time-history for different bridge geometry

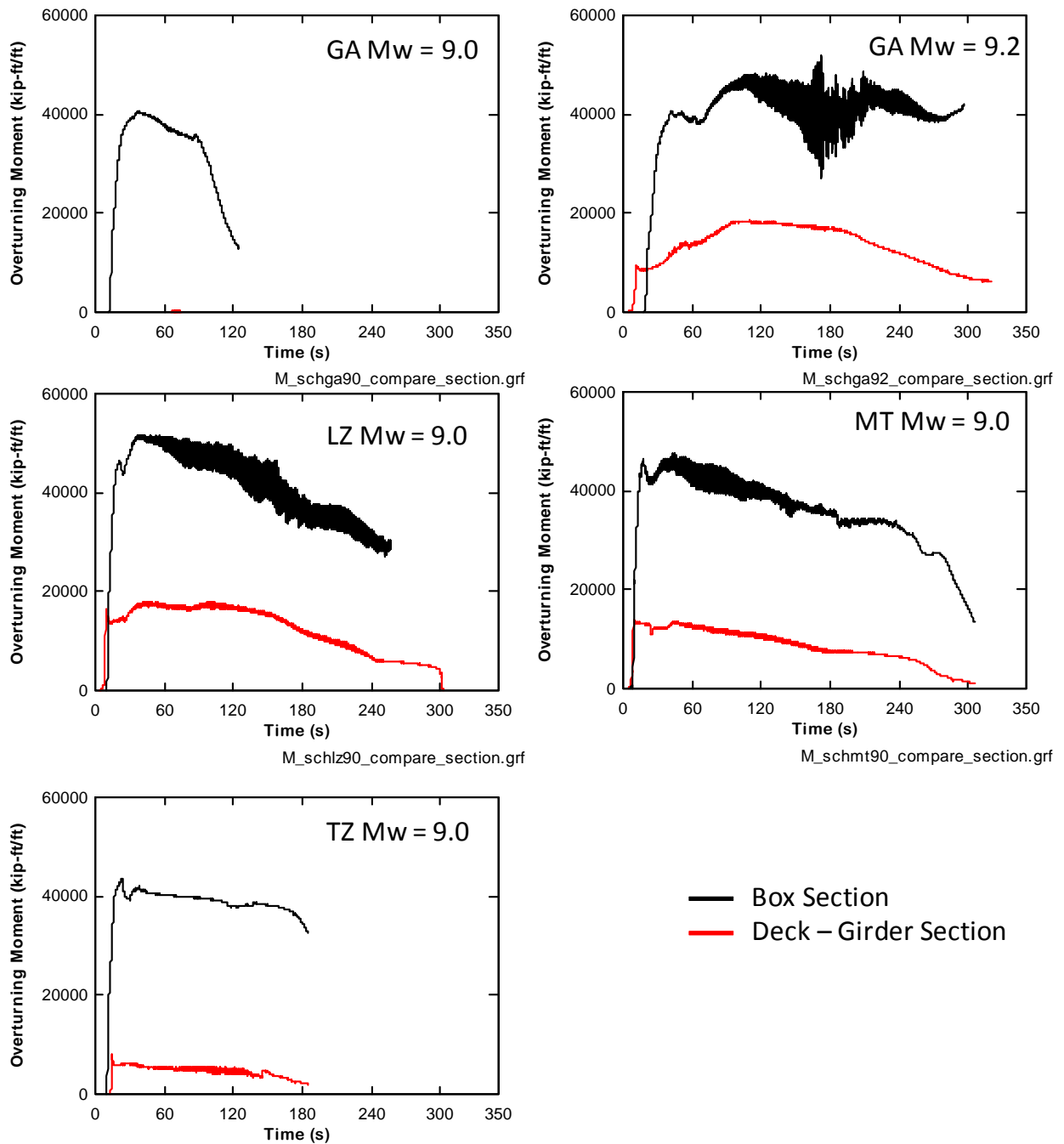


Figure 4.4: Comparisons of numerical prediction of overturning moment (kip-ft/ft) time-history for different bridge geometry

4.5 EFFECT OF RAILS

To examine the effect of the presence of bridge rails, numerical models were developed of deck-girder sections with rigid rails and with open rail spacing with the same tsunami loading. Figure 4.5 to Figure 4.10 show comparisons of the fluid forces and moments on the bridge superstructures with rigid rails and with open rail spacing. It can be observed that the presence of rigid rails did not significantly affect the magnitude of the impact force but induced a slightly larger drag force for fully inundated bridge superstructures. The results appeared reasonable since having the rails would increase the projected vertical area encountering horizontal flows which results in an increase in the maximum horizontal force. The results show that the horizontal tsunami force on a bridge with rigid rails was higher than the force on a bridge with open rail spacing by up to approximately 20%. Furthermore, in practice, the rails should not significantly affect the vertical uplift force on an inundated bridge because the vertical force depends mostly on the horizontal projected area under the bridge superstructure, water velocity, and inundation depth and the water passes through between the rails. However, the model of bridge with rigid rails in this study was selected at the rail post and assumed that water could not flow through the spaces between the rails; thus, the vertical tsunami force on the bridge with rails could be higher than that on the bridge with open rail spacing because rails would prevent water from overtopping the superstructure, thereby increasing the buoyancy force. According to the numerical results, vertical tsunami forces on bridges with rigid rails could be higher than the force on bridges with open rail spacing by up to 15%.

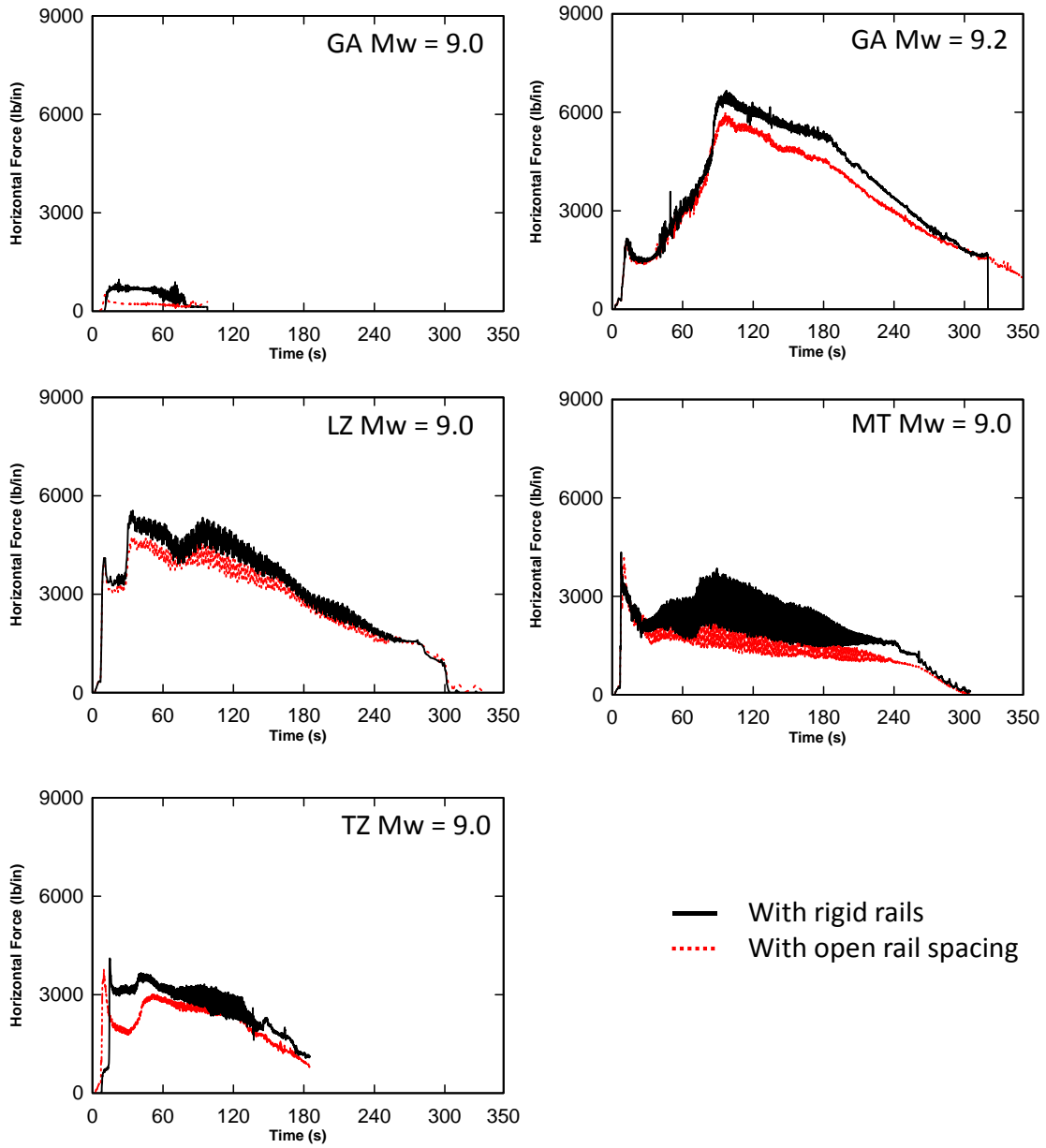


Figure 4.5: Time-Histories of numerical prediction of horizontal tsunami force (lb/in) for Schooner Creek Bridge (Deck-Girder)

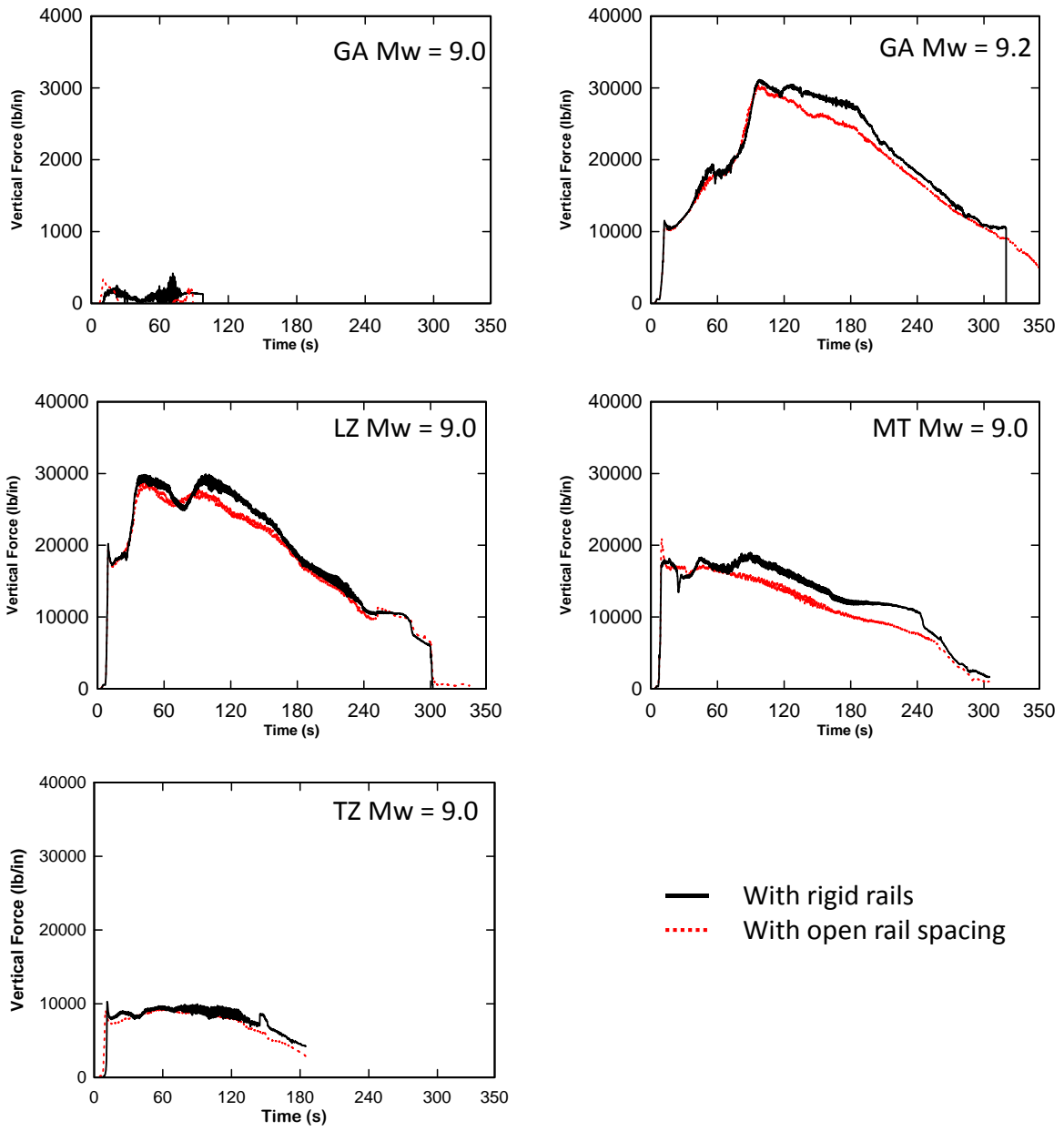


Figure 4.6: Time-Histories of numerical prediction of vertical tsunami force (lb/in) for Schooner Creek Bridge (Deck-Girder)

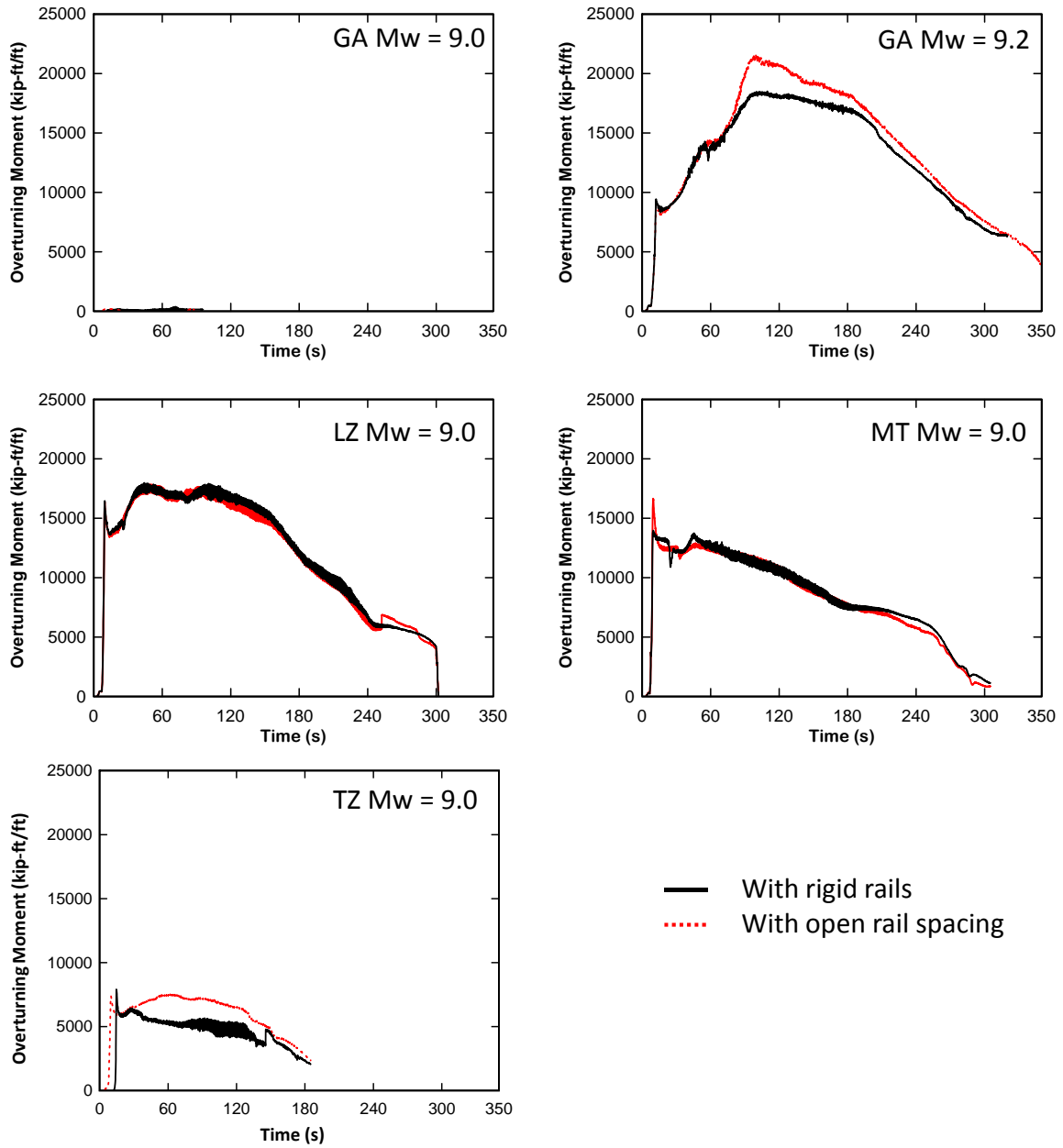


Figure 4.7: Time-Histories of numerical prediction of overturning moment (kip-ft/ft) for Schooner Creek Bridge (Deck-Girder)

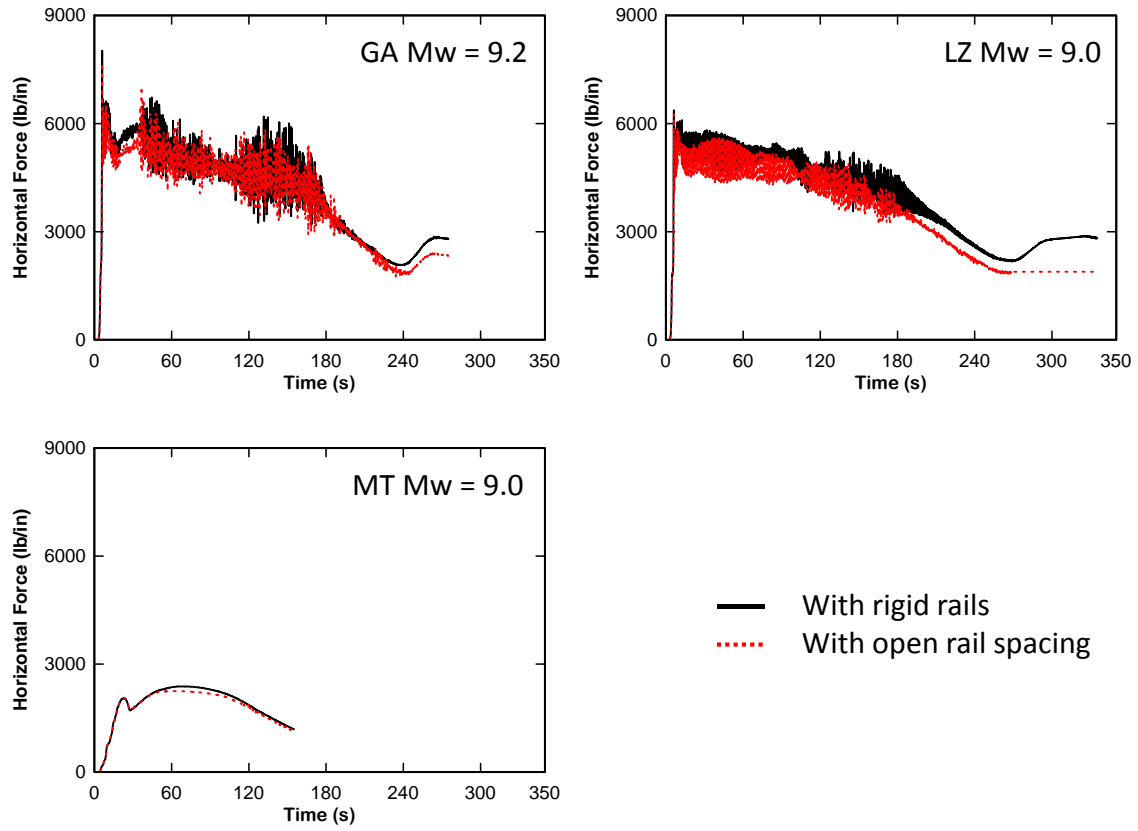


Figure 4.8: Time-Histories of numerical prediction of horizontal tsunami force (lb/in) for Drift Creek Bridge

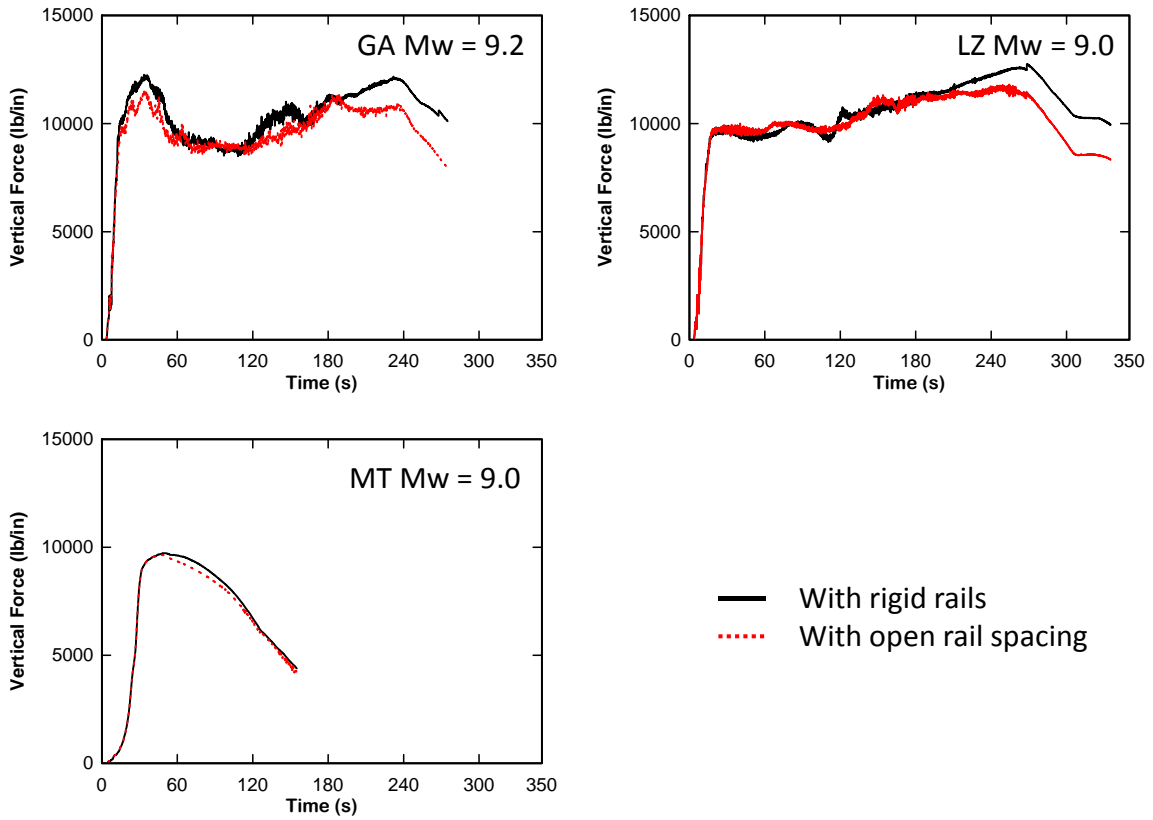


Figure 4.9: Time-Histories of numerical prediction of vertical tsunami force (lb/in) for Drift Creek Bridge

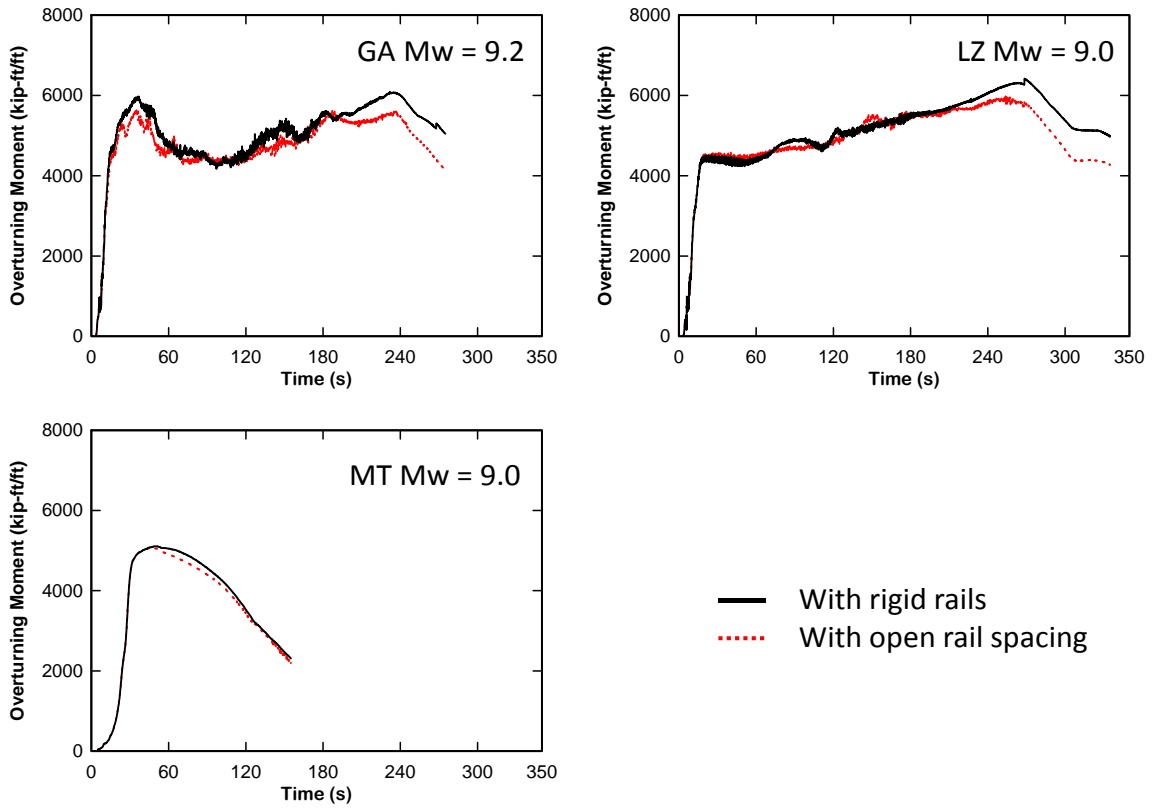
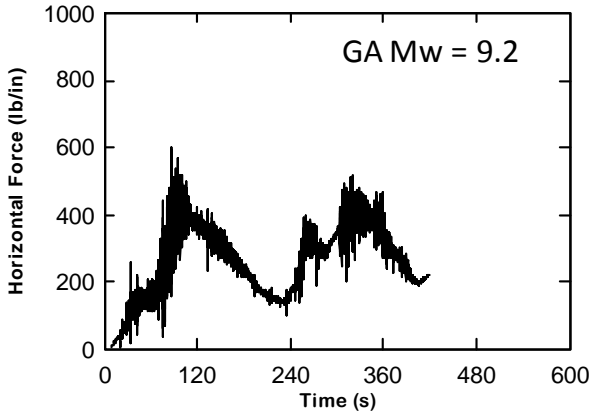
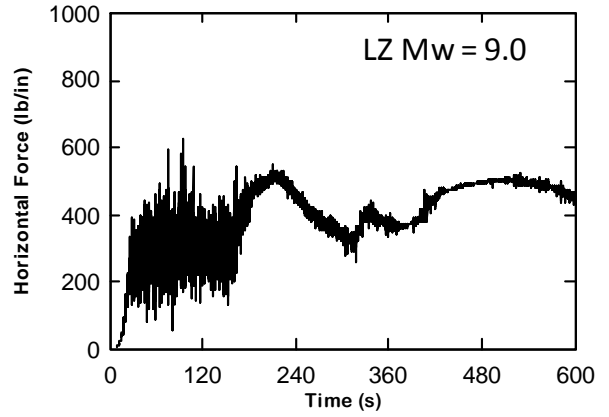


Figure 4.10: Time-Histories of numerical prediction of overturning moment (kip-ft/ft) for Drift Creek Bridge



x_millportga92.grf



x_millportlz90.grf

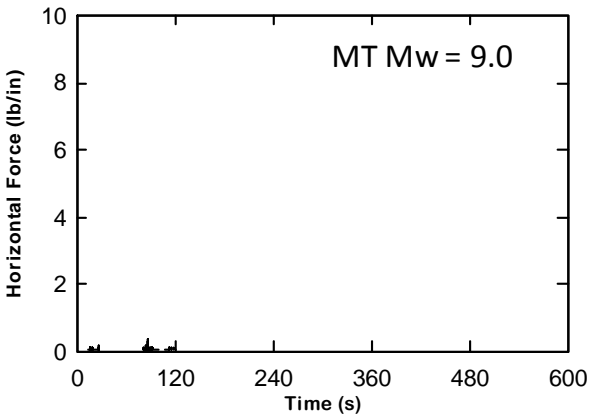
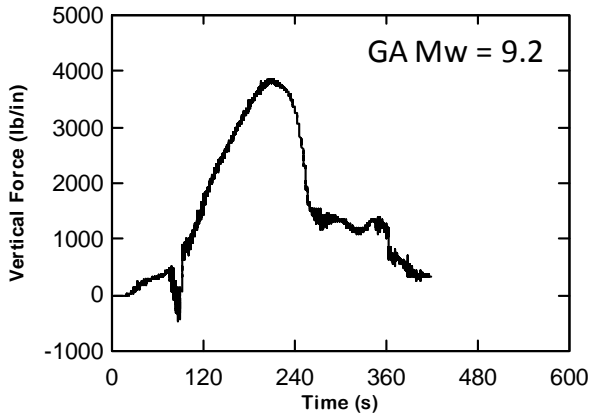
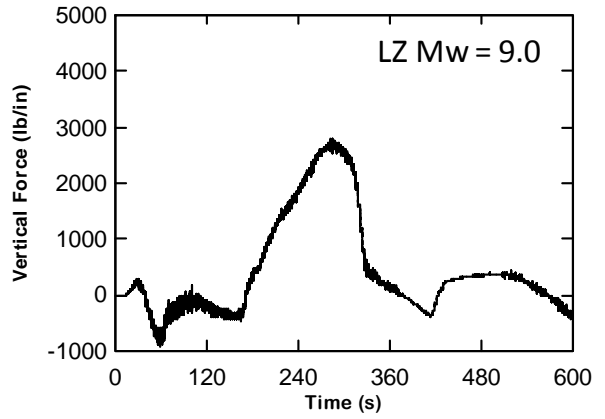


Figure 4.11: Time-Histories of numerical prediction of horizontal tsunami force (lb/in) for Millport Slough Bridge



y_millportga92.grf



y_millportlz90.grf

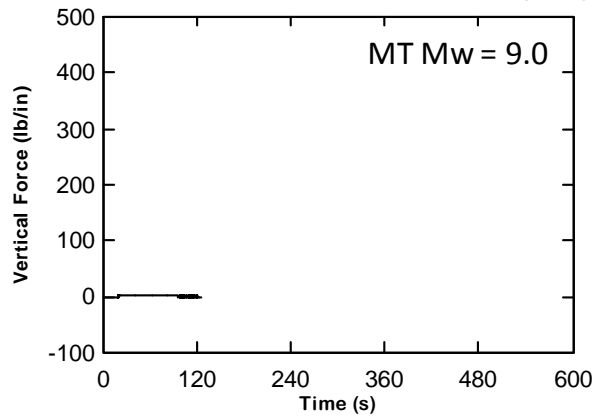


Figure 4.12: Time-Histories of numerical prediction of vertical tsunami force (lb/in) for Millport Slough Bridge

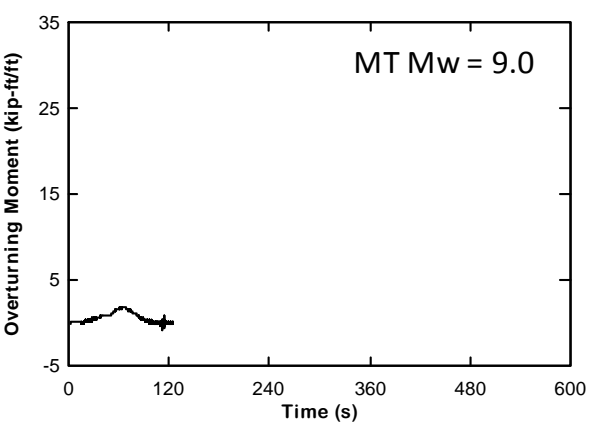
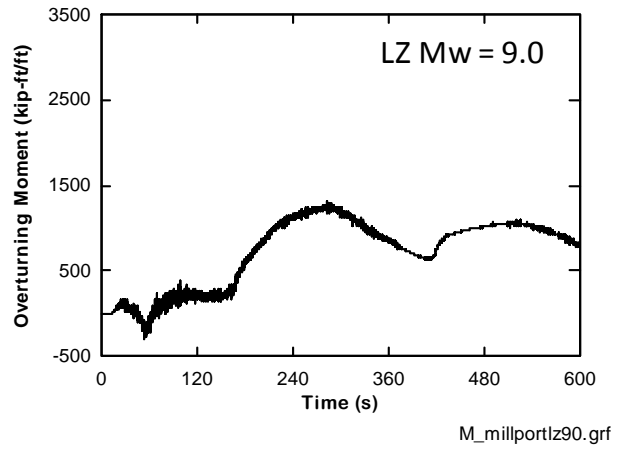
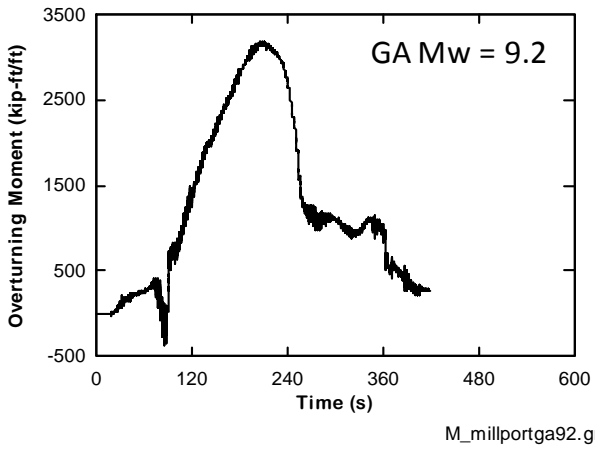


Figure 4.13: Time-Histories of numerical prediction of overturning moment (kip-ft/ft) for Millport Slough Bridge

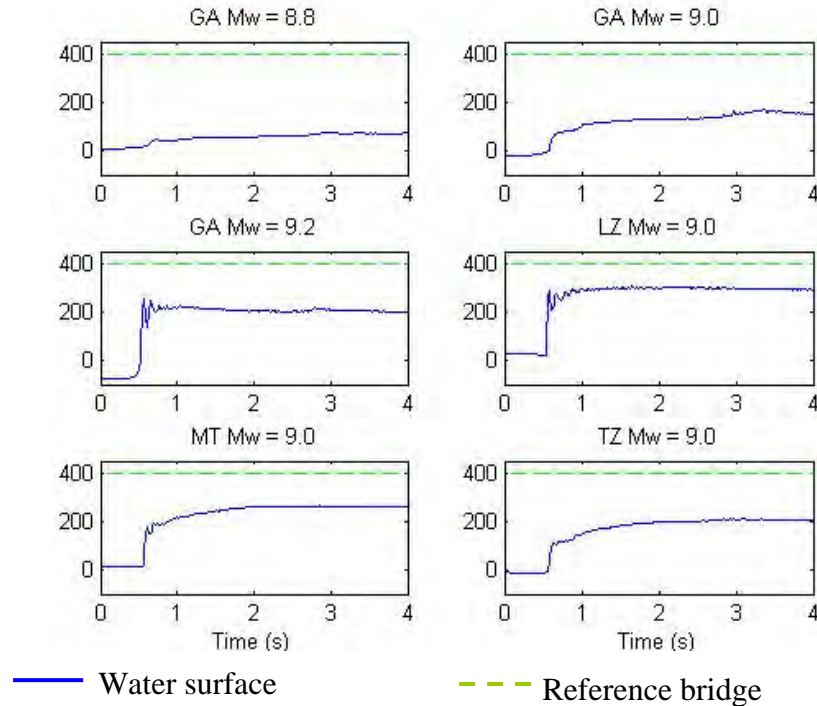


Figure 4.14: Water elevation time-histories at Siletz River Bridge

4.6 CUMULATIVE PROBABILITY OF MAXIMUM TSUNAMI FORCES

Joint probability of 12 scenarios based on four rupture configurations and three earthquake moment magnitudes from the 2008 National Seismic Hazard Maps were provided by Cheung et al. 2011 (see Table 4.4). The provided probability on each scenario was assigned to the corresponding maximum tsunami forces and moments generated on the superstructures. Figure 4.15, Figure 4.16, and Figure 4.17 illustrate cumulative probabilities of the numerical prediction of maximum horizontal force, vertical force and overturning moment due to tsunamis, respectively. Note that the six scenarios incorporating the combination of LZ, MT and TZ rupture at Mw 8.8 and Mw 9.2 were not used for this study as they had considerably low probability of occurrence and ODOT and Cheung decided not to generate them. For this study, tsunami forces generated in the three ruptures with Mw 8.8 were assumed equal to the minimum predicted forces on each bridge while the forces generated in the ruptures with Mw 9.2 were assumed equal to the maximum predicted forces on each bridge.

According to these cumulative probabilities, the Schooner Creek Bridge had the highest probability of being subjected to relatively large tsunami forces while the Millport Slough Bridge had the lowest probability. These results corresponded to the location of the bridges since the Schooner Creek Bridge was located closest to the inlet channel in the bay while the Millport Slough was located furthest. However, there were no forces on the Siletz River Bridge because the designed reference elevation of the superstructure was significantly higher compared to the other three bridges, which helped prevent the tsunami flows from reaching the superstructure. Therefore, as expected, location and reference elevation of the bridge superstructure are important factors for tsunami load estimation.

Table 4.4: Joint Probability of Rupture Scenarios (Cheung et al. 2011)

Rupture	Moment Magnitude, M_w			<u>Total</u>
	8.8	9	9.2	
LZ	0.02	0.06	0.02	0.1
MT	0.04	0.12	0.04	0.2
TZ	0.04	0.12	0.04	0.2
GA	0.1	0.3	0.1	0.5
<u>Total</u>	0.2	0.6	0.2	1

Figure 4.18 shows the correlation between maximum flux momentums and maximum predicted horizontal tsunami forces using numerical modeling. The values of horizontal axis which shows the maximum flux momentums are based on the tsunami flow field data and the vertical axis shows the numerical prediction of the maximum horizontal tsunami forces using FE modeling. It was reasonable to assume that the maximum horizontal force was approximately linearly proportional to the maximum flux momentum as suggested in FEMA (2008) and PBTE (2010).

4.7 COMPUTATIONAL EFFORTS

Two computational platforms were used to analyze the developed numerical models. The first was an eight-processor workstation, Intel Xeon with 34 GB memory, while the second was a parallel cluster system consisting of 1100 two-processor socket dual-core with 16 GB memory each. The processors on the parallel cluster system operated at 3.0 GHz frequency. A record of the computational efforts – number of CPU nodes and CPU time – is summarized in Table 4.5.

As mentioned earlier, the time-marching algorithm in the numerical models was based on explicit integration. An average time step size (Δt) used in calculation of the models was approximately 5×10^{-6} which resulted in long computational time up to approximately 190 hours depending on the number of CPUs used for calculation and the specified problem termination time. The total number of cycles of the models ranged from approximately 20×10^6 to 120×10^6 depending on the corresponding termination time (but independent of the number of CPUs used). A linear relationship between the total number of cycles and the termination time is shown in Figure 4.19. When the CPU run time was scaled to a 300-seconds termination time, the correlation between the CPU run time and the number of CPUs (shown in Figure 4.20) was observed to decrease parabolically with increasing number of CPUs.

Table 4.5: Computational efforts for performing the simulation models

Tsunami Scenario	Computer System	Number of CPUs (ncpu)	Problem Termination Time (s)	CPU Run Duration (hrs)	Number of Cycles
Schooner Creek Bridge: Deck-Girders (with rigid rails)					
GA M _w 9.0	8-processor workstation	6	98	117	2.0E+07
GA M _w 9.2	parallel cluster	32	365	86	7.3E+07
LZ M _w 9.0	parallel cluster	64	335	83	6.8E+07
MT M _w 9.0	parallel cluster	32	305	68	6.2E+07
TZ M _w 9.0	8-processor workstation	6	185	111	2.4E+07
Schooner Creek Bridge: Box Section (with rigid rails)					
GA M _w 9.0	8-processor workstation	6	125	53	2.5E+07
GA M _w 9.2	parallel cluster	64	365	63	7.3E+07
LZ M _w 9.0	8-processor workstation	6	257	N/A	N/A
MT M _w 9.0	8-processor workstation	6	305	121	6.2E+07
TZ M _w 9.0	8-processor workstation	6	185	76	3.7E+07
Drift Creek Bridge (with rigid rails)					
GA M _w 9.2	parallel cluster	16	275	99	5.6E+07
LZ M _w 9.0	parallel cluster	16	335	120	6.8E+07
MT M _w 9.0	Parallel cluster	16	155	51	3.1E+07
Millport Slough Bridge (with rigid rails)					
GA M _w 9.2	parallel cluster	32	363	N/A	N/A
LZ M _w 9.0	parallel cluster	32	612	190	1.2E+08
MT M _w 9.0	8-processor workstation	6	125	N/A	N/A

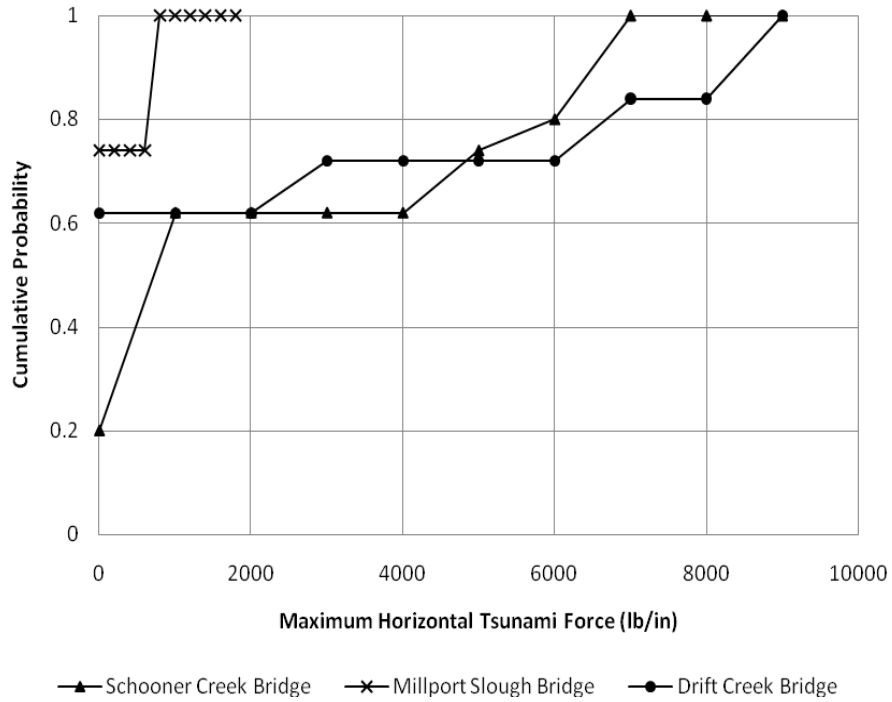


Figure 4.15: Cumulative probability of Maximum Horizontal Tsunami Force

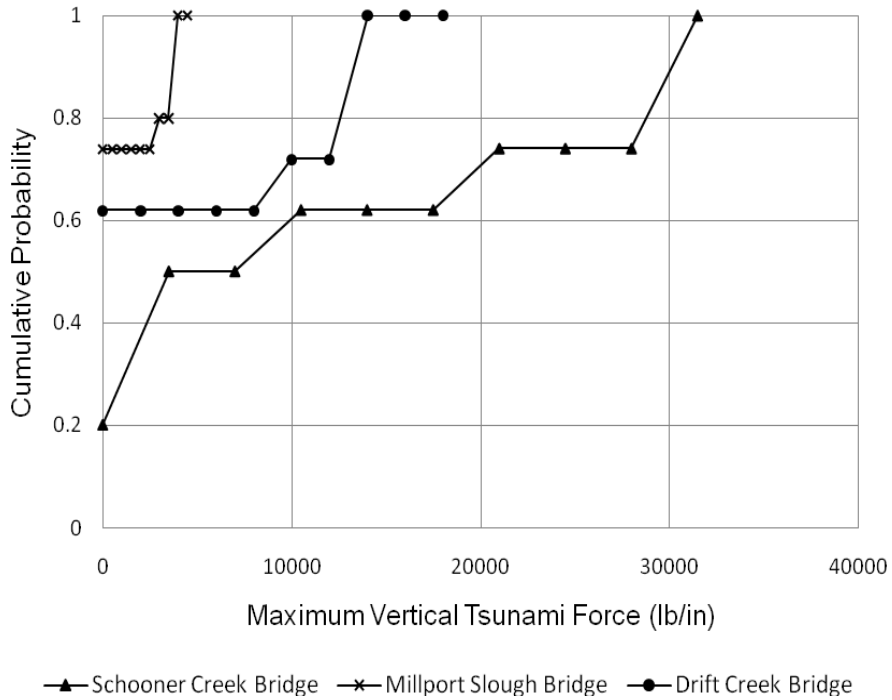


Figure 4.16: Cumulative probability of Maximum Vertical Tsunami Force

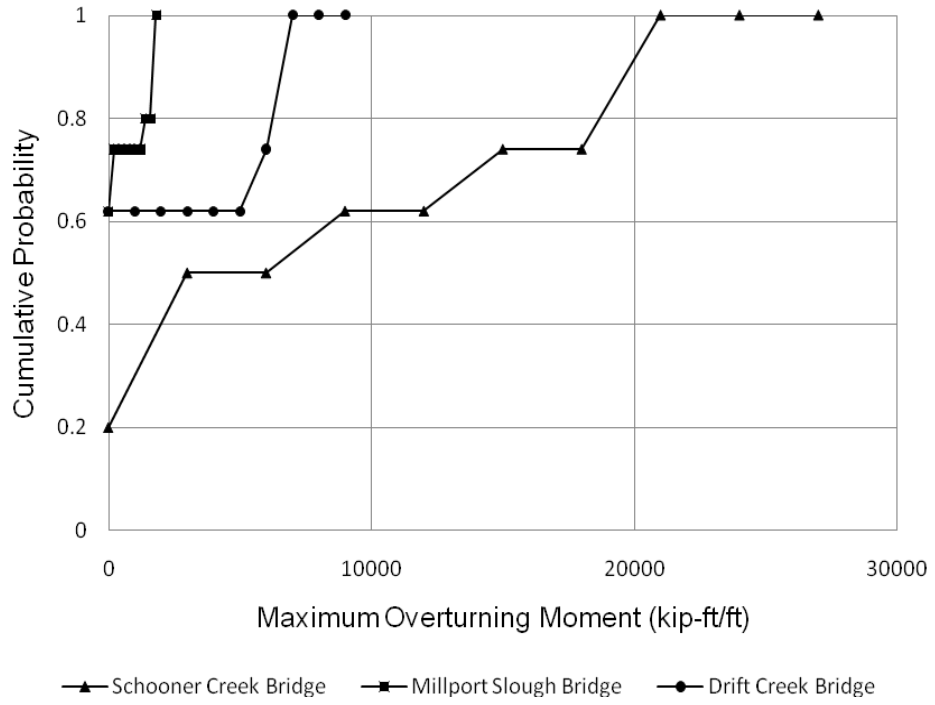


Figure 4.17: Cumulative probability of Maximum Overturning Moment due to Tsunamis

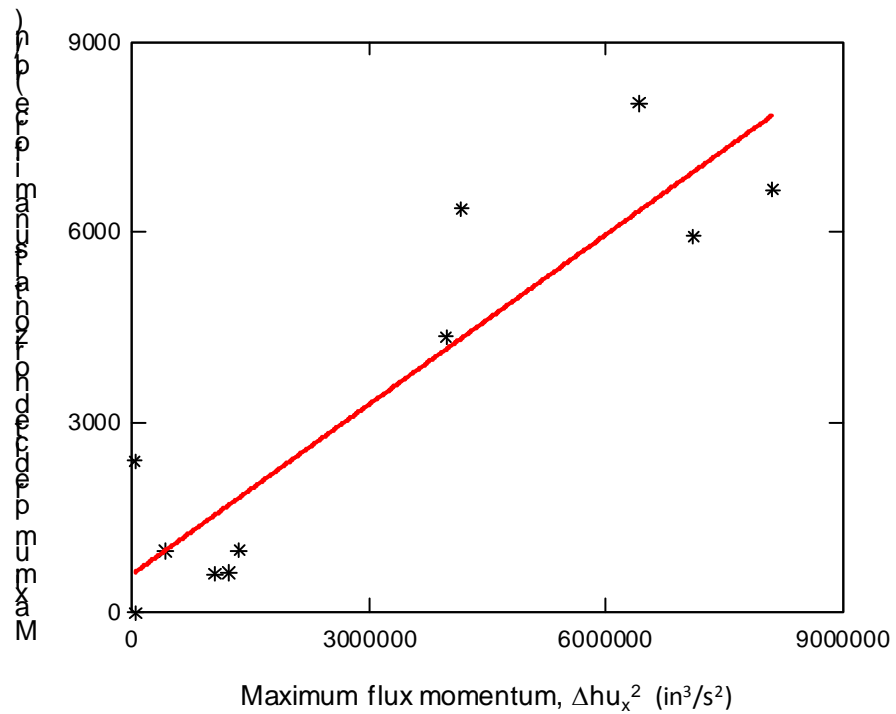


Figure 4.18: Correlation between maximum flux momentums and maximum predicted horizontal tsunami forces using numerical modeling

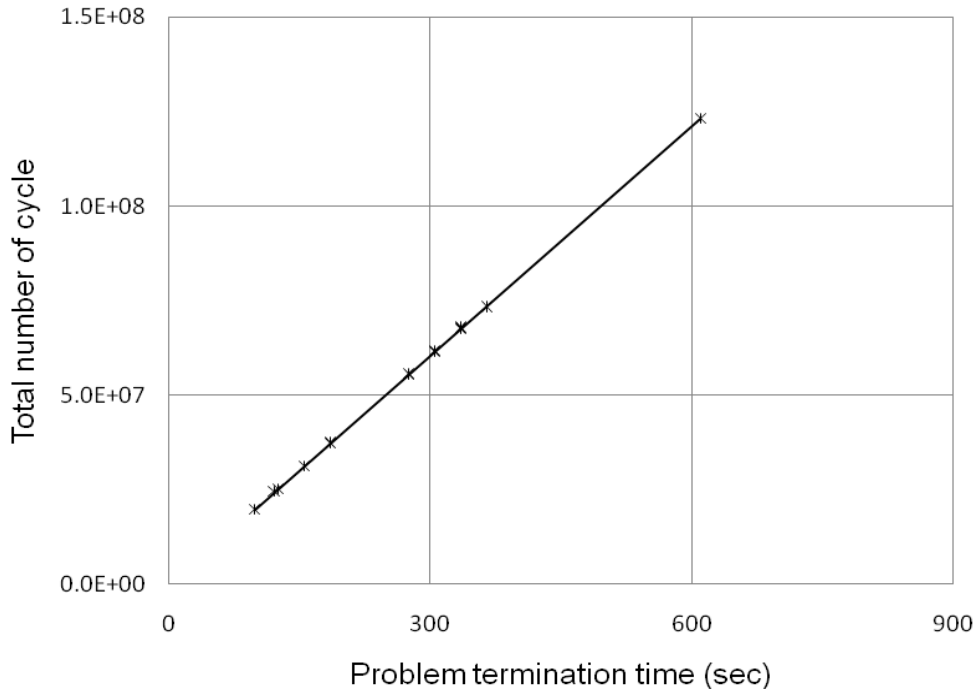


Figure 4.19: Correlation between problem termination time and total number of cycles

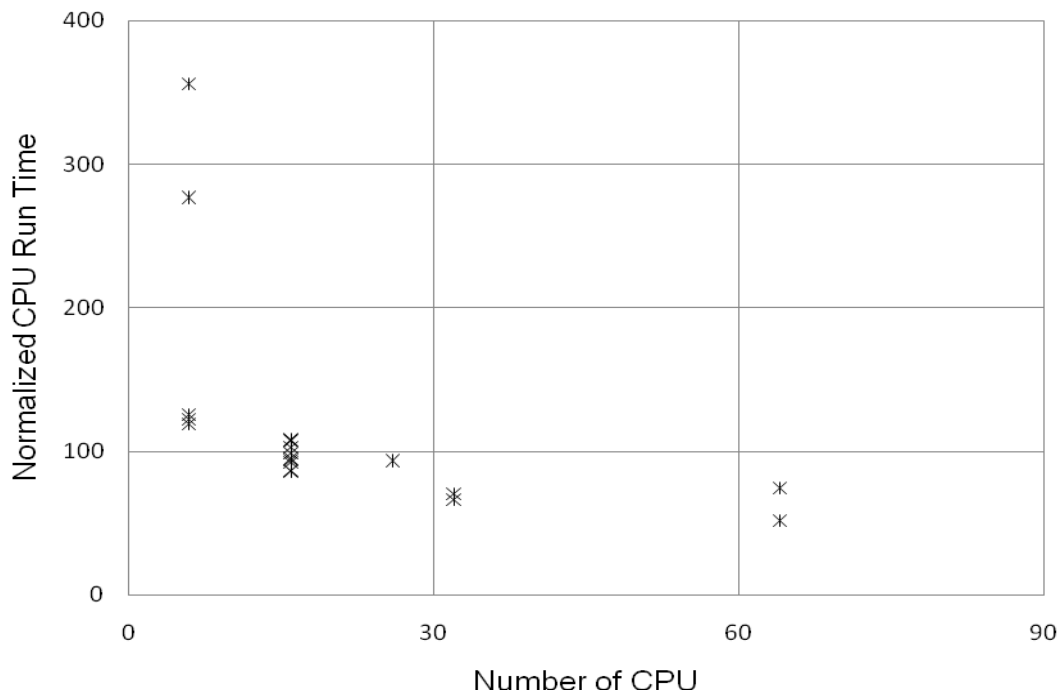


Figure 4.20: Relationship between number of CPUs and consumed CPU time scaled for 300 seconds problem termination time

5.0 ESTIMATION OF TSUNAMI FORCES ON BRIDGE SUPERSTRUCTURES

This section presents a development of a guideline for estimating tsunami forces on superstructures for preliminary design of bridges in a tsunami run-up zone along the Oregon Coast. This approach was developed by incorporating the relevant existing literature and the tsunami forces obtained from the numerical models developed in Section 4.0.

The total tsunami force on a bridge superstructure can be considered separately as horizontal and vertical components. The horizontal component acts perpendicularly to the longitudinal span of the bridge superstructure while the vertical component acts in upward and downward directions normal to the wave direction. The estimated total tsunami forces are assumed to apply to the bridge superstructure through the centroid of the cross-sectional area as shown in Figure 5.1. It is worth mentioning that all the loads computed using recommended equations are per unit length of the bridge which is consistent with 2-D analysis approach used for this study.

5.1 HORIZONTAL FORCES

The total horizontal forces on the bridge superstructures due to tsunami loads are basically a combination of hydrostatic and hydrodynamic pressures. The hydrostatic pressure is induced by gravity, and increases with water depth. The total force due to hydrostatic pressure is a result of imbalanced pressure, which could be considered zero when water filled up both side of the structure. The hydrodynamic pressure is induced by horizontal water velocity which is a significant factor in the tsunami events. The hydrostatic and hydrodynamic forces are considered linearly proportional to the water elevation and the flux momentum (hu^2), respectively.

The total horizontal wave-induced force on bridge superstructures presented by Douglass et al. (2006) was estimated by combining the hydrostatic pressure on the seaward external girder and the total pressure on the internal girders. The total force on the internal girders can be estimated by multiplying a reduction factor with the corresponding force on the seaward external girder. The horizontal force due to hydrostatic (Douglass et al. 2006) and hydrodynamic (Yeh 2007) pressures, therefore, can be formulated as shown in equation (5.1) and (5.2), respectively.

$$F_h = (1 + C_r (N - 1)) C_h F_h^* \quad (5.1)$$

$$F_d = 0.5 C_d \rho b (\Delta h u^2)_{max} \quad (5.2)$$

where $C_r = 0.4$ reduction coefficient for pressure on internal girders; $N =$ number of girders supporting bridge deck; $F_h^* = \gamma(\Delta h_{max})A_h$; $C_d =$ empirical drag coefficient; $C_h =$ an empirical coefficient for the horizontal “varying” load; $\rho =$ seawater mass density; and $(hu^2)_{max} =$ maximum flux momentum. The other parameters are defined in the notation section.

As mentioned earlier, the total horizontal force due to tsunami loads consists of hydrostatic force (water elevation-dependent term) and hydrodynamic force (flux momentum-dependent term). Even though the maximum of these forces might not occur exactly at the same time, combining these maximum forces together is considered reasonable (and conservative) for design purpose. Therefore, the maximum horizontal force on bridge superstructure due to tsunamis can be estimated by combining equation (5.1) and (5.2) as follows:

$$F_H = F_h + F_d = (1 + C_r(N-1)) C_h F_h^* + 0.5 C_d \rho b (\Delta h u^2)_{max} \quad (5.3)$$

An empirical drag coefficient, C_d , for bridge superstructures was evaluated in this research based on the time-history results obtained from the numerical models. A plot between the total horizontal force and flux momentum can be considered separately in two parts. The first part is where the horizontal force increases rapidly with a small change in the flux momentum (flux momentum-independent part). The second part is where the horizontal force increases proportionally to the corresponding flux momentum (flux momentum-dependent part) as shown in Figure 5.2. The empirical coefficient was estimated from the slope of the graph between flux momentum and the total horizontal force as $0.5C_d\rho b$ (= slope). Therefore, the drag coefficient was approximately 1.0 for the deck-girder bridge type.

In determination of wave forces due to wind wave and storm surge, it is recommended that the total horizontal pressure on internal girders could be estimated as 40% of the pressure on the external seaward girder. However, horizontal pressure time-history results at the bottom of bridge girders were used to evaluate an appropriate reduction coefficient for the distributed pressure on the internal girders under tsunami loads. According to Figures 5.6 to 5.8, the maximum pressure on the internal girders was approximately 20% to 50% of the corresponding pressure on the external seaward girder. Therefore, the reduction coefficient, C_r , can be used as 0.4 until further information shows a different value would be more appropriate.

A comparison between the formula estimation of maximum horizontal forces and the numerical prediction of forces calculated from the numerical models are shown in Figure 5.3. The straight line in Figure 5.3 represents a perfect fit between formula estimation of force and the numerical prediction of force. It can be observed that the formula estimation of forces could be overestimated or underestimated in some cases. A major reason for this behavior is that the recommended empirical coefficients are based on an average value of the scattering data as discussed above. The other reasons for this behavior could be: a) The values considered for drag coefficient and reduction coefficient for pressure on internal girders are approximate, b) The assumption that the maximum hydrostatic and hydrodynamic forces occur at a same time.

Note that the maximum flux momentum is calculated directly from the tsunami flow field (water surface elevation and water velocity) and controls the hydrodynamic force on bridge. This maximum flux momentum in general does not occur at a time that water free surface reaches the maximum height (maximum hydrostatic force) or the water reaches maximum velocity. Therefore, combining both maximum forces is conservative.

5.2 VERTICAL FORCES

Load effects due to tsunamis that must be considered for estimating vertical force under bridge girders consist of hydrostatic and hydrodynamic pressure. The hydrostatic pressure is induced by water elevation as mentioned earlier while the hydrodynamic pressure is induced by horizontal and vertical water velocity. The summation of formula estimation of pressures under the bridge superstructure can be estimated by equation (5.4).

$$P = \gamma(\Delta h) + 0.5\rho u_x^2 + 0.5\rho u_y^2 \quad (5.4)$$

However, the hydrodynamic force induced by the vertical component of water velocity is relatively small compared to the corresponding hydrostatic and hydrodynamic forces due to horizontal velocity; thus, it can be neglected. Consequently, the maximum vertical force due to tsunami loads can be estimated by equation (5.5).

$$F_V = [\gamma(\Delta h_{max}) + 0.5\rho u_{x,max}^2]A_v \quad (5.5)$$

As mentioned earlier, these maximum forces might not occur at exactly the same time, but it is considered conservative to combine these maximum forces together for design purpose.

Mostly, the provided tsunami flow field data – water velocity and water elevation – was based on tsunami flow without obstruction (which was a bridge superstructure in this study). The results from the numerical models showed that the water elevation and water velocity (outputs from the models) of tsunami waves near the bridge were higher than the input values. Figure 5.4 shows a plot between input value of water velocity and the output value of water velocity obtained from the numerical models. The output water velocities were measured near the bottom of the seaward external girder as pressures at this location represented up to 80% of total pressure under the bridge cross-section (explained later in this section). It can be interpreted that the output water velocity near the bridge superstructure was approximately 3.5 times the input water velocity, based on scattering data shown in Figure 5.4. The relationship between these input and output water velocities can be formulated as shown in equation (5.6).

$$u_{x,max} \approx 3.5 u_{x,max}^* \quad (5.6)$$

where $u_{x,max}$ = adjusted horizontal water velocity (output water velocity); and $u_{x,max}^*$ = input horizontal water velocity. Figure 5.5 shows a comparison between the formula estimation of maximum vertical force and the predicted maximum vertical force obtained from the simulations. The formula estimation of vertical forces were observed to be overly conservative for small values and slightly under-estimated for large values. However, the recommended equation was considered appropriate for estimating vertical force due to tsunamis.

The maximum percentage values of pressure distribution time-histories under each girder along the cross-section of the deck-girder bridges are plotted in Figure 5.6, Figure 5.7, and Figure 5.8. The pressure under the bridge girders was not uniformly distributed along the cross-section. The maximum 70% to 100% of total pressure was applied to the external seaward girder and rapidly decreased for the internal girders. However, the total vertical force, equation (5.5), was assumed to interact with the bridge at the centroid of the cross-section at this time.

5.3 DISCUSSION AND LIMITATION OF RECOMMENDED APPROACH

The recommended approach is intended to be used for estimating tsunami forces on bridge superstructures as a preliminary guidance for design. This approach was developed by incorporating the literature resources described in section 3.0 and the time-history of the tsunami forces on bridge superstructures calculated from the numerical models developed in this research. Given the uncertainties in tsunami flow field and the lack of laboratory results on realistic bridge models, an appropriate load factor should be added to these equations.

The input parameters required for estimating tsunami forces by the recommended approach consisted of maximum water elevation, horizontal water velocity, maximum flux momentum, elevation of bridge superstructure, number of girders, bridge width, and deck/beam height. Moreover, tsunami waves usually loosen sediment saturated with seawater while surging inland increasing the effective fluid density above that of typical seawater. Thus, FEMA (2008) recommended the fluid density to be equal to 1.2 times typical freshwater density for tsunami forces calculation.

The recommended empirical coefficients are given here. The recommendation for the reduction factor for forces on internal girders, C_r , is 0.4, which corresponds to that presented in Douglass et al. (2006) as the maximum fluid pressure on the internal girders ranging from 20% to 50% of the pressure on the seaward external girder. The recommendation for the drag coefficient C_d is 1, which was obtained for bridge superstructures under tsunami loads in this study. Note that the values of the empirical coefficients C_r , C_h , and C_d in equations 5.1-5.3 are based on limited experimental or numerical simulation data only, in fact some of which (C_r and C_h) were obtained from hurricane studies. These coefficients need verification using tsunami-based experiments prior to any practical applications in tsunami design.

The recommended approach was developed based on the deck-girder bridge section only. It might not be appropriate to apply these recommended equations directly to calculate tsunami forces on other types of bridge superstructures. A comparison between maximum tsunami forces on deck-girder sections and box sections (Table 4.1) showed that maximum forces on box-sections were significantly higher than those on deck-girder sections. Therefore, the box-section bridge type is not recommended to be placed in the tsunami run-up zones.

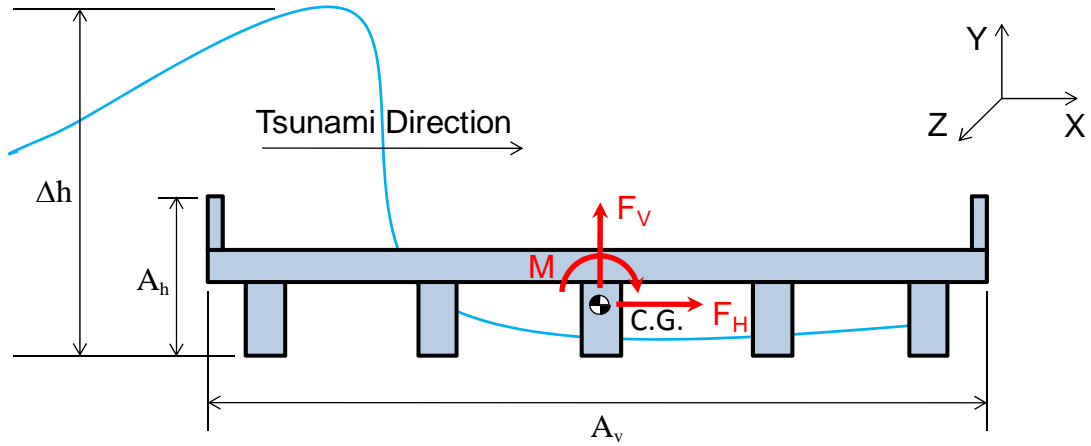


Figure 5.1: Parameters definition used in the recommended equations for estimating tsunami forces

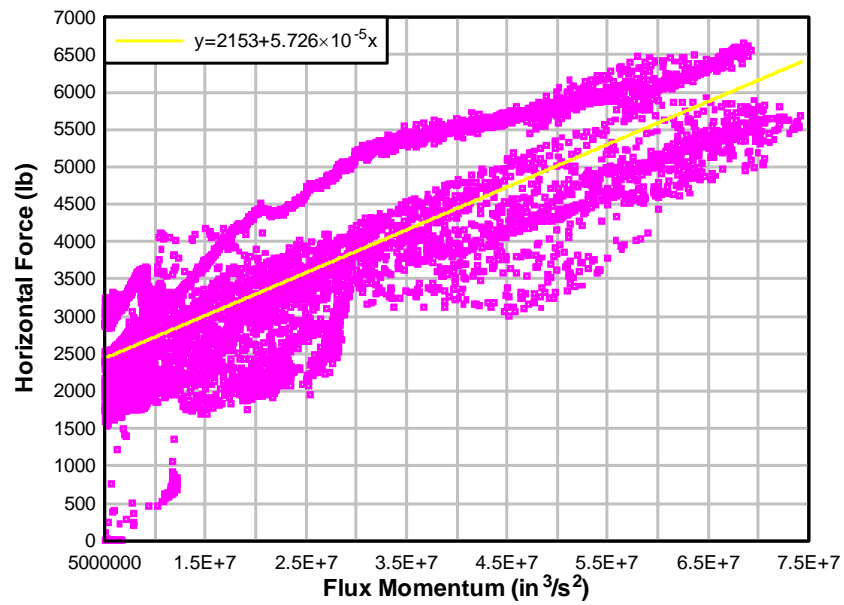


Figure 5.2: Relationship between total horizontal force and flux momentum (flux momentum-dependent part)

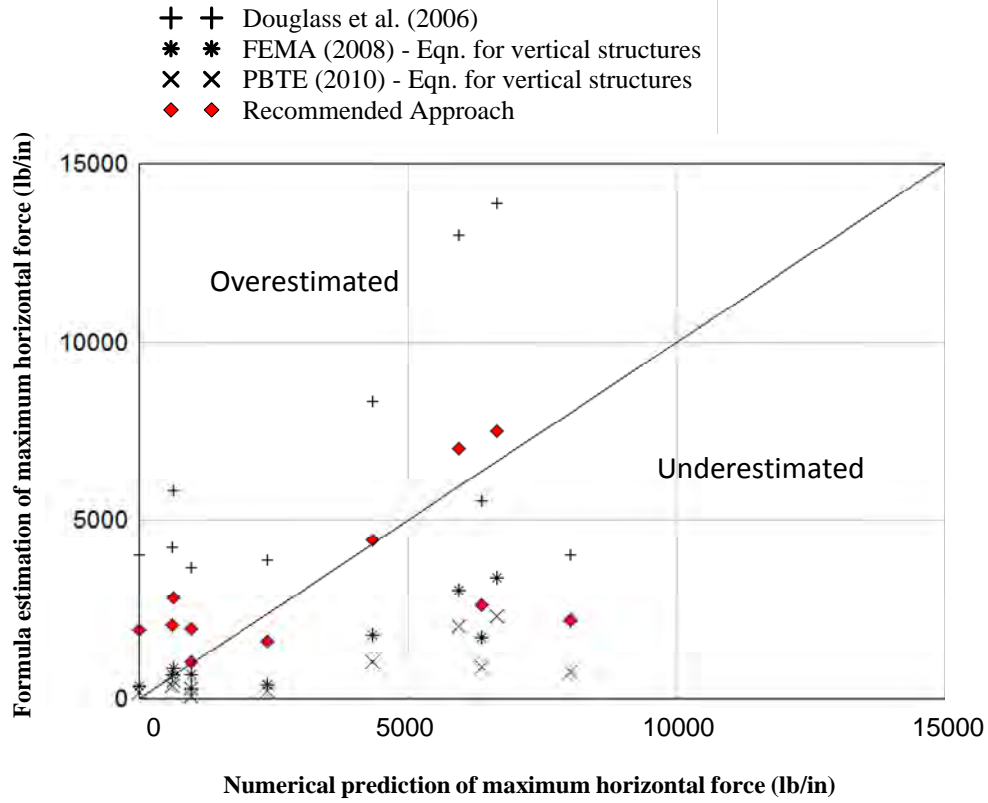


Figure 5.3: Comparison between formula estimation of maximum horizontal tsunami force and numerical prediction of maximum horizontal tsunami force

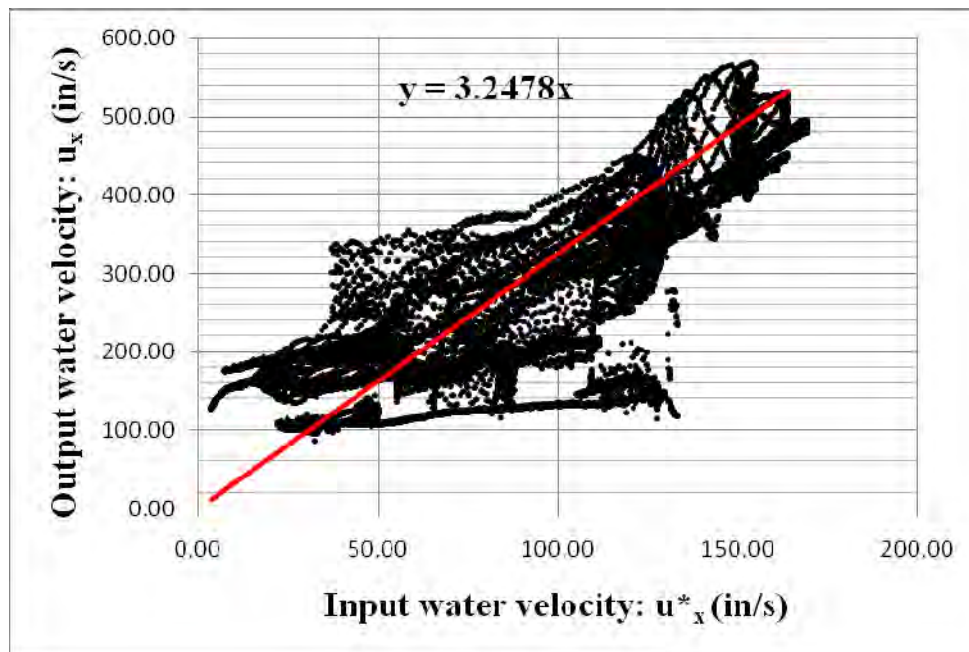


Figure 5.4: Correlation between horizontal water velocity with and without obstruction

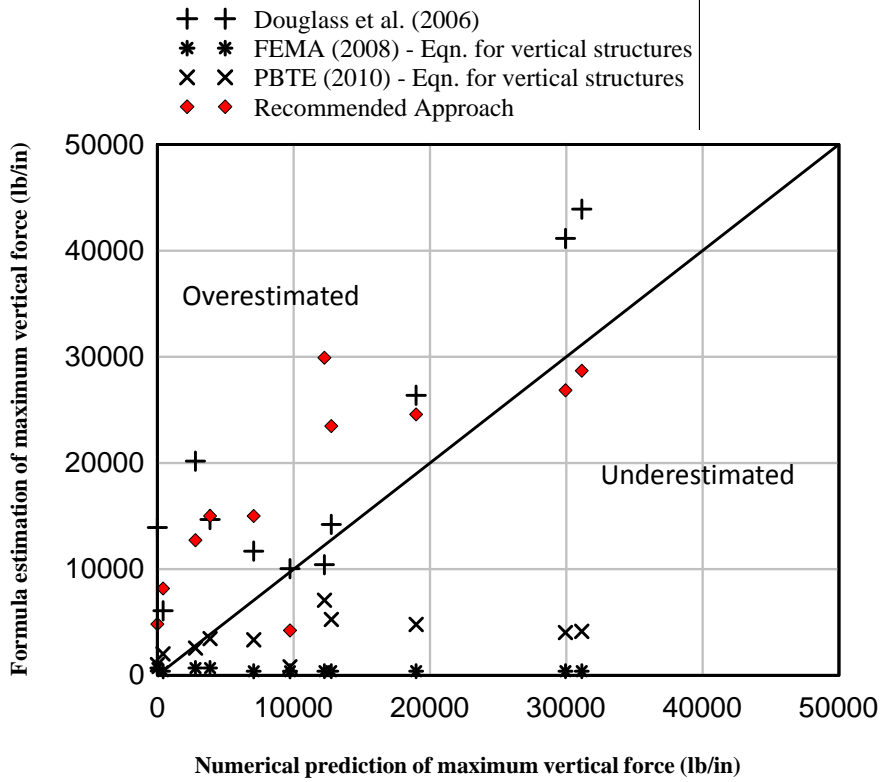


Figure 5.5: Comparison between the formula estimation of maximum vertical force and the numerical prediction of maximum vertical force

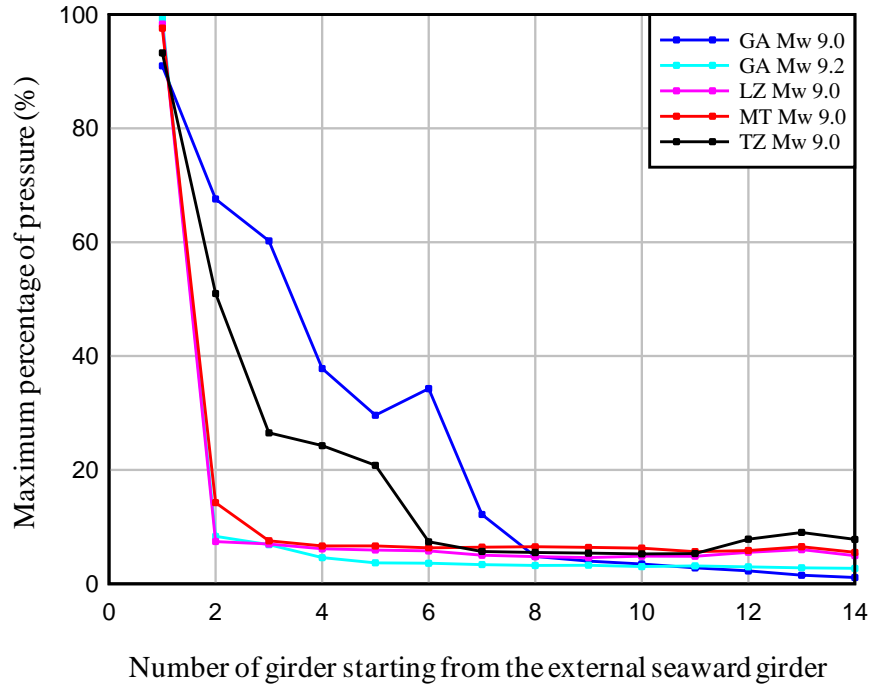


Figure 5.6: Maximum percentage of pressure distribution under each girder along the cross-section at Schooner Creek Bridge

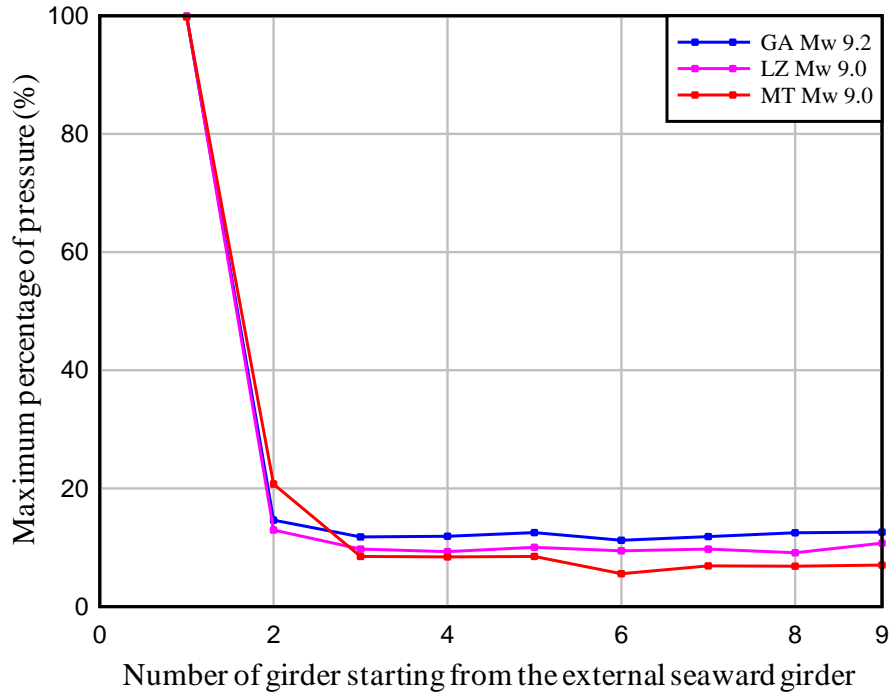


Figure 5.7: Maximum percentage of pressure distribution under each girder along the cross-section at Drift Creek Bridge

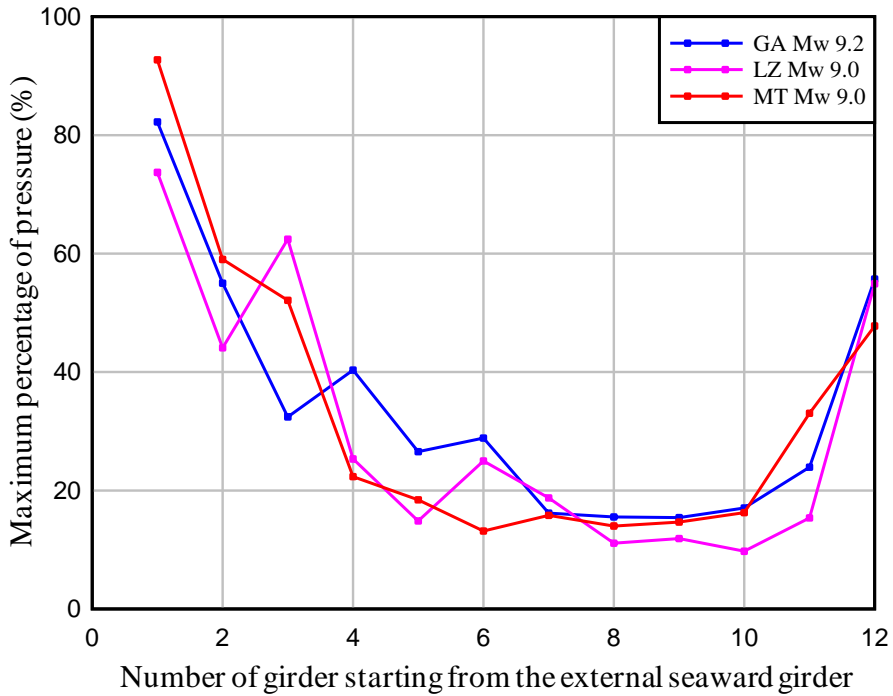


Figure 5.8: Maximum percentage of pressure distribution under each girder along the cross-section at Millport Slough Bridge

6.0 CASE STUDY OF THE SPENCER CREEK BRIDGE – REVISITED

The Spencer Creek Bridge on the Oregon Coast was analyzed in 2006 to estimate the expected forces on the bridge from tsunami inundation (Nimmala et al. 2006). It is of technical interest to revisit the Spencer Creek Bridge analysis for a more complete presentation of developing a set of guidelines for the design of coastal bridges. Firstly, this extension provides an evaluation of the guideline with regards to an application to another bridge that is at a different location and thus subjected to different tsunami loads. Secondly, it applies the recommended formulations to a bridge with a different structural configuration (with an arch-type of structure in place of longitudinal girders).

The chosen critical section for the Spencer Creek Bridge was at the middle of the longitudinal span consisting of a deck and a cross-beam. Even though the recommended approach (in this report) for estimating tsunami forces on the bridge superstructures was developed for the deck-girder bridge type only, similar logic can be applied to the deck of the Spencer Creek Bridge with modified coefficients.

Since there was no girder supporting the bridge deck in this case, the term that accounts for additional horizontal force on internal girders was set to zero; i.e., it can be considered that the bridge superstructure consisted of a deck with one girder ($N = 1$). Therefore, equation (5.3) was modified as follows:

$$F_H = \gamma(\Delta h_{max})A_h + 0.5 C_d \rho b (\Delta h u^2)_{max} \quad (6.1)$$

Other than setting the number of girders equal to one, the empirical drag coefficient, C_d , was modified for this case because the recommended value provided in Section 5.0 was determined based on the tsunami forces of deck-girder bridge types. Considering the numerical results of the tsunami impact on the Spencer Creek Bridge from Nimmala et al. (2006), the drag coefficient was calculated by taking $C_d = 2 \times F_H / (\rho b u^2)$. Thus the recommended drag coefficient for the Spencer Creek Bridge was 3.5 as shown in Figure 6.1. Consequently, the formula estimation of maximum horizontal force due to tsunami loads on the Spencer Creek Bridge deck calculated by equation (6.1) was approximately 18 kip/ft while the numerical prediction of maximum force was approximately 23 kip/ft (Nimmala et al. 2006). Note that the drag coefficient used to estimate the maximum horizontal force was based on a single set of data only; therefore, additional data is required to confirm the appropriateness of the drag coefficient for this type of bridge.

The equation for estimating maximum vertical force, equation (5.5), was directly applied to the Spencer Creek Bridge. Unlike the deck-girder bridge type, an observation from the numerical model of the Spencer Creek Bridge showed that the local velocity near the bridge support was approximately equal to the input value of water velocity ($u_x \cong 1.0 u_x^*$) which can be directly used in equation (5.5). Consequently, the formula estimation of maximum vertical force due to

tsunami loads on the Spencer Creek Bridge deck was approximately 67 kip/ft while the numerical prediction of maximum vertical force was approximately 40 kip/ft. An example calculation of tsunami forces on the Spencer Creek Bridge using the recommended approach is shown in Appendix C.

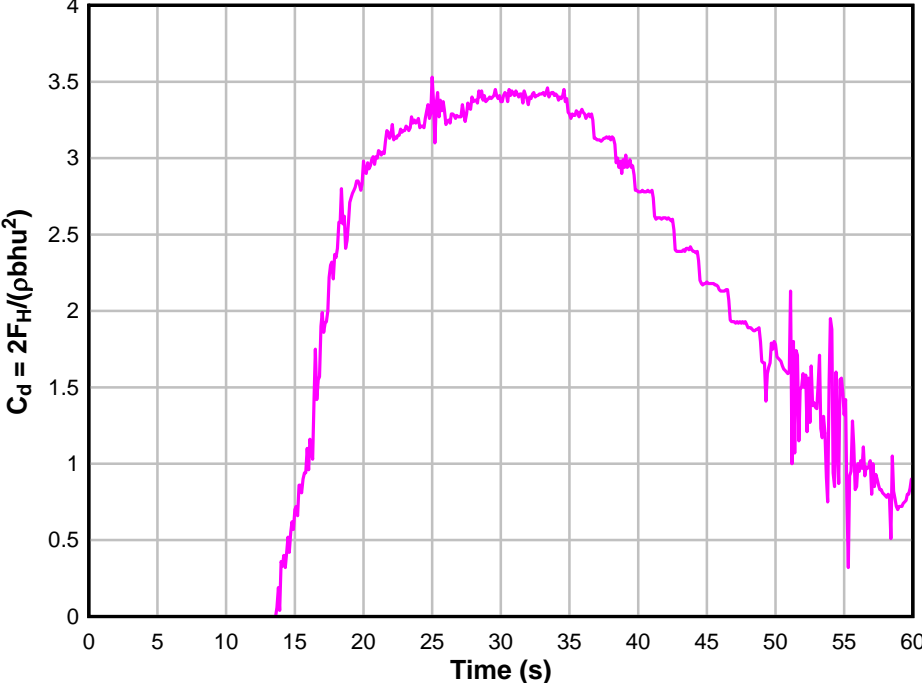


Figure 6.1: Empirical drag coefficients for Spencer Creek Bridge

7.0 ACCURACY COMPARISON OF THE RECOMMENDED APPROACH WITH OTHER EXISTING METHODS

Table 7.1 to Table 7.6 show the maximum values of horizontal and vertical forces on the bridges due to different tsunami scenarios. These values are based on Numerical results from LS-DYNA and estimated values using the methods provided by Douglass et al. (2006), FEMA (2008), PBTE (2010), and Recommended Approach. Table 7.7 shows the maximum values of horizontal and vertical forces on the Spencer Creek Bridge.

The relative errors of the estimated values are provided in Table 7.8 to Table 7.14. In these calculations it was assumed the numerical results computed using LS-DYNA are the exact values.

Table 7.1: Maximum values of horizontal forces on the Schooner Creek Bridge due to different tsunami scenarios

Tsunami scenario	Maximum horizontal forces (Lb/in)					
	LS-DYNA		Douglass et al. (2006)	FEMA (2008)	PBTE	Recommended Approach
	Deck-girder	Box section				
GA Mw 9.0	967.5	12500	1923.44	275.57	75.46	1001.06
GA Mw 9.2	6661.93	12500	13867.44	3397.45	2304.09	7499.54
LZ Mw 9.0	5933.25	16666.6	12997.35	3046.47	2022.76	7001.43
MT Mw 9.0	4343.8	19166.6	8330.28	1792.56	1005.52	4455.37
TZ Mw 9.0	4091	15833.3	3693.53	680.077	265.58	1952.50

Table 7.2: Maximum values of vertical forces on the Schooner Creek Bridge due to different tsunami scenarios

Tsunami scenario	Maximum vertical forces (Lb/in)					
	LS-DYNA		Douglass et al. (2006)	FEMA (2008)	PBTE	Recommended Approach
	Deck-girder	Box section				
GA Mw 9.0	418.3	50000	6090.52	388.37	2017.46	8183.57
GA Mw 9.2	31136.31	60000	43910.92	393	4146.72	28691.7
LZ Mw 9.0	29938.44	70000	41155.8	394.9	4031.73	26850.86
MT Mw 9.0	18984.39	57083.3	26377.6	390.4	4792.15	24585.35
TZ Mw 9.0	10302	52500	11695.47	388.6	3346.85	15013.16

Table 7.3: Maximum values of horizontal forces on the Millport Slough Bridge due to different tsunami scenarios

Tsunami scenario	Maximum horizontal forces (Lb/in)				
	LS-DYNA	Douglass et al. (2006)	FEMA (2008)	PBTE	Recommended Approach
GA Mw 9.2	602.9	4243.8	665.2	362	2068.82
LZ Mw 9.0	625.7	5833.59	852.96	498.65	2831.52
MT Mw 9.0	0	4027.49	365.58	192.22	1910.22

Table 7.4: Maximum values of vertical forces on the Millport Slough Bridge due to different tsunami scenarios

Tsunami scenario	Maximum vertical forces (Lb/in)				
	LS-DYNA	Douglass et al. (2006)	FEMA (2008)	PBTE	Recommended Approach
GA Mw 9.2	3866.49	14679	684.7	3463	15016.9
LZ Mw 9.0	2797.9	20177.93	685.52	2565.32	12725.75
MT Mw 9.0	0	13930.8	684.28	1013.6	4827.8

Table 7.5: Maximum values of horizontal forces on the Drift Creek Bridge due to different tsunami scenarios

Tsunami scenario	Maximum horizontal forces (Lb/in)				
	LS-DYNA	Douglass et al. (2006)	FEMA (2008)	PBTE	Recommended Approach
GA Mw 9.2	8026	4047.28	2185.99	745.9	3118.17
LZ Mw 9.0	6366.45	5520.86	1703.36	887.7	2621.93
MT Mw 9.0	2381.75	3900.93	393.4	226.89	1608.46

Table 7.6: Maximum values of vertical forces on the Drift Creek Bridge due to different tsunami scenarios

Tsunami scenario	Maximum vertical forces (Lb/in)				
	LS-DYNA	Douglass et al. (2006)	FEMA (2008)	PBTE	Recommended Approach
GA Mw 9.2	12257.9	10422.69	391.2	7073.61	29912.58
LZ Mw 9.0	12761.19	14217.52	392.33	5264.91	23475.75
MT Mw 9.0	9729.17	10045.82	386.25	807.61	4232.20

Table 7.7: Maximum values of horizontal and vertical forces on the Spencer Creek Bridge

Maximum horizontal forces (Lb/ft)				
LS-DYNA	Douglass et al. (2006)	FEMA (2008)	PBTE	Recommended Approach
23000	18000	23970	8395	17550
Maximum vertical forces (Lb/ft)				
40000	91530	21850	48880	67020

Table 7.8: Computed relative error of horizontal forces on the Schooner Creek Bridge for different methods

Tsunami scenario	Relative Error (%)			
	Douglass et al. (2006)	FEMA (2008)	PBTE	Recommended Approach
GA Mw 9.0	98.8	71.5	92.1	3.4
GA Mw 9.2	108.1	49.0	65.4	12.5
LZ Mw 9.0	119.0	48.6	65.9	18.0
MT Mw 9.0	91.7	58.7	76.8	2.5
TZ Mw 9.0	9.71	83.3	93.5	52.2

Table 7.9: Computed relative error of vertical forces on the Schooner Creek Bridge for different methods

Tsunami scenario	Relative Error (%)			
	Douglass et al. (2006)	FEMA (2008)	PBTE	Recommended Approach
GA Mw 9.0	1355.9	7.1	382.2	1856.3
GA Mw 9.2	41.0	98.7	86.6	7.8
LZ Mw 9.0	37.4	98.6	86.5	10.3
MT Mw 9.0	38.9	97.9	74.7	29.5
TZ Mw 9.0	13.5	96.2	67.5	45.7

Table 7.10: Computed relative error of horizontal forces on the Millport Slough Bridge for different methods

Tsunami scenario	Relative Error (%)			
	Douglass et al. (2006)	FEMA (2008)	PBTE	Recommended Approach
GA Mw 9.2	603.8	10.3	39.9	243.1
LZ Mw 9.0	832.2	36.3	20.3	352.4
MT Mw 9.0	-	-	-	-

Table 7.11: Computed relative error of vertical forces on the Millport Slough Bridge for different methods

Tsunami scenario	Relative Error (%)			
	Douglass et al. (2006)	FEMA (2008)	PBTE	Recommended Approach
GA Mw 9.2	279.6	82.2	10.4	288.3
LZ Mw 9.0	621.1	75.4	8.3	354.8
MT Mw 9.0	-	-	-	-

Table 7.12: Computed relative error of horizontal forces on the Drift Creek Bridge for different methods

Tsunami scenario	Relative Error (%)			
	Douglass et al. (2006)	FEMA (2008)	PBTE	Recommended Approach
GA Mw 9.2	49.5	72.7	90.7	61.1
LZ Mw 9.0	13.2	73.2	86.0	58.8
MT Mw 9.0	63.7	83.4	90.4	32.4

Table 7.13: Computed relative error of vertical forces on the Drift Creek Bridge for different methods

Tsunami scenario	Relative Error (%)			
	Douglass et al. (2006)	FEMA (2008)	PBTE	Recommended Approach
GA Mw 9.2	14.9	96.8	42.2	144.0
LZ Mw 9.0	11.4	96.9	58.7	83.9
MT Mw 9.0	3.2	96.0	91.6	56.4

Table 7.14: Computed relative error of horizontal and vertical forces on the Spencer Creek Bridge
Relative Error of horizontal forces (%)

Douglass et al. (2006)	FEMA (2008)	PBTE	Recommended Approach
21.7	4.2	63.5	23.6

Relative Error of vertical forces (%)

128.8	45.3	22.2	67.5
-------	------	------	------

According to these tables, the relative error of the recommended approach in estimating the horizontal and vertical forces on the Schooner Creek Bridge is considerably less than the other methods. For the other three bridges, Millport Slough Bridge, Drift Creek Bridge, and Spencer Creek Bridge, the relative error of the recommended approach is slightly less than the other methods; therefore, some modifications should be applied to the recommended approach.

8.0 COMPUTATIONAL PERFORMANCE

This section presents a performance study of the numerical code (LS-DYNA) by performing Fluid-Structure Interaction (FSI) simulation models on a high-performance computing system. In this study, the parallel cluster system consisted of 1,100 two-processor socket dual-core computer nodes with 8 GB of memory each. The core processor specification on parallel cluster was 4,400 with 3.0 GHz Intel Woodcrest.

Three FSI models with different finite element nodes – 12k, 30k, and 48k nodes – were tested with 20 seconds termination time. The test was conducted by recording the computational time required to run each FSI model with a varying number of computer CPUs (CPU node). The purpose of this study was to determine an optimal number of CPUs for calculating the FSI problem with LS-DYNA software on a high performance computer system. The consumed computational time for each simulation is summarized in Table 8.1.

A comparison between the computational time and the number of CPUs of three different FSI models are plotted in Figure 8.1. The number of CPU axis (x-axis) is shown in log scale for a better demonstration purpose. Based on Figure 8.1, the computational time decreased rapidly as the number of CPUs increased at the small number of CPU and continued to decrease slowly until reaching its optimal point. It can be observed that using CPUs more than the optimal number could increase the computational time for running these models. The optimal number of CPUs for Model 1 and Model 2 were approximately at 32 CPU nodes while the optimal number of CPUs for Model 3 was approximately at 64 nodes. However, the computational time used for simulating Model 1 with 16 CPU nodes was only slightly higher than using 32 CPUs as shown in Table 8.1. Thus, it might be more appropriate to use 16 CPU nodes for simulating Model 1 considering the cost of computational time. Furthermore, relationships between computational time, unit cost, and number of CPUs are shown in Figure 8.2. It can be observed that by considering the computational time along with the unit cost, the optimal number of CPUs for all three models was 16 nodes.

According to this performance study, it can be concluded that an appropriate number of CPUs for simulating a FSI problem by the simulation code depends on the size of each FSI model. Moreover, the optimal number of CPU for a small model (Model 1: 12k) is smaller than the optimal number of CPU for a large model (Model 3: 48k).

Table 8.1: Summary of computational time

Number of CPUs	Computational Time (min)		
	Model 1: 12k	Model 2: 30k	Model 3: 48k
2	863.3	2382.7	3675.7
4	436.9	1210.6	1792.6
8	244.6	647.6	933.7
16	161.2	388.9	502
32	158.2	278.9	333.2
64	196.6	303.3	313
128	379.3	461.9	466.8

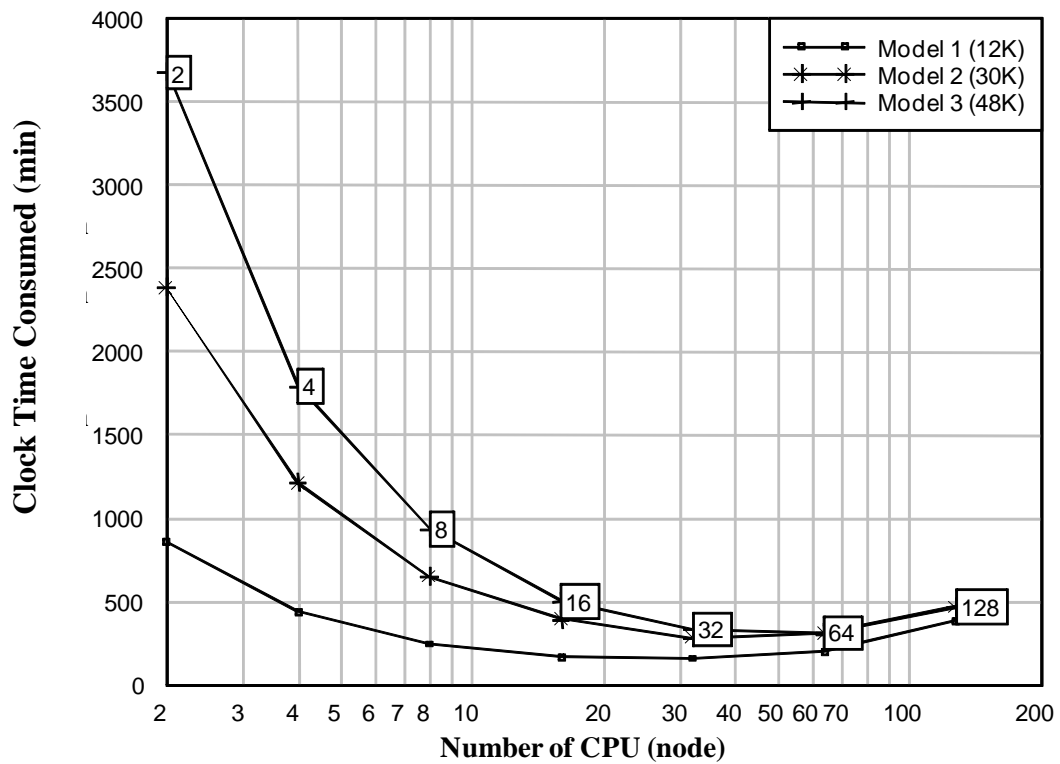


Figure 8.1: Relationships between consumed computational time and number of computer CPUs

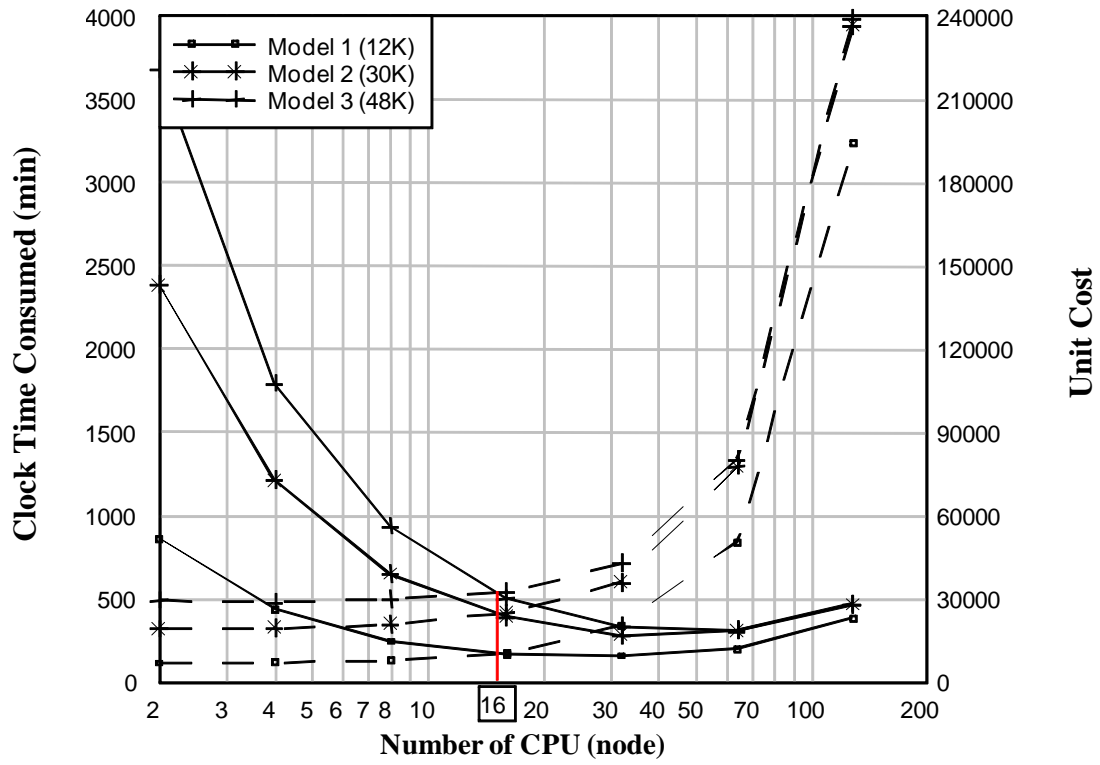


Figure 8.2: Relationships between computational time, unit cost, and number of computer CPUs

9.0 CONCLUDING REMARKS

Bridges along the Oregon coast are an important part of the transport system in the area; however, they were not designed to resist large tsunami loads. Based on the studies of tsunami deposits, there is a high possibility that large tsunamis could occur in the vicinity of the Oregon Coast. To understand the magnitude of the forces that could act on bridges from tsunami inundation, ODOT initiated a research program to perform a tsunami vulnerability study on four bridges in the Siletz bay area in Oregon.

This study was divided into two major parts. The first part developed numerical models to perform numerical testing of tsunami impact on full-scaled bridge superstructures. The provided tsunami flow fields at each bridge location consisted of six different scenarios based on rupture configurations and earthquake moment magnitudes. However, the maximum elevations of wave crest in some scenarios were lower than the reference bridge elevation; therefore, only the cases in which the maximum wave crest elevation was higher than the reference elevation were selected to perform the numerical testing. The selected tsunami scenarios consisted of five scenarios at Schooner Creek, and three scenarios at Drift Creek and Millport Slough. At the Schooner Creek, two different bridge superstructure cross-sections, deck-girder and box section, were developed to perform numerical testing subjected to identical tsunami flow field. The time-history of the numerical results showed that, given identical tsunami conditions, box section bridges were subjected to significantly larger forces (both horizontal and vertical forces) than deck-girder section bridges. Therefore, it would be more appropriate to select deck-girder section bridges in the tsunami run-up zone instead of a box section. Furthermore, the effect of bridge rails on tsunami forces was examined in this research. The results showed that rigid rails on the superstructure could increase horizontal and vertical tsunami forces up to 20% and 15%, respectively.

The second part of this study was to develop a guideline to estimate tsunami forces on a bridge superstructure. The guideline was developed based on a review of wave force related literature and time-history results obtained from numerical models conducted in the first part of this research. The horizontal force due to tsunamis was considered to be linearly proportional to the water elevation and the flux momentum ($F_H \propto \Delta z$; $F_H \propto (\Delta z)u_x^2$), while the vertical force was linearly proportional to the water elevation and the square of water velocity in the horizontal direction ($F_V \propto \Delta z$; $F_V \propto (\Delta z)u_x^2$). The water pressure due to water velocity in the vertical direction was relatively small compared to the pressure due to water elevation and the water velocity in horizontal direction; thus, the vertical water velocity was neglected. The recommended approach provided simplified equations for estimating tsunami forces due to fluid loads only. Impact force from floating objects was not included in these equations.

The recommended approach was developed to be used as a preliminary guideline for design engineers. An appropriate load factor should be incorporated into these equations in design given uncertainties in the tsunami flow fields and lack of laboratory experiments on realistic bridge models to validate the numerical results.

10.0 FUTURE RESEARCH

The current study was developed based on tsunami time-history loads calculated from finite-element models without verification with laboratory test data. A recommendation for future research is to perform laboratory experiments of tsunami impact on bridge superstructures and compare the test results with the numerical predictions. Furthermore, the numerical models developed in this study were two-dimensional. The longitudinal span lengths of the bridges were not taken into account. Three-dimensional models of tsunami impact on bridge superstructures should be developed for a better understanding of an interaction between them and to study the effect of longitudinal span length in computing the tsunami forces. Other than total tsunami forces on bridge superstructure, force distribution on each girder along the cross-section could be evaluated for a better design aspect by tracking reaction forces at connections between the deck and girders in the future model.

The recommended approach for estimating the tsunami forces on bridge decks was developed as a preliminary guidance for design of new bridges in the tsunami run-up zone and for performing a tsunami vulnerability study of the existing bridges as well. A survey of the tsunami vulnerability for existing bridges should be conducted to initiate plans for retrofit, or replacement if necessary, of these bridges to be able to withstand possible tsunami events.

11.0 REFERENCES

- Bea, R.G., T. Xu, J. Stear, and R. Ramos. Wave Forces on Decks of Offshore Platforms. *Journal of Waterway, Port, Coastal and Ocean Engineering*, 1999, pp. 136-144.
- Cheung, K.F., Y. Wei, Y. Yamazaki, and S. C. Yim. *Modeling of 500-year Tsunamis for Probabilistic Design of Coastal Infrastructure in the Pacific Northwest*. Coastal Engineering, 2011, In Press.
- Cuomo, G., K. Shimosako., and S. Takahashi. *Wave-in-deck loads on coastal bridges and the role of air*. Coastal Engineering, 2009, pp. 793-809.
- Dalrymple, R.A. and B.D. Rogers, Numerical Modeling of Water Waves with the SPH Method. Coastal Engineering, 2006, 53/2-3, 141-147.
- Douglass, S.L., Q. Chen, and J. M. Olsen. *Wave Forces on Bridge Decks*. FHWA, Washington, 2006.
- FEMA P646. *Guidelines for Design of Structures for Vertical Evacuation from Tsunamis*. Federal Emergency Management Agency, Washington, D.C., 2008.
- Goldfinger, C. *Deep-water turbidites as Holocene earthquake proxies: the Cascadia subduction zone and Northern San Andreas Fault systems*. Annals of Geophysics, 2003, pp. 1169-1194.
- Munger, S., and K.F. Cheung. Resonance in Hawaii waters from the 2006 Kuril Islands Tsunami. *Geophysical Research Letters*, Vol. 35, No. 7, L07605, Doi: 10.1029/2007GL032843, 2008.
- Nimmala, S.B., S.C. Yim, K.F. Cheung, and W. Yong. *Tsunami Design Criteria for Coastal Infrastructure: A case study for Spencer Creek Bridge, Oregon*. Oregon Department of Transportation (ODOT), 2006.
- PBTE. Riggs, R., G. Chock, I. Robertson, and S.C. Yim. *Development of Performance-Based Tsunami Engineering*. NEES Presentation, 2010.
- Petersen, M.D., A.D. Frankel, S.C. Harmsen, C.S. Mueller, K.M. Haller, R.L. Wheeler, R.L. Wesson, Y. Zeng, O.S. Boyd, D.M. Perkins, N. Luco, E.H. Field, C.J. Wills, and K.S. Rukstales. *Documentation for the 2008 Update of the United States National Seismic Hazard Maps*. US Geological Survey, Open-file Report 2008-1128. 2008.
- Peterson, C.D., M.E. Darienzo, S.F. Burns, and W.K. Burris. Field trip guide to Cascadia paleoseismic evidence along the northern Oregon coast: Evidence of subduction zone seismicity in the central Cascadia margin. *Oregon Geology*, Vol. 55, No. 5, 1993, pp. 99-114.

Roeber, V., Y. Yamazaki, and K.F. Cheung. Resonance and impact of the 2009 Samoa tsunami around Tutuila, American Samoa. *Geophysical Research Letters*, Vol. 37, No. 21, L21604, doi: 10.1029/2010GL044419, 2010.

Tichelaar, B.W., and L.J. Ruff. Depth of seismic coupling along subduction zone. *Journal of Geophysical Research*, 1993, pp. 15829-15831.

Wang, K., R. Wells, S. Mazzotti, R.D. Hyndman, and T. Sagiya. A revised dislocation model of interseismic deformation of the Cascadia subduction zone. *Journal of Geophysical Research*, 108(B1), 2026, doi: 10.1029/2001JB001227, 2003.

Yamazaki, Y., and K.F. Cheung. Shelf resonance and impact of near-field tsunami generated by the 2010 Chile earthquake. *Geophysical Research Letters*, Vol. 38, doi: 10.1029/2011GL047508, 2011, In press.

Yamazaki, Y., Z. Kowalik, and K.F. Cheung. Depth-integrated, non-hydrostatic model for wave breaking and runup. *International Journal for Numerical Methods in Fluids*, Vol. 61, No. 5, 2009, pp. 473-497.

Yeh, H. Design Tsunami Forces for Onshore Structure. *Journal of Disaster Research* Vol. 2, No.6, 2007, pp. 531-536.

Yeh, H., I. Robertson, and J. Preuss. *Development of Design Guidelines for Structures that Serve as Tsunami Vertical Evacuation Sites*. Washington State Department of Natural Resources, Olympia, WA, 2005

**APPENDIX A:
SIMULATION MODELS**

A-1 MODEL BOUNDARY CONDITIONS

The two dimensional model can be thought of as a three dimensional rectangular box model with one-inch thickness in the z-direction. The box is composed of water and air material parts with a bridge part inside. Boundary conditions of the box must be specified correctly at eight corner nodes, eight edges, two surfaces of the box, and the connection between water and air material to prevent leakage of fluid materials. The eight corner nodes of the water part are constrained in x, y, and z translational. Four edges aligned along x-axis are constrained in y and z translational. Two edges aligned along y-axis at the water part and two edges at the connection between the water and air parts are constrained in x and z translational. Nodes on two x-y plane surfaces are constrained in z translational. Nodes on two edges along y-axis at the right border of the air material part must not be constrained in x translational as they are intentionally left as an open channel for water and air to flow out. A demonstration of the boundary set up is shown in Figure A.1. Fluid elements on this open channel, orange area in Figure A.1, are specified as a non-reflecting boundary condition to prevent leakage of water from the open channel at the beginning of the simulation and still allow water and air to flow out freely. Note that general parameters and formulations set up in each simulation model are similarly specified for all three bridges. The differences between each model are bridge cross-section and the input tsunami flow fields.

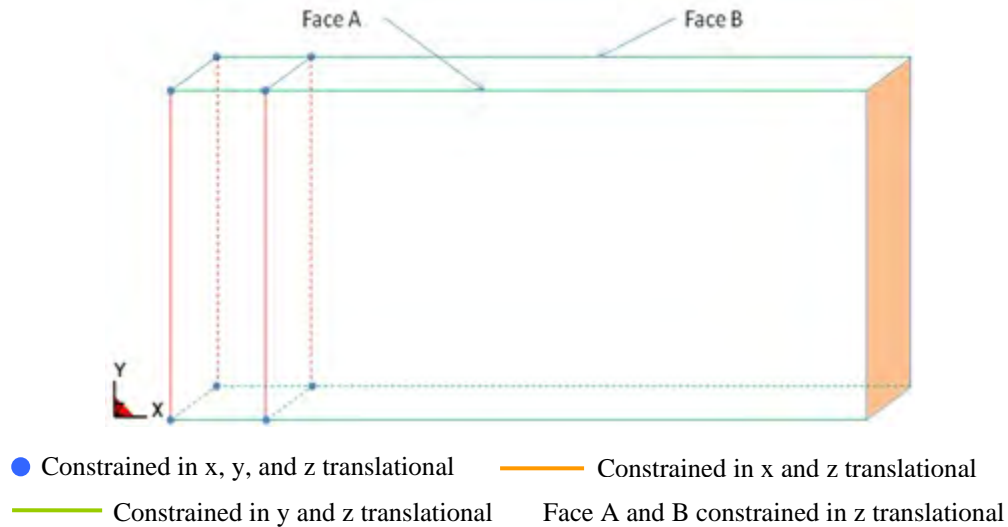


Figure A.1: Boundary conditions

A-2 MODEL CONSTRUCTION

As mentioned earlier, a numerical model consists of two major material parts: a fluid-like part (water and air), and a rigid structure part (bridge). The unit system used in construction of the numerical models is the English system for convenience of design engineers. The FSI numerical models were analyzed by an ALE solver provided in LS-DYNA. The ALE solver involves a Lagrangian step followed by an advection step. The advection step stops the calculation when

mesh distortion has occurred and then smoothes the mesh. After the smoothing mesh process, it remaps the solution from the distorted to smoothed meshes. By using a combination of the Lagrangian-Eulerian coupling algorithm and the ALE solver, the interaction between a Lagrangian material (Bridge) and an Eulerian material (Fluid: water and air) could be taken care of.

The Eulerian fluid parts (water and air) are generally modeled using *MAT_NULL and an accompanying equation of state (*EOS) as recommended by LS-DYNA user manual. The null material was chosen to represent the fluid material because it has no yield strength and behaves in a fluid-like manner.

The equation of state has to be specified along with the fluid-like materials to simulate their behaviors of water and air. The fluid properties of water are usually defined by the bulk modulus of the water. The relation between the change of volume and pressure was assumed to be linear in this study. Therefore, *EOS LINEAR POLYNOMIAL keyword card is used in development of the numerical model. The fluid pressure is given by the following equation:

$$P = C_0 + C_1\mu + C_2\mu^2 + C_3\mu^3 + (C_4 + C_5\mu + C_6\mu^2) E$$

where $\mu = (\rho/\rho_0) - 1$, and ρ_0 is a reference density defined in the *MAT_NULL keyword card. Due to the linear assumption, the constant parameter of the nonlinear term is assumed to be zero. Therefore, the pressure is now given by:

$$P = C_1\mu$$

where C_1 is the bulk modulus of water.

$$C_1 = \rho \times c^2$$

where ρ is density of the water, and c is the speed of sound in the water.

Note that the choice of speed of sound in the water could affect the integration time step in the calculation. In the study of the smoothed particle hydrodynamics (SPH) modeling of wave propagation by Dalrymple and Rogers (2006), it was concluded that the speed of sound could be set lower than its average value without affecting the accuracy of fluid motion but could significantly reduce the computation time by increasing the integration time step. The paper suggests that the minimum modified speed of sound should be about ten times greater than the maximum expected water flow speed. However, a very small speed of sound could cause stiffness problems in computation in LS-DYNA.

To model an air material in the simulation model, there are two alternative ways to specify the equation of state along with the null material to simulate the behavior of air. The first way is to use *EOS_LINEAR_POLYNOMIAL keyword card. The second way is to use *EOS_IDEAL_GAS keyword card. The *EOS_LINEAR_POLYNOMIAL was used in this research with the gamma law equation of state by setting

$$C_4 = C_5 = \gamma - 1$$

where γ is the ratio of specific heat capacity, and set other parameters to be zero.

Numerical models of the bridge superstructures are demonstrated in Figure A.2 to Figure A.4. The selected input tsunami conditions – water surface elevation and horizontal velocity of water – are shown in Figure A.5 to Figure A.15.

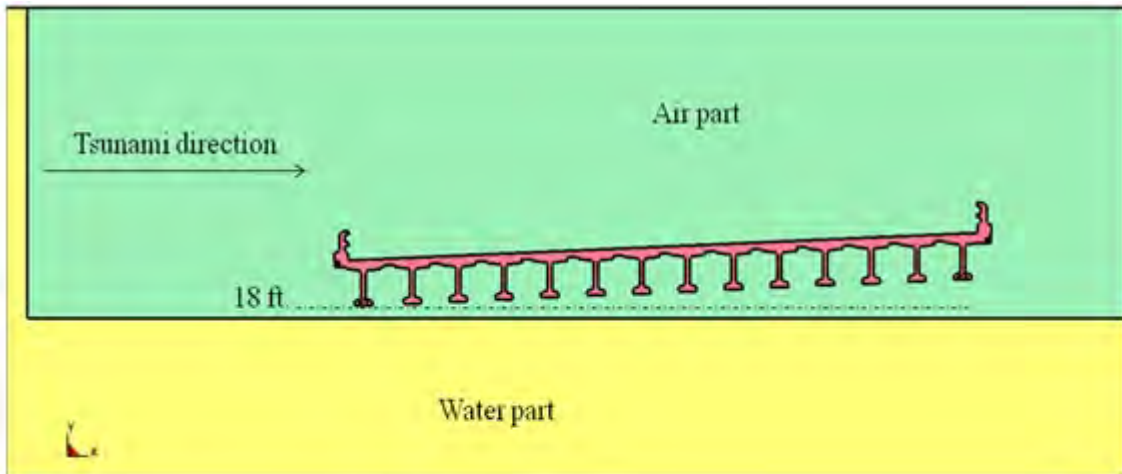


Figure A.2: Simulation model of Schooner Creek Bridge (deck-girder) cross-section with one-inch thickness in z-direction

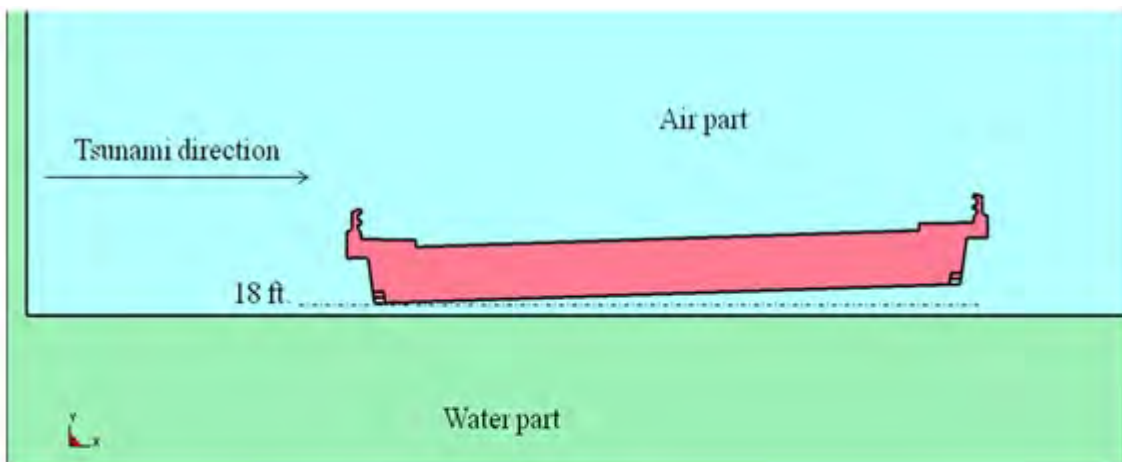


Figure A.3: Simulation model of Schooner Creek Bridge (box-section) cross-section with one-inch thickness in z-direction

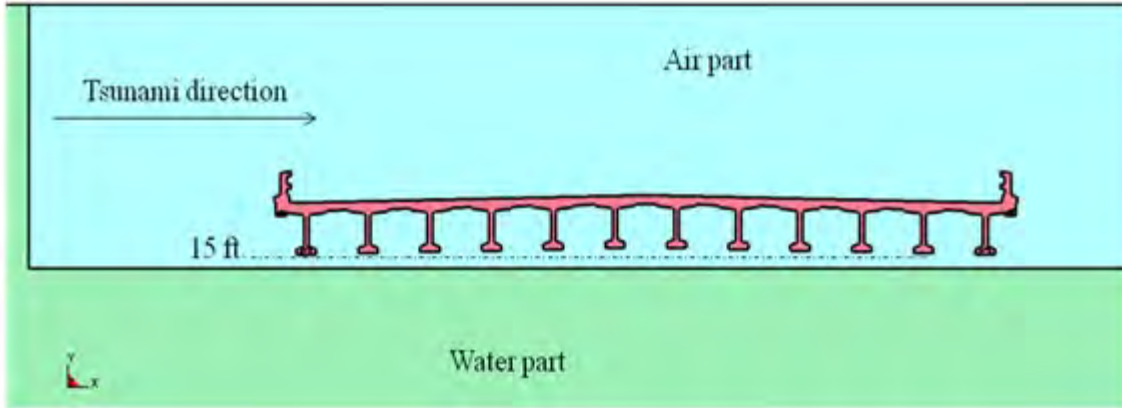


Figure A.4: Simulation model of Millport Slough Bridge cross-section with one-inch thickness in z-direction

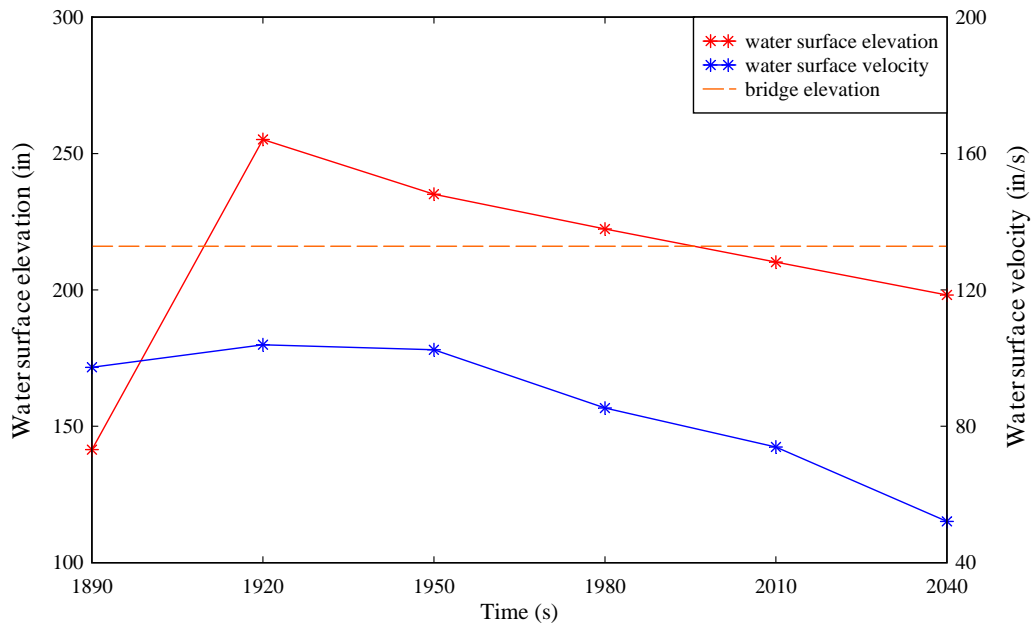


Figure A.5: Input conditions for simulation models of Schooner Creek Bridge under GA Mw 9.0 tsunami scenario

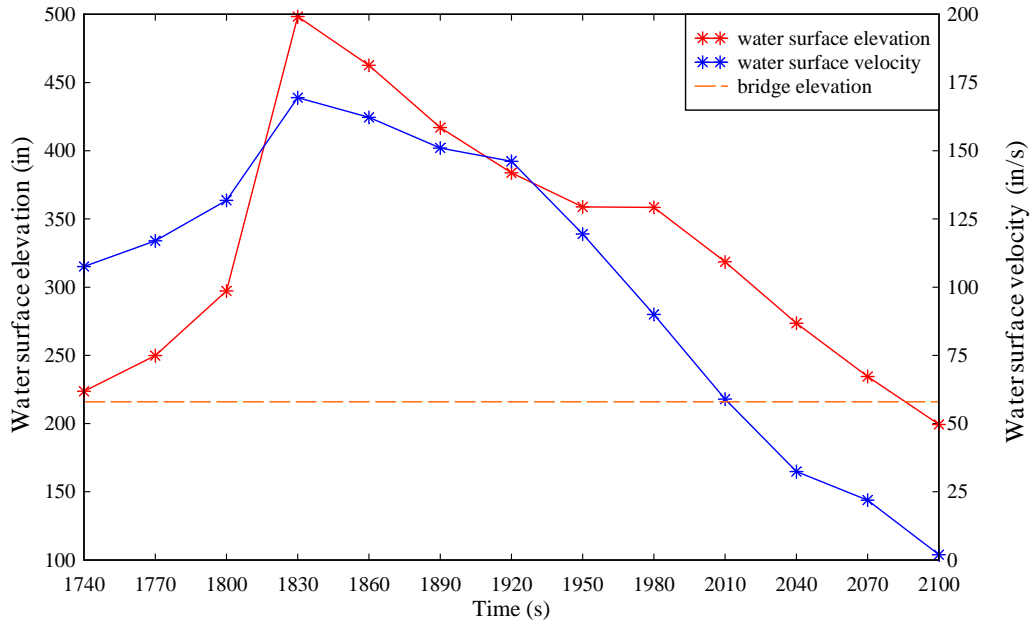


Figure A.6: Input conditions for simulation models of Schooner Creek Bridge under GA M_w 9.2 tsunami scenario

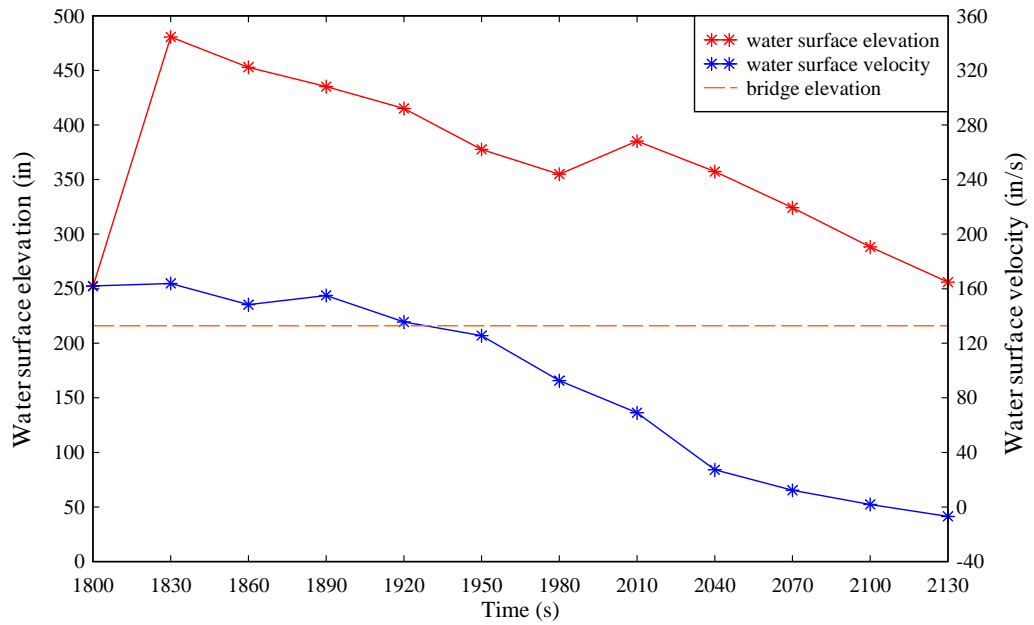


Figure A.7: Input conditions for simulation models of Schooner Creek Bridge under LZ M_w 9.0 tsunami scenario

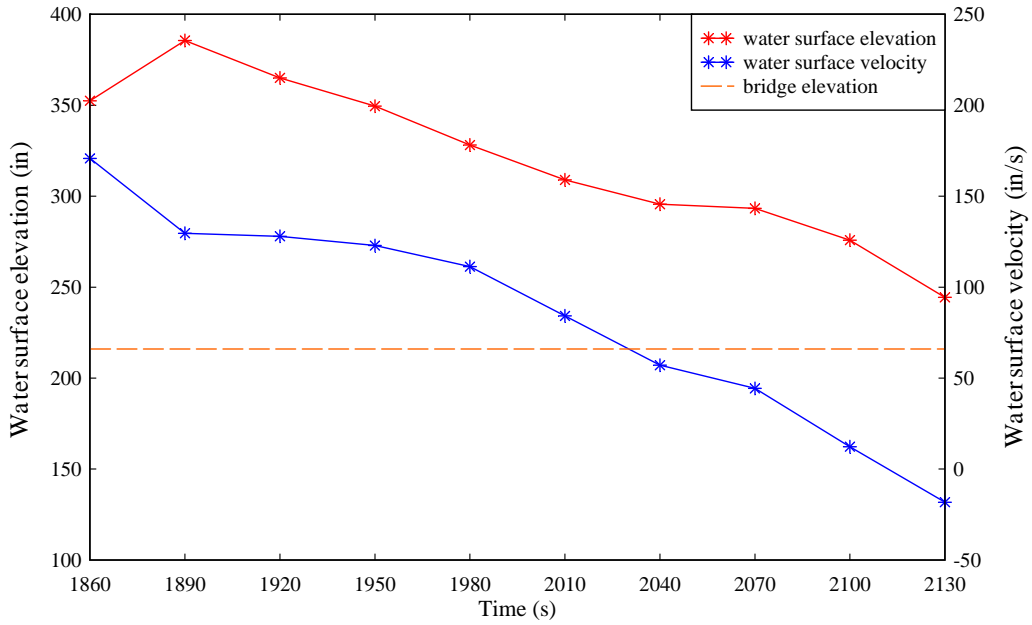


Figure A.8: Input conditions for simulation models of Schooner Creek Bridge under MT M_w 9.0 tsunami scenario

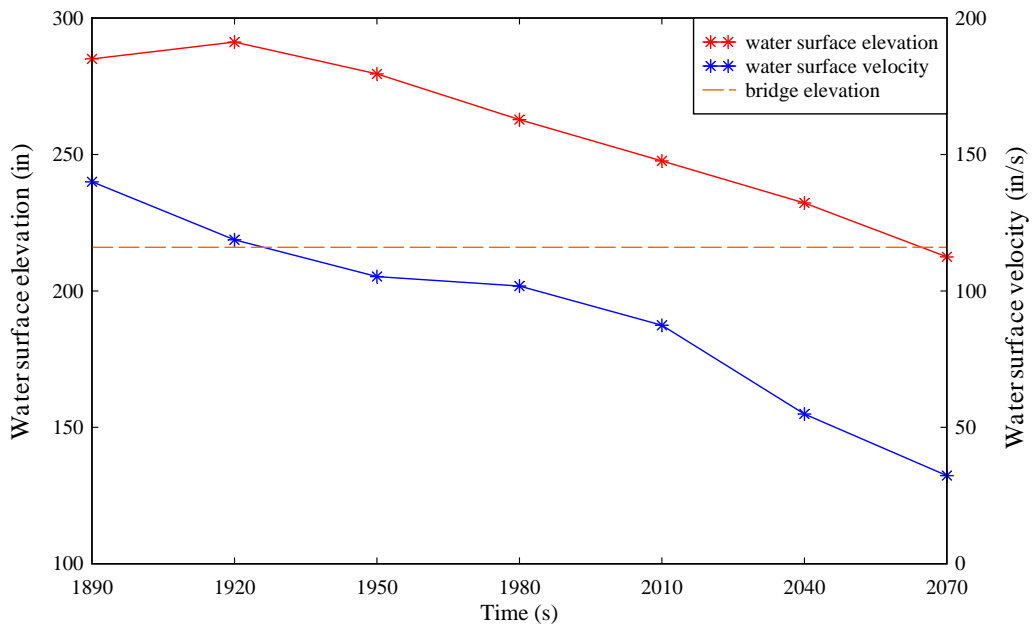


Figure A.9: Input conditions for simulation models of Schooner Creek Bridge under TZ M_w 9.0 tsunami scenario

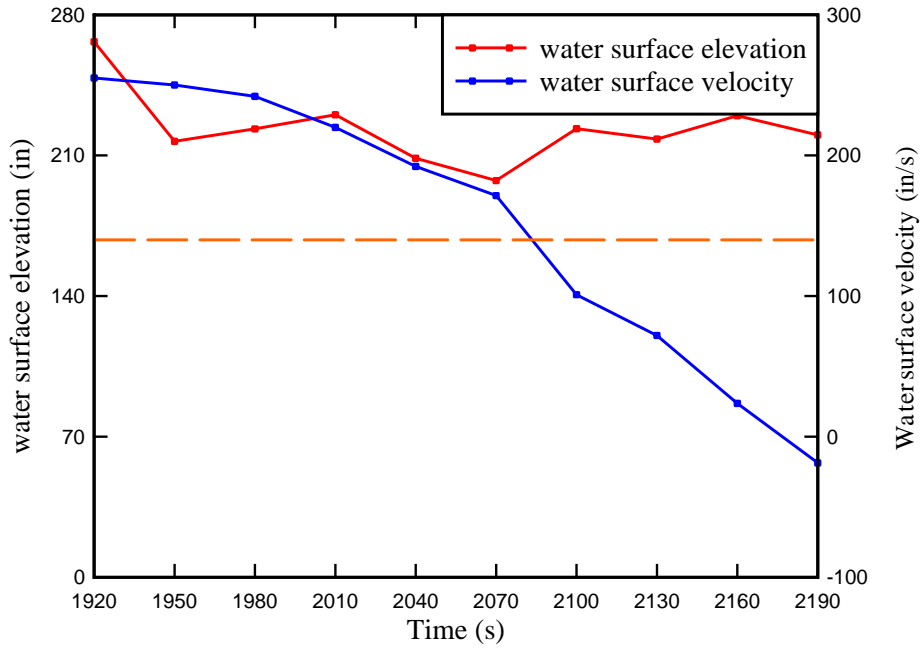


Figure A.10: Input conditions for simulation models of Drift Creek Bridge under GA M_w 9.2 tsunami scenario

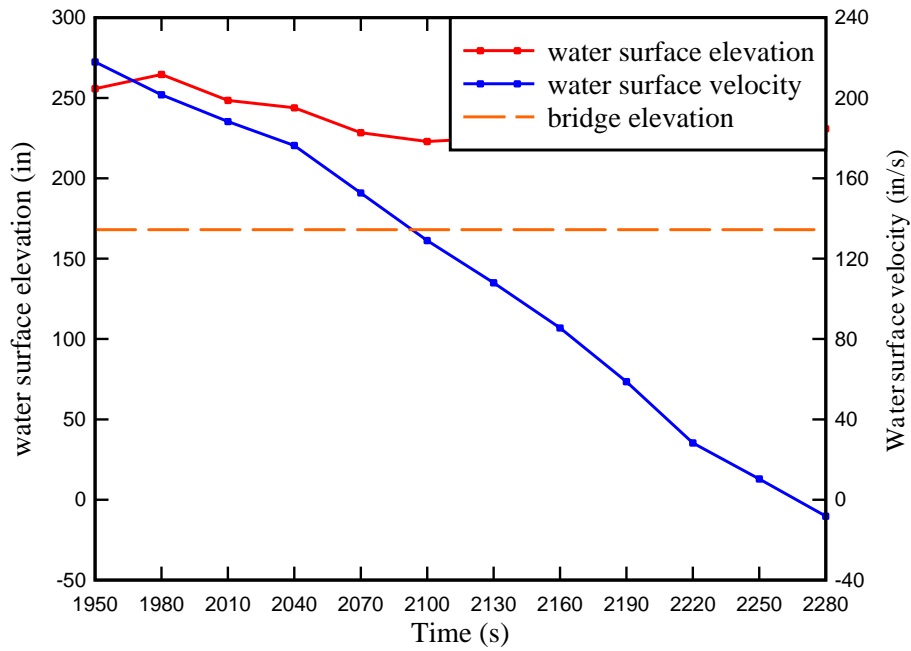


Figure A.11: Input conditions for simulation models of Drift Creek Bridge under LZ M_w 9.0 tsunami scenario

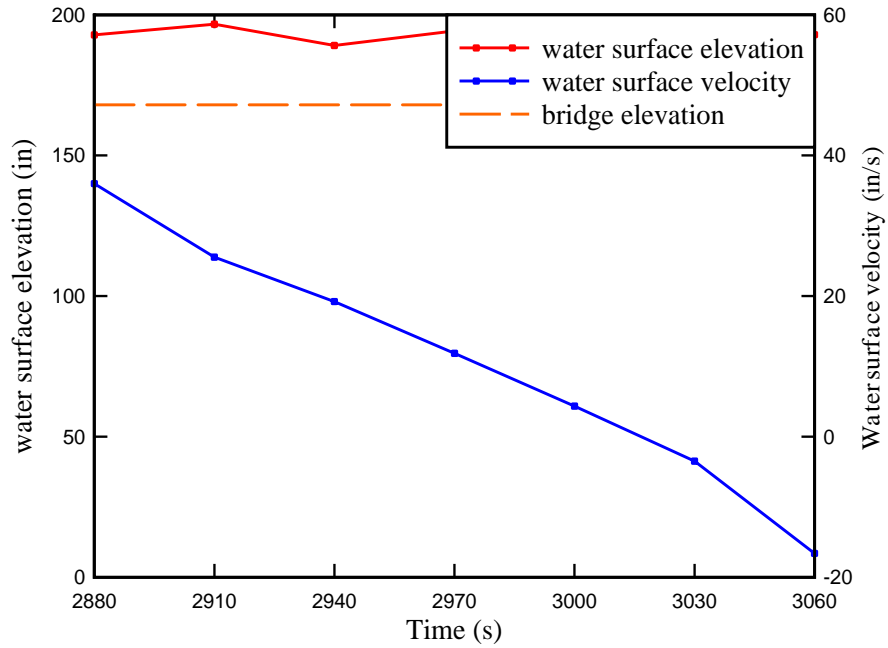


Figure A.12: Input conditions for simulation models of Drift Creek Bridge under MT M_w 9.0 tsunami scenario

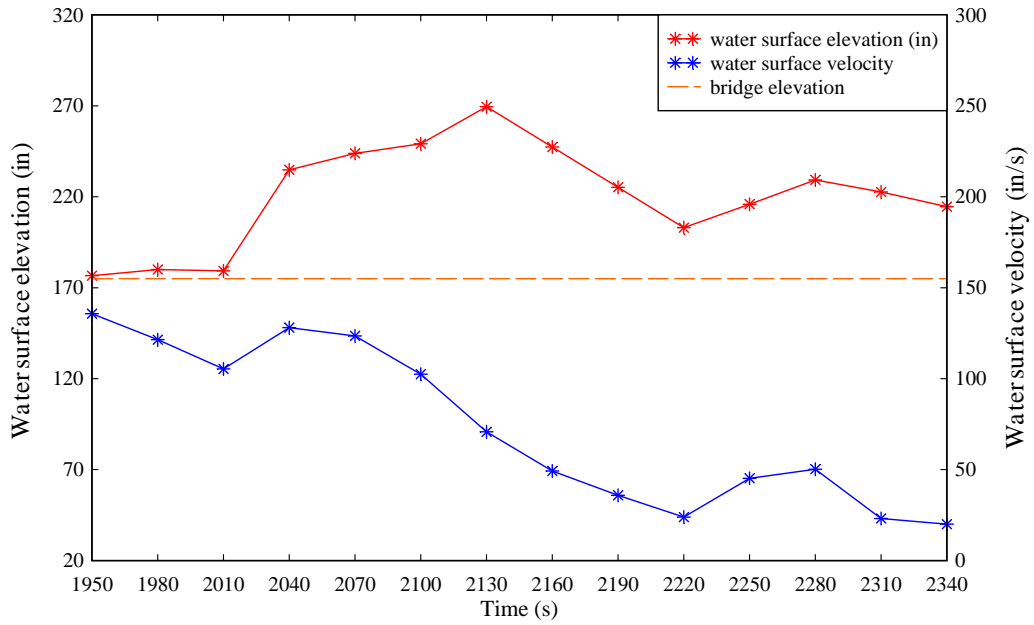


Figure A.13: Input conditions for simulation models of Millport Slough Bridge under GA M_w 9.2 tsunami scenario

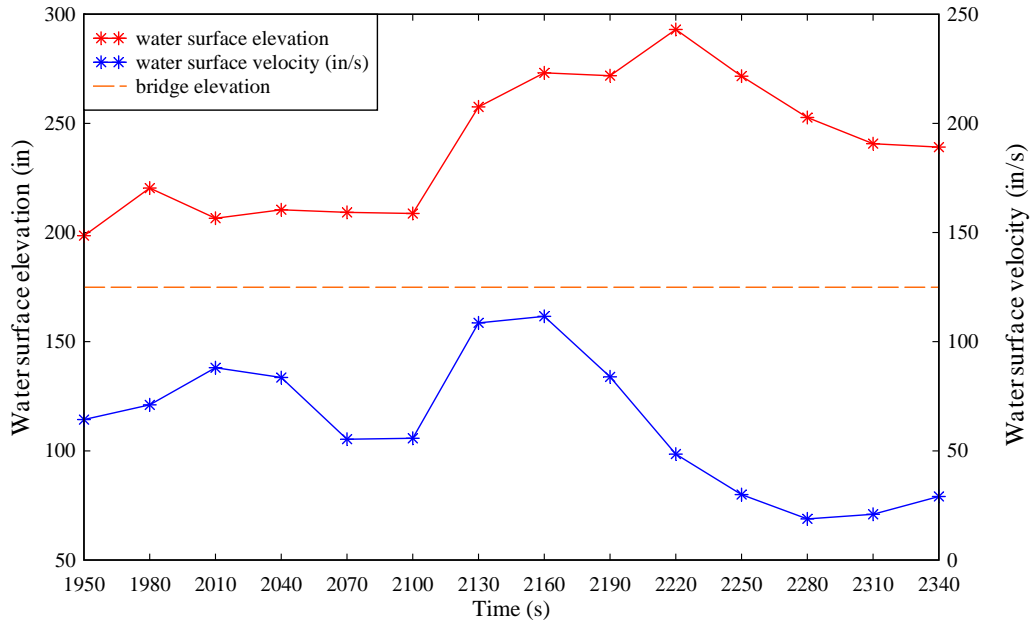


Figure A.14: Input conditions for simulation models of Millport Slough Bridge under LZ M_w 9.0 tsunami scenario

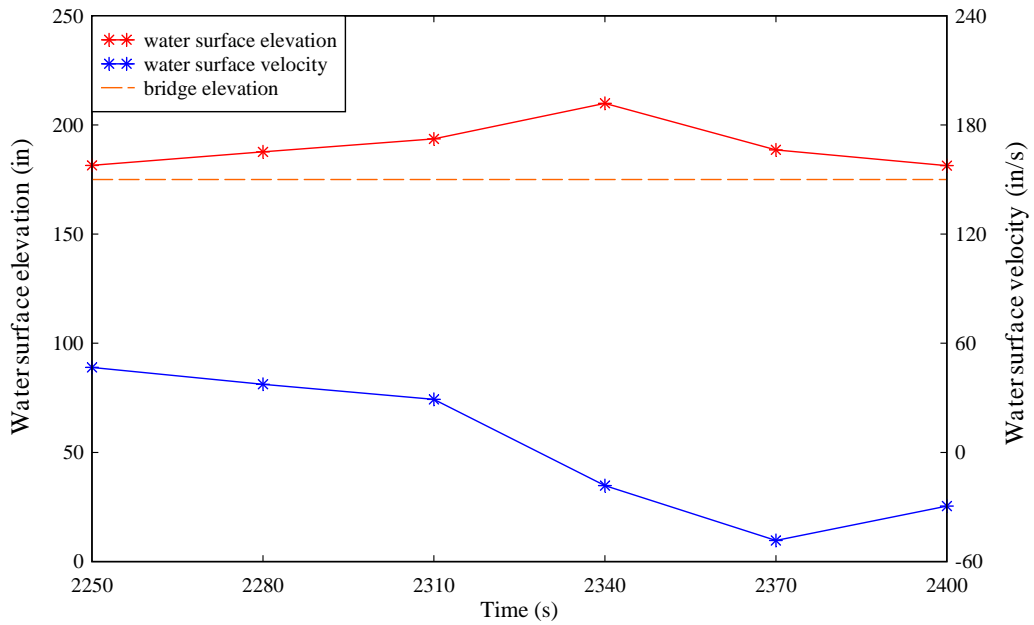


Figure A.15: Input conditions for simulation models of Millport Slough Bridge under MT M_w 9.0 tsunami scenario

A-3 SIMULATED TSUNAMI IMPACT ON SELECTED BRIDGE SUPERSTRUCTURES

Figures A.16 to A.19 show a set of screen captures of the Schooner Creek Bridge (box-section) under four tsunami scenarios. These figures, which captured the fluid flow field at different times during the analysis, are good visual tools to understand the behavior of tsunami hitting a bridge superstructure and the fluid-structure interaction phenomenon. These figures demonstrate the boundary condition of the incoming flow at the left side and movement of the fluid toward the bridge including inundation of the entire bridge superstructure. Figures A.20 to A.24 show the related screen captures of Schooner Creek Bridge (deck-girder) under five tsunami scenarios (the four cases as the Schooner Creek Bridge (box-section) plus the GAM_w9.2 scenario).

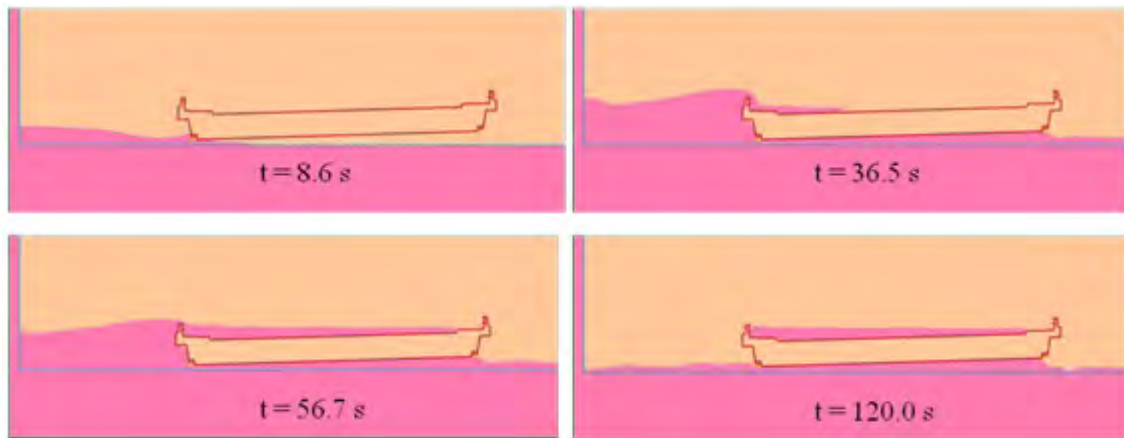


Figure A.16: Screen capture of Schooner Creek Bridge (box-section) under GA Mw 9.0 tsunami scenario

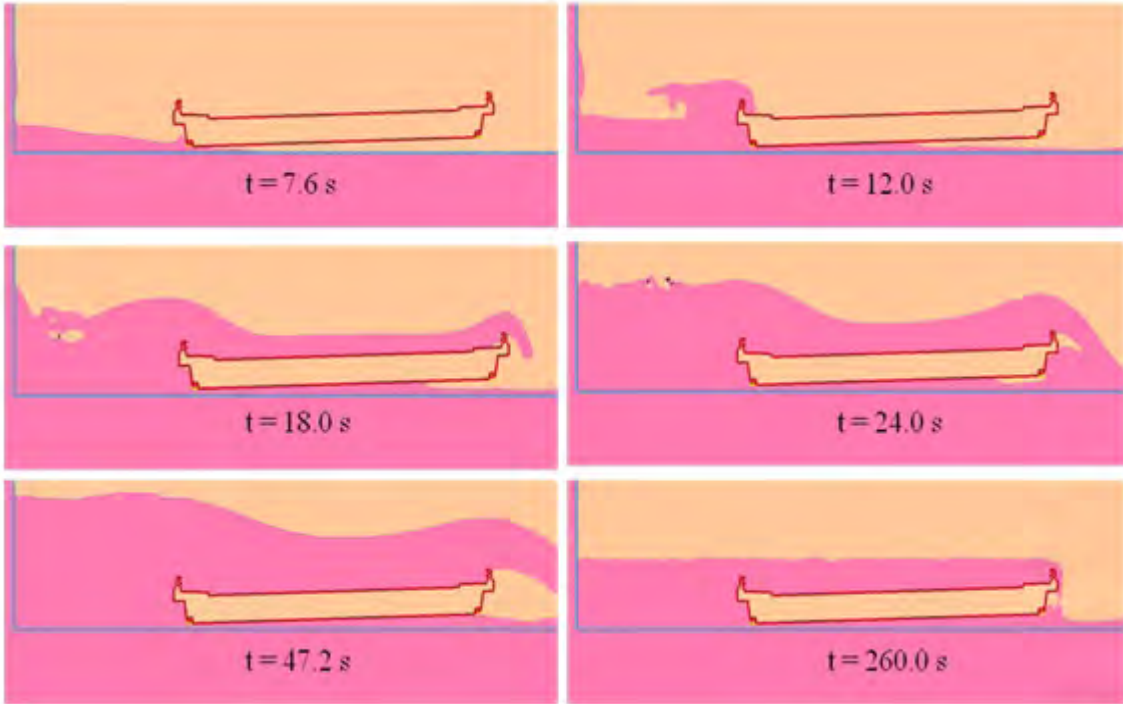


Figure A.17: Screen capture of Schooner Creek Bridge (box-section) under LZ Mw 9.0 tsunami scenario

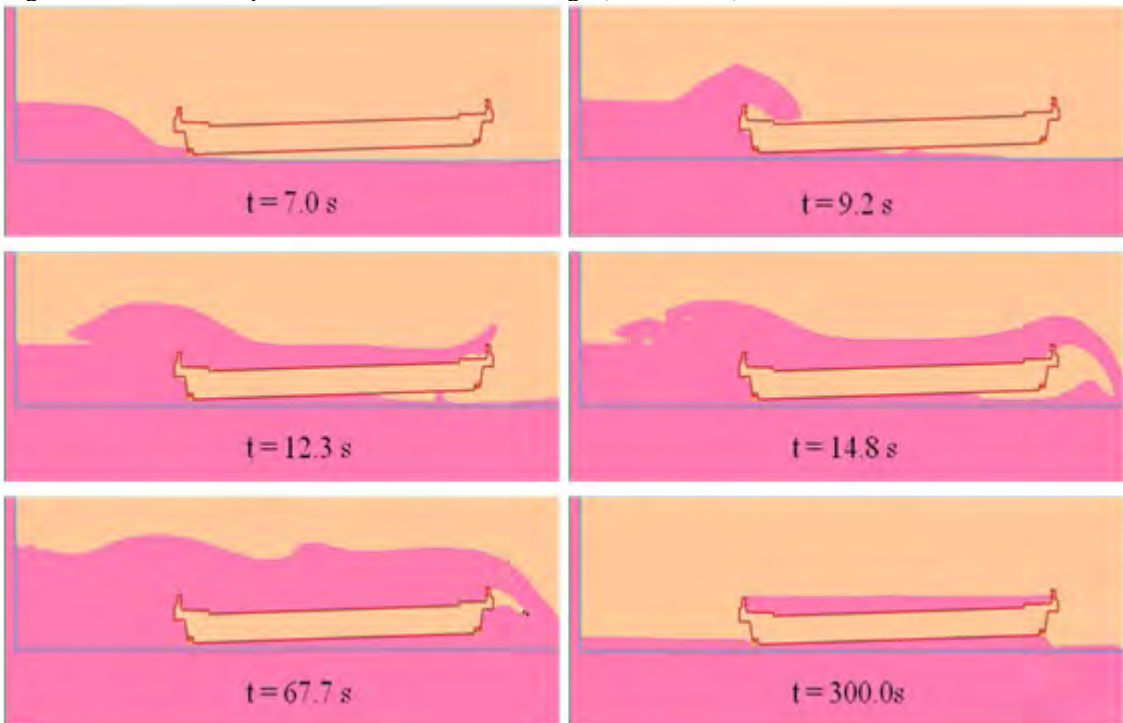


Figure A.18: Screen capture of Schooner Creek Bridge (box-section) under MT Mw 9.0 tsunami scenario

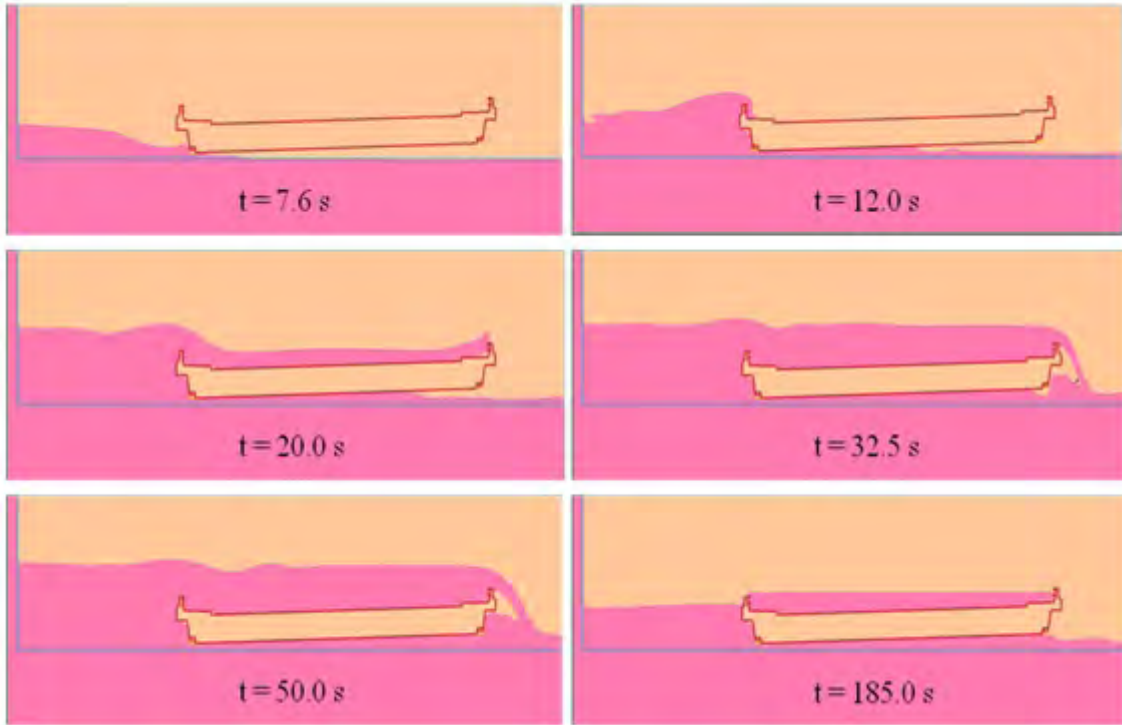


Figure A.19: Screen capture of Schooner Creek Bridge (box-section) under TZ Mw 9.0 tsunami scenario

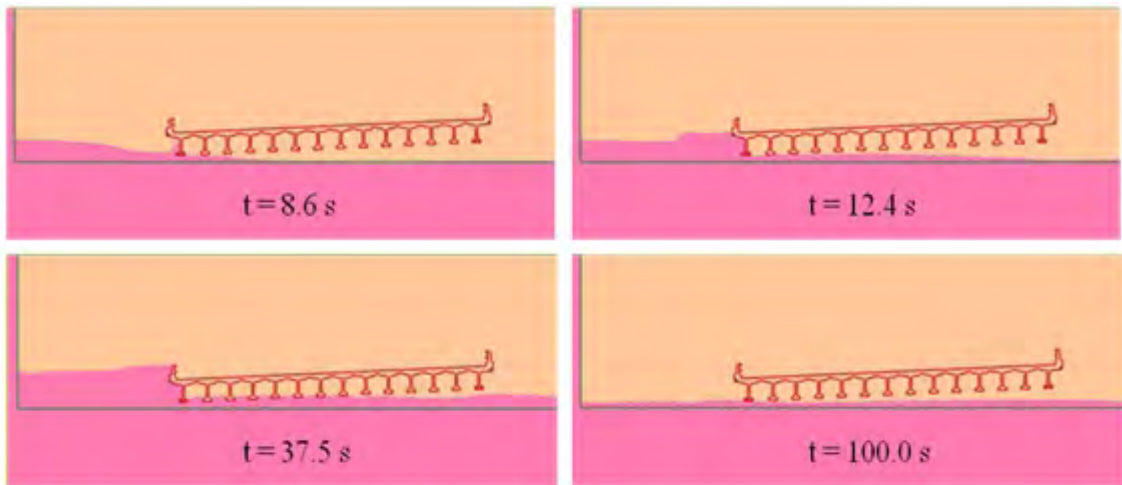


Figure A.20: Screen capture of Schooner Creek Bridge (deck-girder) under GA Mw 9.0 tsunami scenario

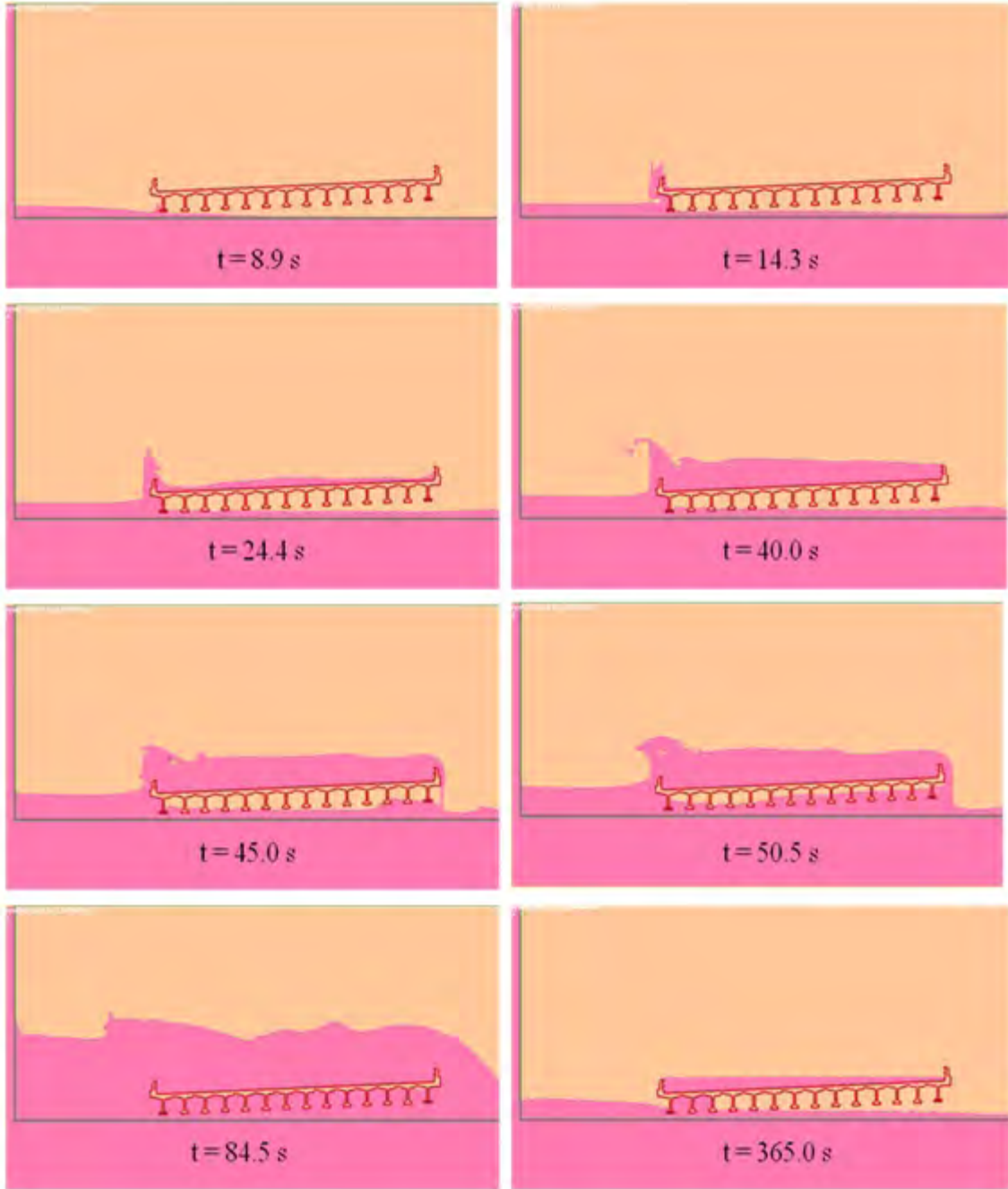


Figure A.21: Screen capture of Schooner Creek Bridge (deck-girder) under GA Mw 9.2 tsunami scenario

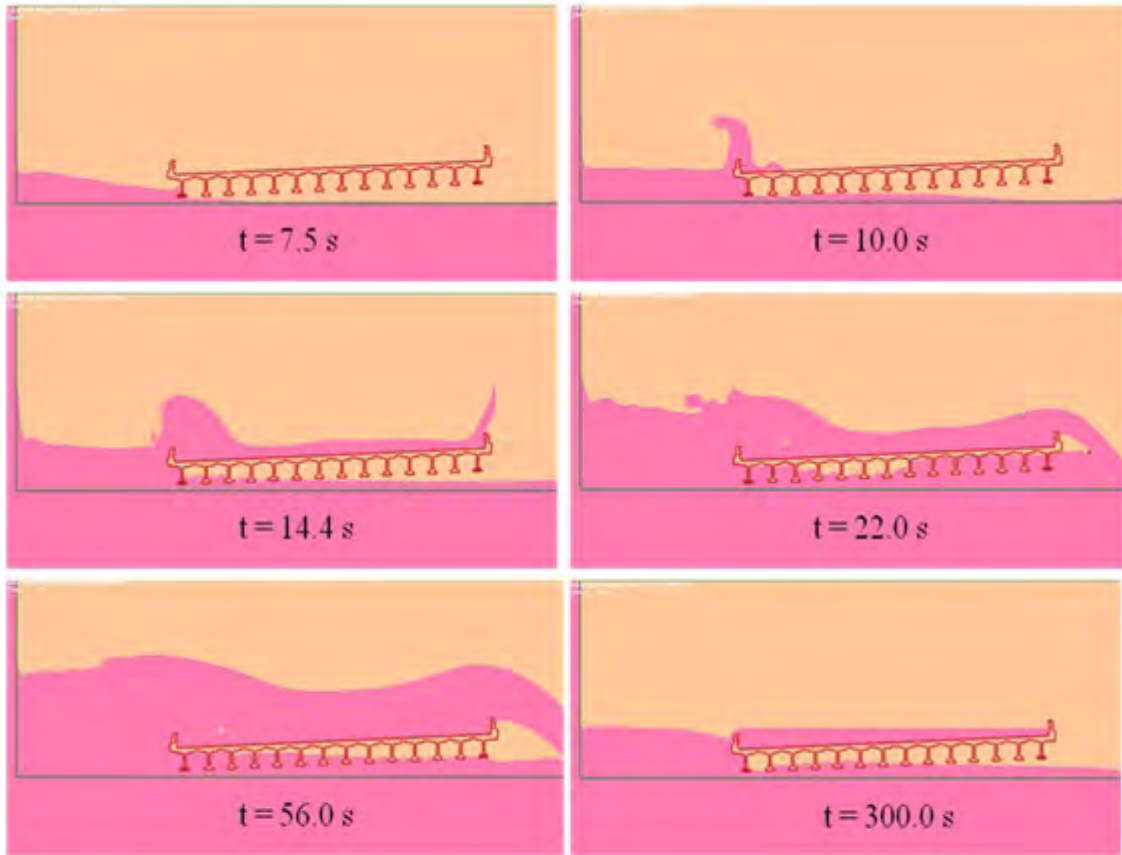


Figure A.22: Screen capture of Schooner Creek Bridge (deck-girder) under LZ Mw 9.0 tsunami scenario

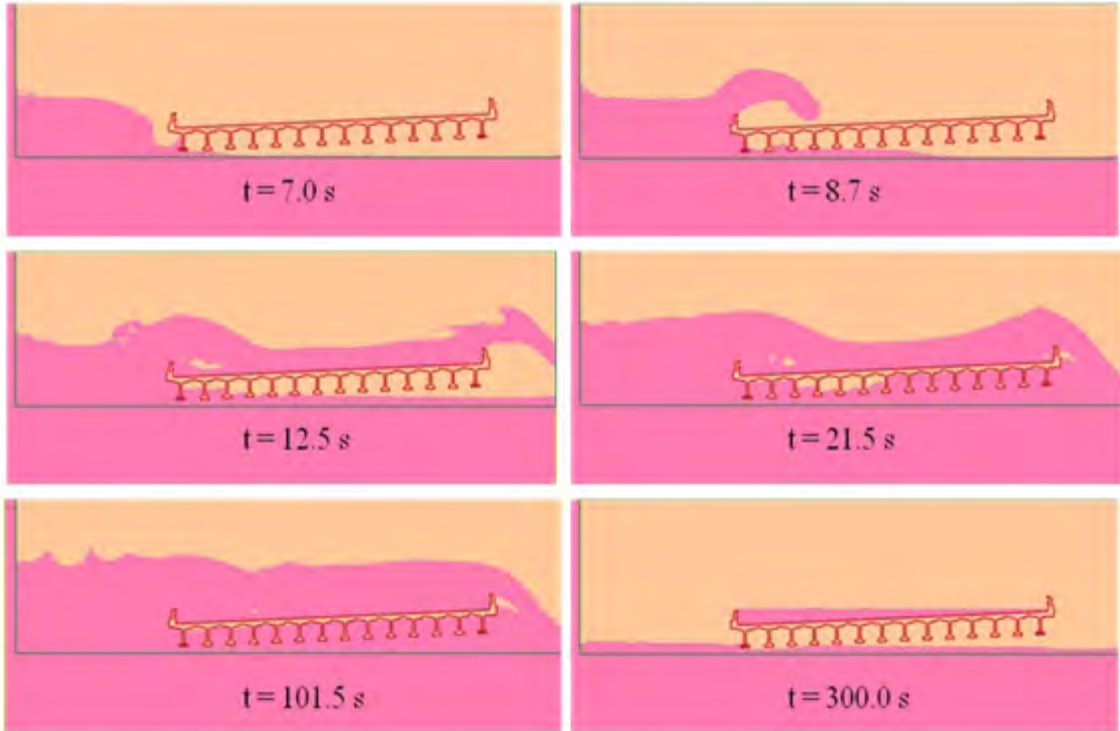


Figure A.23: Screen capture of Schooner Creek Bridge (deck-girder) under MT Mw 9.0 tsunami scenario

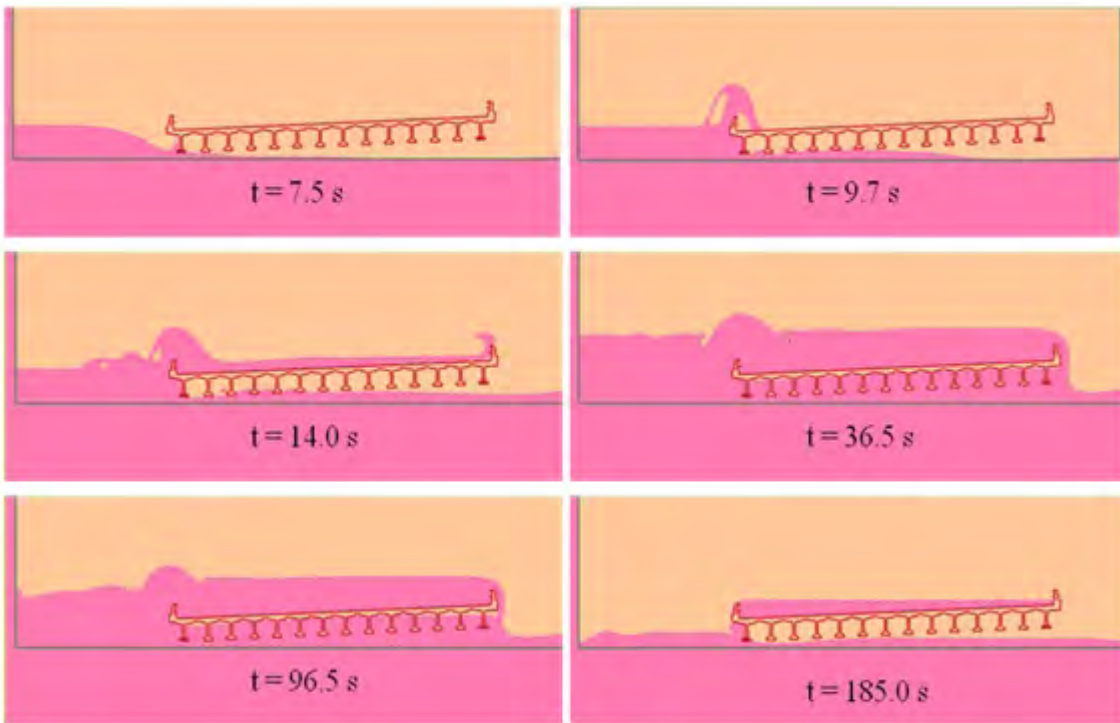


Figure A.24: Screen capture of Schooner Creek Bridge (deck-girder) under TZ Mw 9.0 tsunami scenario

Figures A.25 and A.26 show a set of screen captures of the Drift Creek Bridge under GA M_w 9.2 and LZ M_w 9.0 tsunami scenarios. A corresponding set of screen captures of the Millport Slough Bridge under GA M_w 9.2 and LZ M_w 9.0 tsunami scenarios are provided in Figures A.27 and A.28.

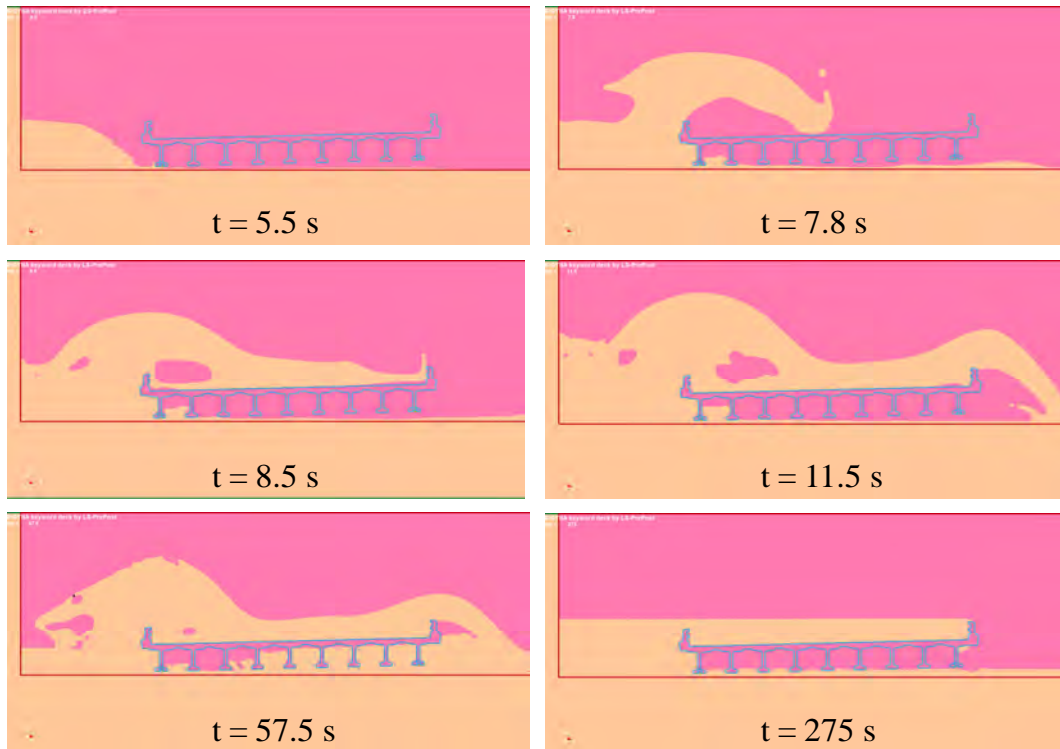


Figure A.25: Screen capture of Drift Creek Bridge under GA M_w 9.2 tsunami scenario

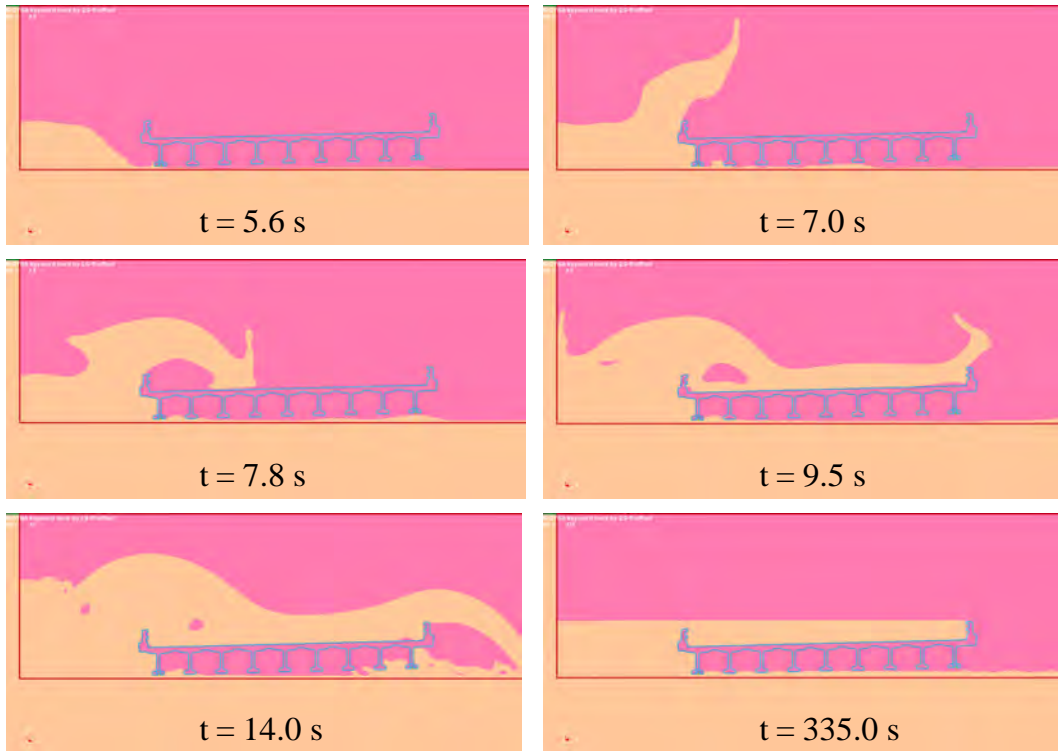


Figure A.26: Screen capture of Drift Creek Bridge under LZ Mw 9.0 tsunami scenario

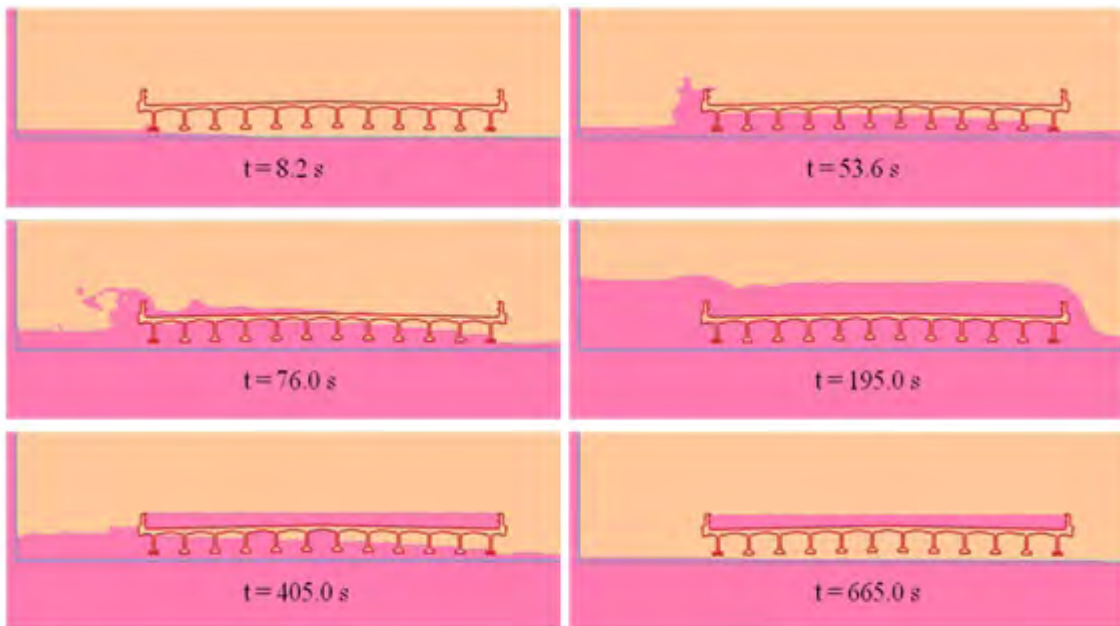


Figure A.27: Screen capture of Millport Slough Bridge under GA Mw 9.2 tsunami scenario

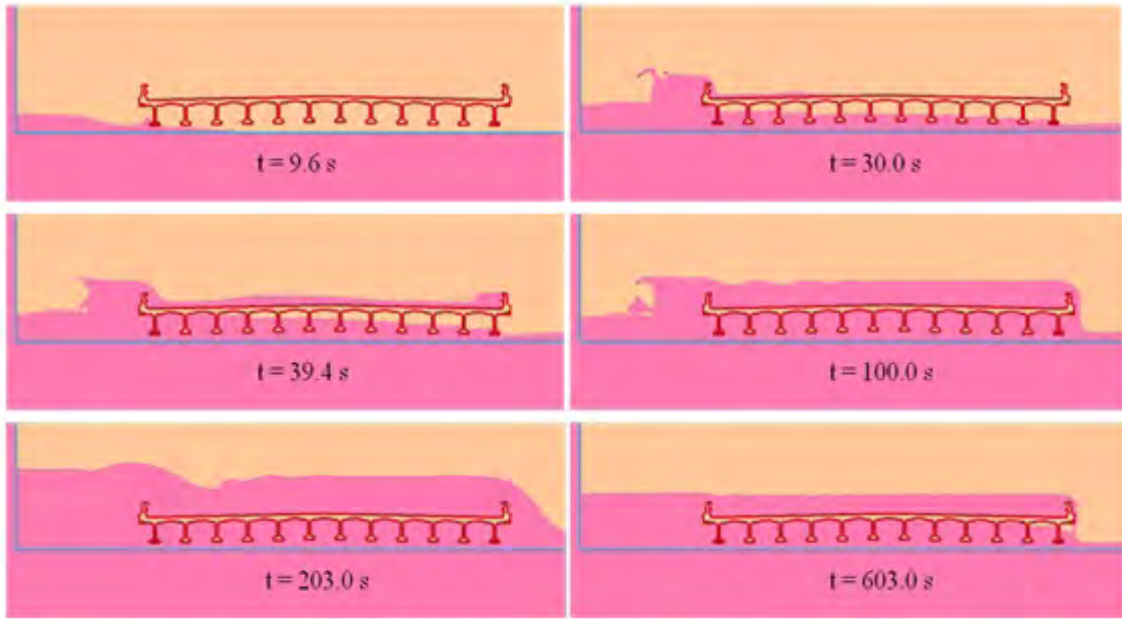


Figure A.28: Screen capture of Millport Slough Bridge under LZ Mw 9.0 tsunami scenario

**APPENDIX B:
TSUNAMI TIME-HISTORY FORCES OF THE SELECTED
BRIDGE SUPERSTRUCTURES**

This section presents horizontal and vertical forces time-histories of the selected bridges under the selected tsunami scenarios. The time-history results of the Schooner Creek Bridge under five selected tsunami scenarios – GA Mw 9.0, GA Mw 9.2, LZ Mw 9.0, MT Mw 9.0, and TZ Mw 9.0 – are shown in Figure B.1 to Figure B.13. The time-history results of the Drift Creek Bridge and the Millport Slough Bridge under three selected tsunami scenarios – GA Mw 9.2, LZ Mw 9.0, and MT Mw 9.0 – are shown in Figure B.14 and Figure B.15.

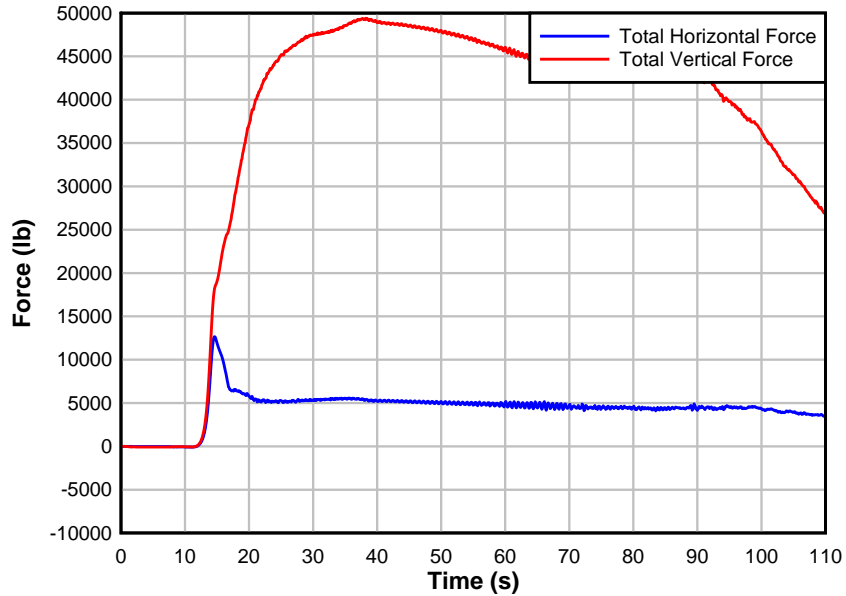


Figure B.1: Time-history forces of Schooner Creek Bridge (box-section) under GA Mw 9.0 tsunami conditions

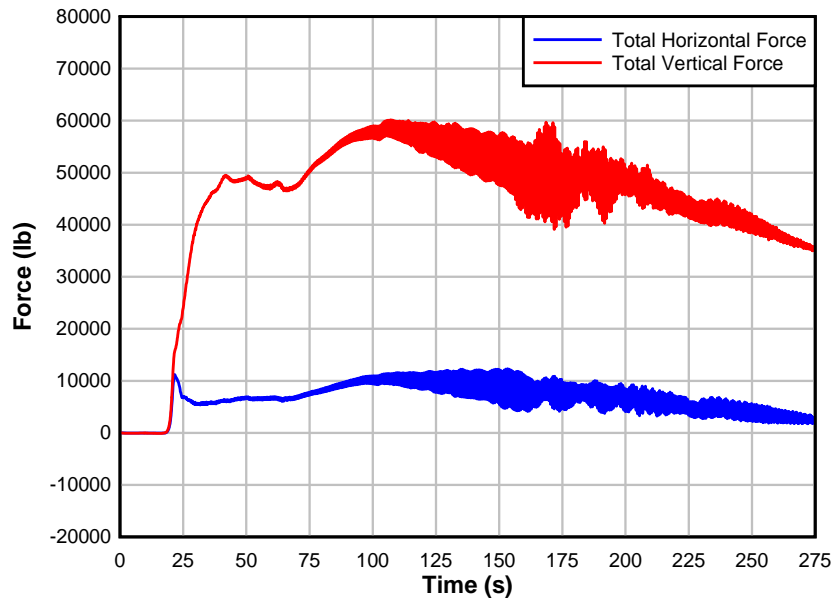


Figure B.2: Time-history forces of Schooner Creek Bridge (box-section) under GA Mw 9.2 tsunami conditions

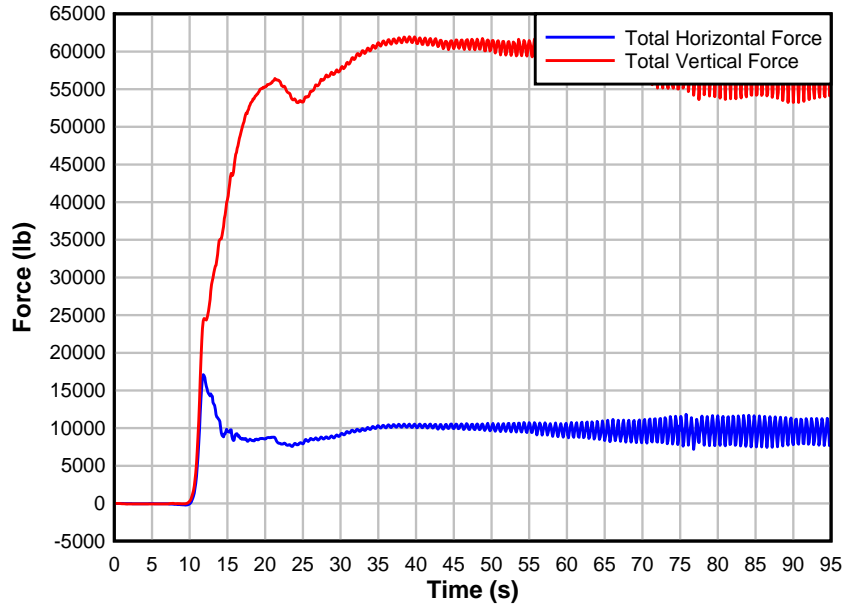


Figure B.3: Time-history responses of Schooner Creek Bridge (box-section) under LZ Mw 9.0 tsunami conditions

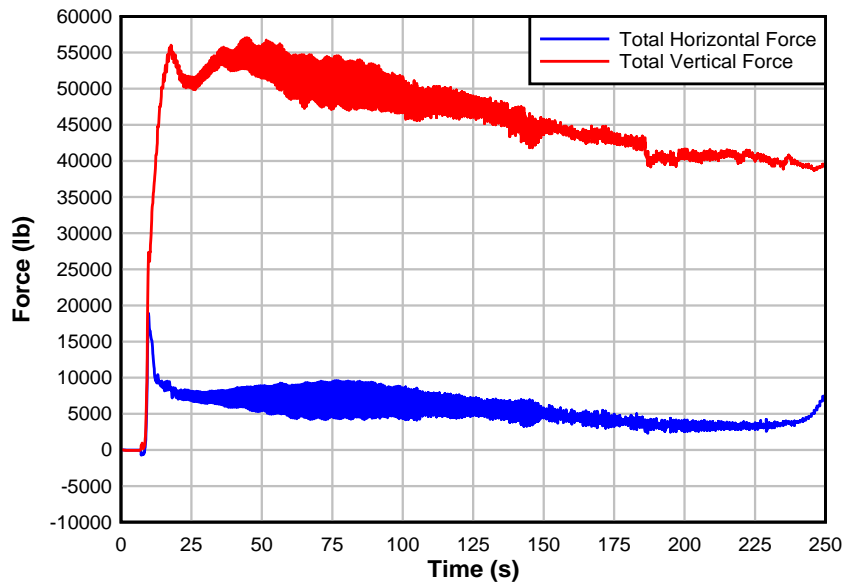


Figure B.4: Time-history forces of Schooner Creek Bridge (box-section) under MT Mw 9.0 tsunami conditions

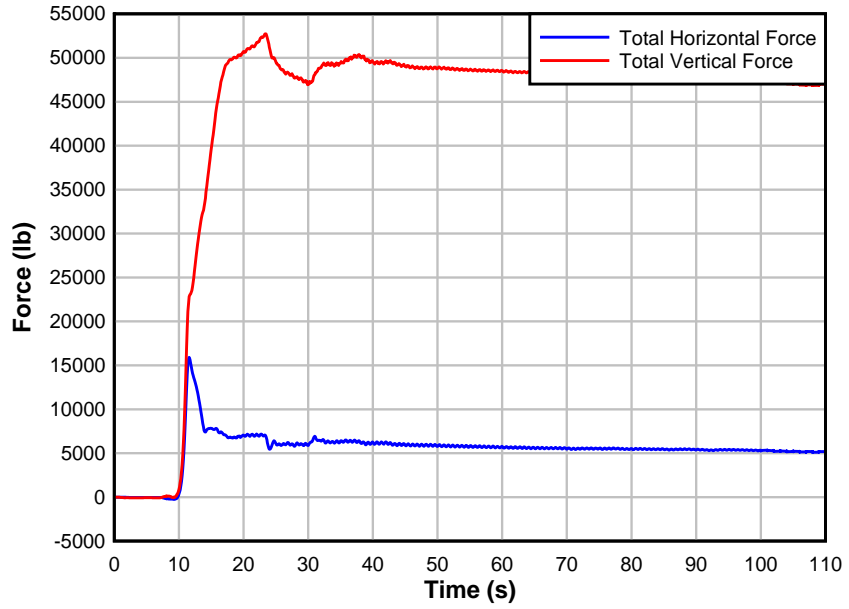


Figure B.5: Time-history forces of Schooner Creek Bridge (box-section) under TZ Mw 9.0 tsunami conditions

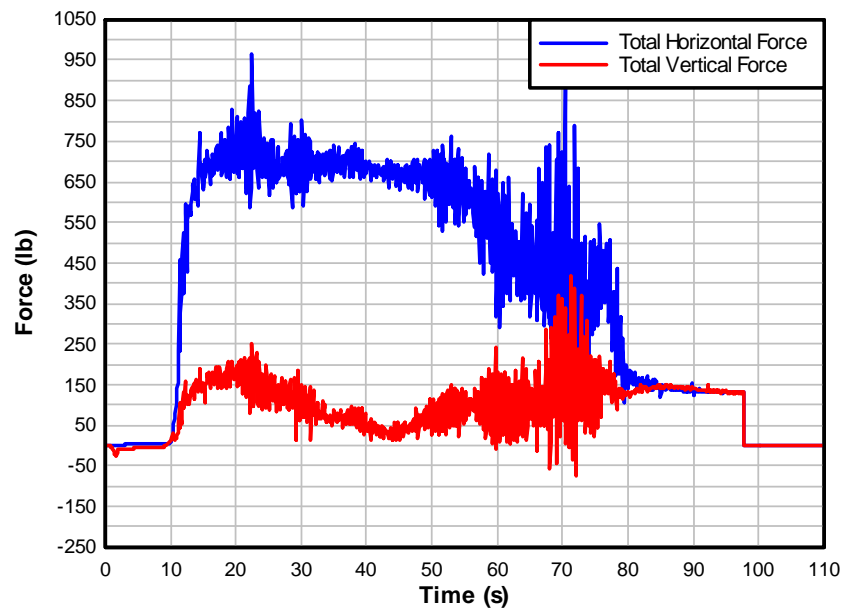


Figure B.6: Time-history forces of Schooner Creek Bridge (deck-girder) under GA Mw 9.0 tsunami conditions

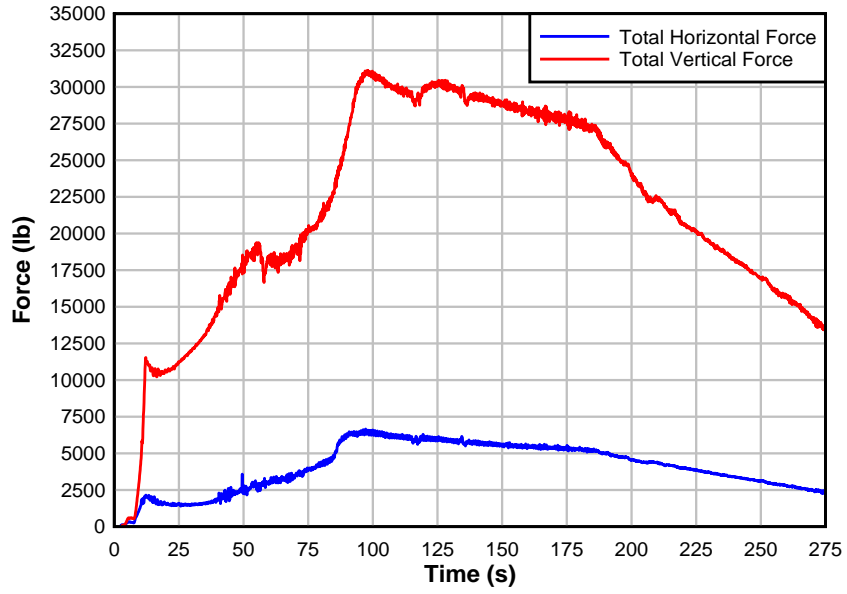


Figure B.7: Time-history forces of Schooner Creek Bridge (deck-girder) under GA Mw 9.2 tsunami conditions

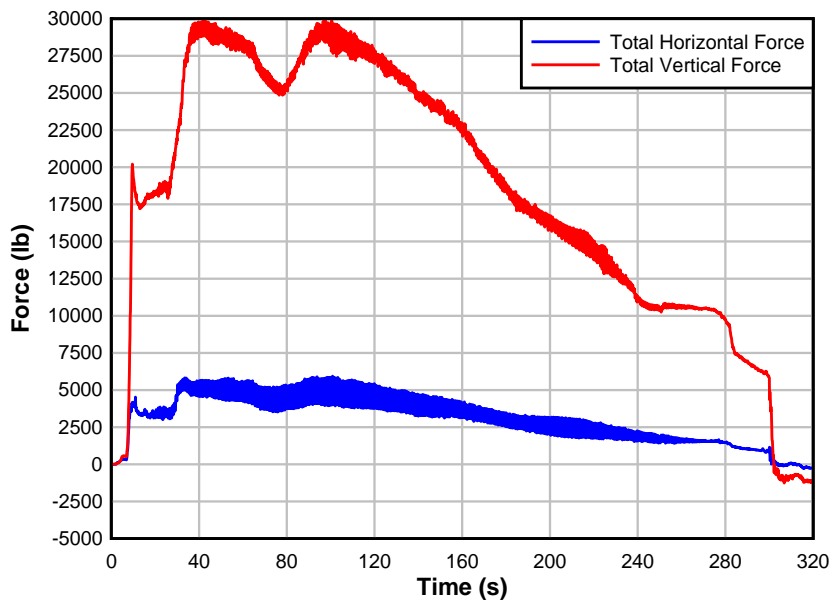


Figure B.8: Time-history forces of Schooner Creek Bridge (deck-girder) under LZ Mw 9.0 tsunami conditions

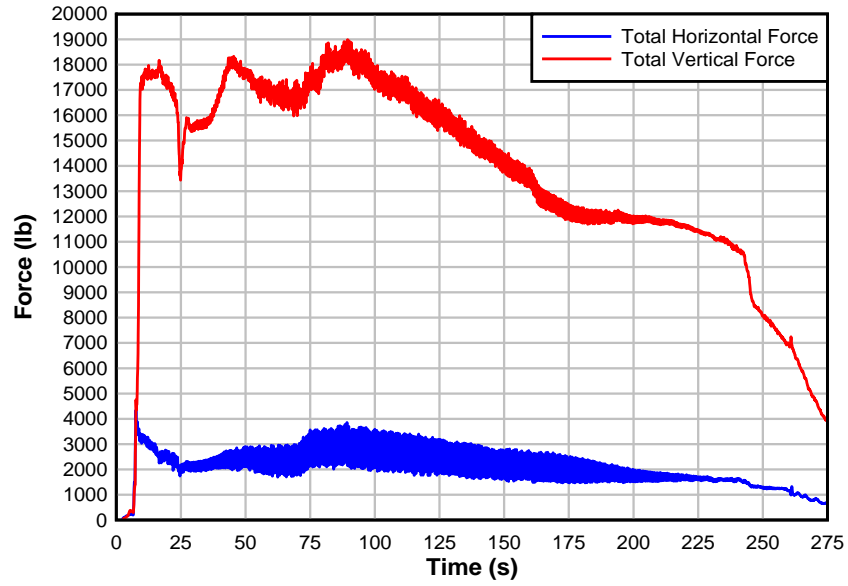


Figure B.9: Time-history forces of Schooner Creek Bridge (deck-girder) under MT Mw 9.0 tsunami conditions

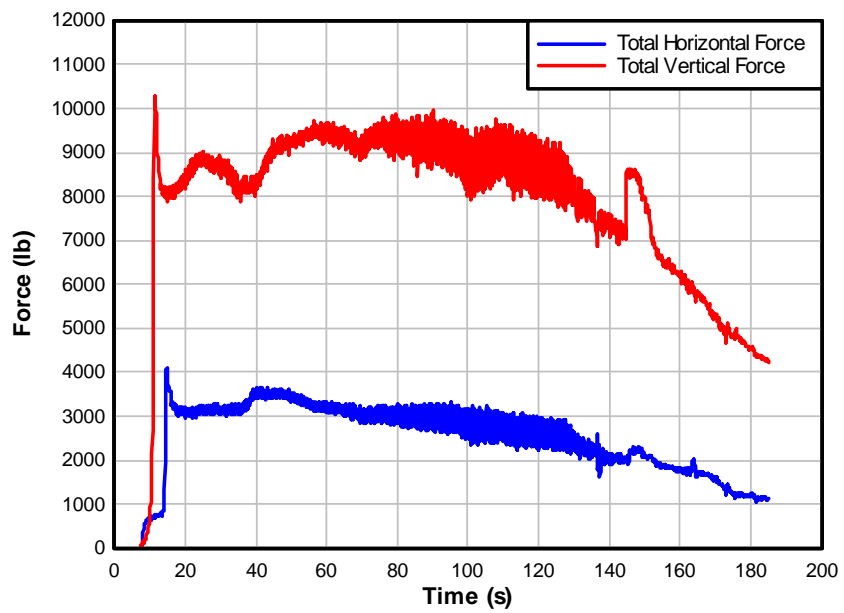


Figure B.10: Time-history forces of Schooner Creek Bridge (deck-girder) under TZ Mw 9.0 tsunami conditions

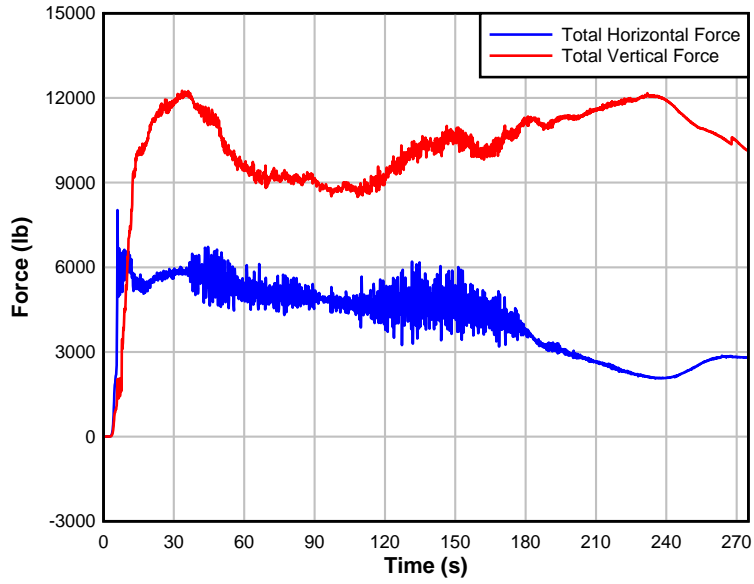


Figure B.11: Time-history forces of Drift Creek Bridge under GA Mw 9.2 tsunami conditions

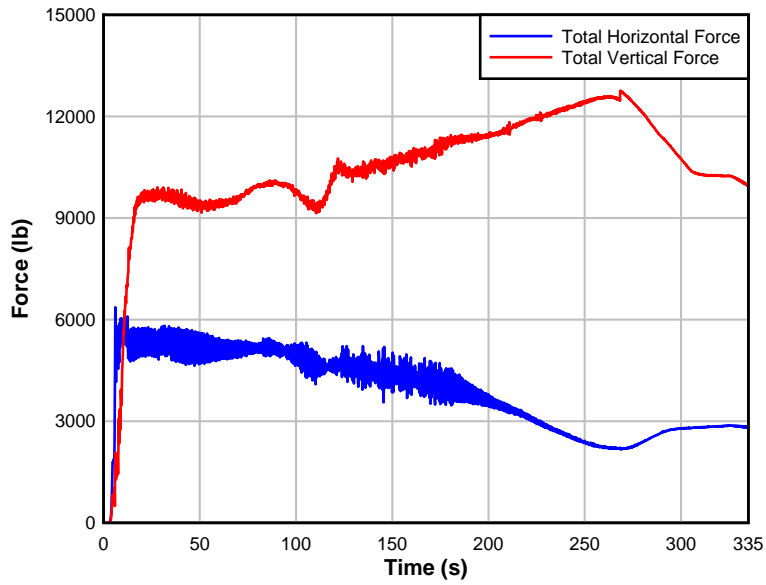


Figure B.12: Time-history forces of Drift Creek Bridge under LZ Mw 9.0 tsunami conditions

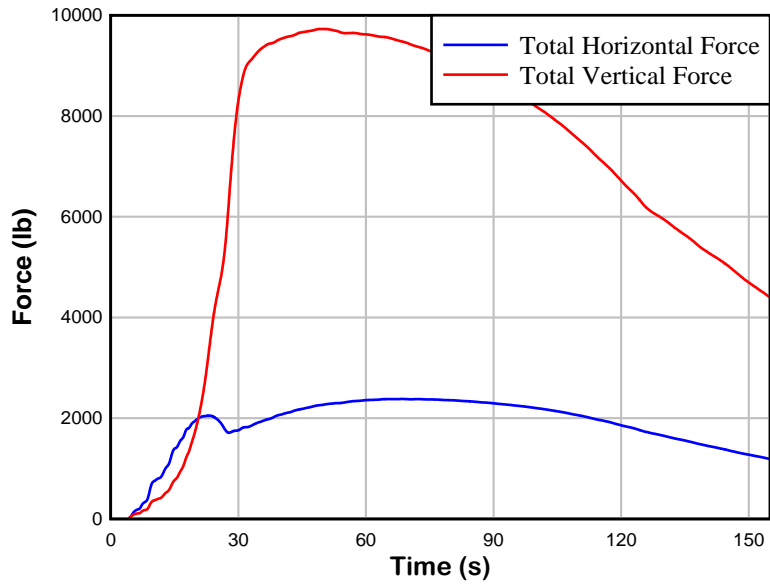


Figure B.13: Time-history forces of Drift Creek Bridge under MT Mw 9.0 tsunami conditions

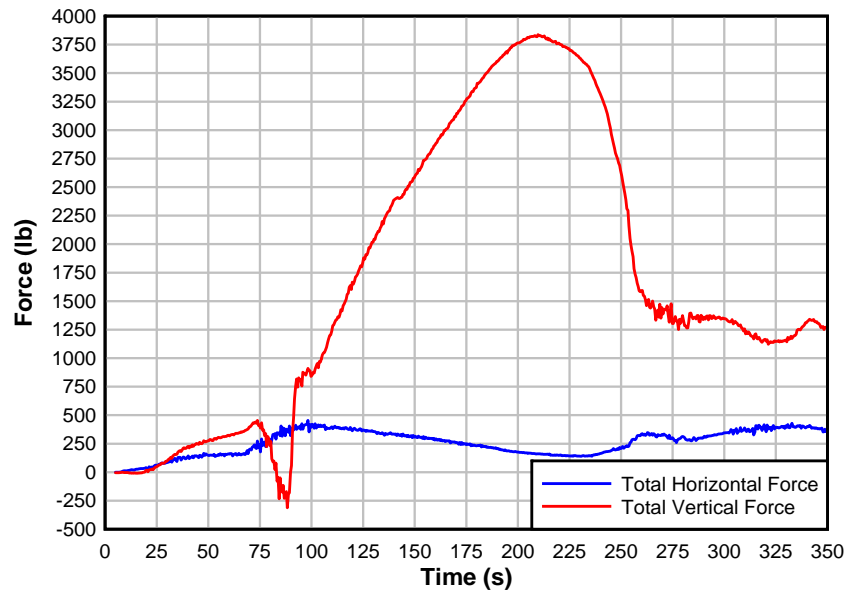


Figure B.14: Time-history forces of Millport Slough Bridge under GA Mw 9.2 tsunami conditions

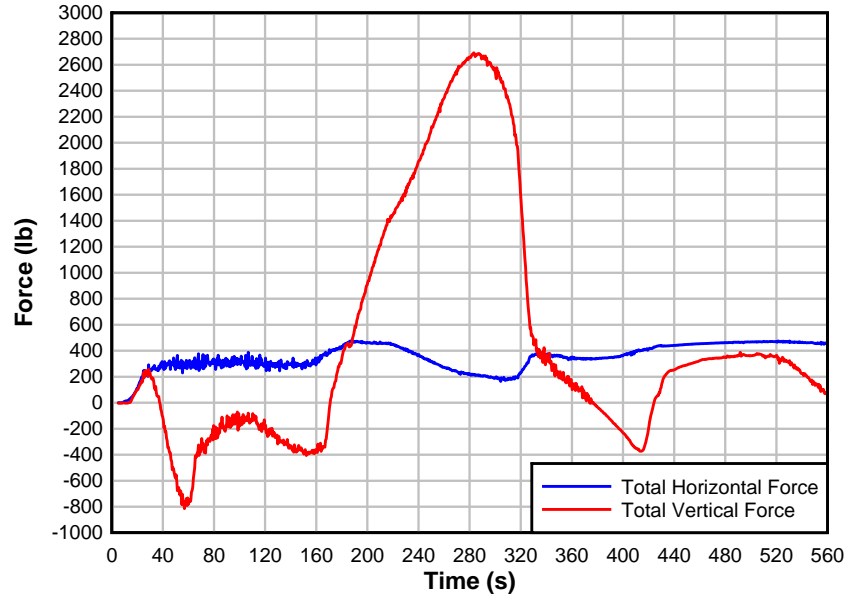


Figure B.15: Time-history forces of Millport Slough Bridge under LZ Mw 9.0 tsunami conditions

APPENDIX C
EXAMPLE CALCULATIONS OF TSUNAMI FORCES ON
BRIDGE SUPERSTRUCTURE

This section shows an example of tsunami forces calculations by using the existing method mentioned earlier in the paper. The example calculations are based on the deck-girder section at Schooner Creek Bridge under the tsunami loads generated by the GA rupture configuration at moment magnitude 9.2.

The bridge deck cross-section properties are given here as follows: underside of bridge deck elevation = 264 in.; underside of girder elevation = 216 in.; elevation of c.g. of the cross-section = 250 in.; number of girders = 14; subjected area normal to horizontal force (A_h) = 93.5 in²; subjected area normal to vertical force (A_v) = 903 in²; bridge deck volume = 8970 in³. The subjected areas and volume of bridge deck are based on one inch thickness of bridge cross-sectional. The required tsunami condition data are also provided here as follows: unit weight of water = 62 lb/ft³; maximum water surface elevation = 498.4 in.; maximum horizontal velocity of water = 169.45 in/s²; maximum vertical velocity of water = 6.71 in/s²; maximum water acceleration = 1.33 in/s²; maximum flux momentum (hu^2_{max}) = 7418.2 x 10³ in³/s².

Note that the maximum water surface elevation (h_{max}) is measured based on the total water free surface elevation from the ground and the value of the (Δz) used for calculating the horizontal and vertical forces is determined by subtracting the elevation of the underside of bridge girder from the total water free surface elevation. In other words, Δz is the distance from the bottom of the girders to the instantaneous water free-surface elevation.

Given :

Bridge Properties

$$h_{br} := 216 \text{ in} \quad N := 14 \quad b := 1 \text{ in}$$

$$A_v := 903 \text{ in}^2 \quad A_h := 93.5 \text{ in}^2 \quad V := 8970 \text{ in}^3$$

Tsunami Conditions

$$h_{max} := 498.4 \text{ in} \quad u_x := 169.45 \frac{\text{in}}{\text{s}} \quad u_v := 6.71 \frac{\text{in}}{\text{s}}$$

$$a_{max} := 1.33 \frac{\text{in}}{\text{s}^2} \quad \text{flux}_{max} := 7418.210^3 \frac{\text{in}^3}{\text{s}^2}$$

General Conditions

$$g := 386 \frac{\text{in}}{\text{s}^2} \quad \gamma_w := 62 \frac{\text{lb}}{\text{ft}^3} \quad \gamma_s := 1.2 \gamma_w = 74.4 \frac{\text{lb}}{\text{ft}^3}$$

$$\rho_s := 1.2 \frac{\gamma_w}{g} = 2.313 \frac{\text{lb} \cdot \text{s}^2}{\text{ft}^4}$$

1. Douglass et al. (2006)'s method for estimating wave forces on bridge decks

$$C_r := 0.4 \quad C_{h.va} := 1 \quad C_{h.im} := 6$$

$$C_{v.va} := 1 \quad C_{v.im} := 3$$

$$\Delta z := h_{\max} - h_{br} = 23.533\text{ft}$$

$$F_{H.Douglass} := \left[\left[1 + C_r \cdot (N - 1) \right] \cdot C_{h.va} + C_{h.im} \right] \cdot \gamma_s \cdot \Delta z \cdot A_h = 1.387 \times 10^4 \text{ lb}$$

$$F_{V.Douglass} := (C_{v.va} + C_{v.im}) \cdot \gamma_s \cdot \Delta z \cdot A_v = 4.392 \times 10^4 \text{ lb}$$

2. FEMA P646 (2008), Guidelines for Design of Structures for Vertical Evacuation from Tsunamis

$$C_d := 2 \quad C_u := 3$$

Hydrostatic Force : $F_{hs} := \gamma_s \cdot \Delta z \cdot A_h = 1.137 \times 10^3 \text{ lb}$

Hydrodynamic Force: $F_d := 0.5 \cdot \rho_s \cdot C_d \cdot b \cdot \text{flux}_{\max} = 827.447\text{lb}$

Impulsive Force: $F_i := 1.5 \cdot F_d = 1.241 \times 10^3 \text{ lb}$

$$F_{H.FEMA} := F_{hs} + F_d + F_i = 3.205 \times 10^3 \text{ lb}$$

Buoyant Force: $F_b := \gamma_s \cdot V = 386.208\text{lb}$

Uplift Force: $F_u := 0.5 \cdot C_u \cdot \rho_s \cdot A_v \cdot u_v^2 = 6.802\text{lb}$

$$F_{V.FEMA} := F_b + F_u = 393.01 \text{ lb}$$

3. Performance-Based Tsunami Engineering (PBTE): Tsunami bore on vertical wall and slab

Bridge Longitudinal Span Length: $L := 297.083\text{ft}$

Width to inundation depth ratio: $R := \frac{L}{\Delta z} = 12.624$

$$C_{d.PBTE} := \begin{cases} 1.25 & \text{if } 1 < R < 12 \\ 1.3 & \text{if } 12 < R < 20 \end{cases} = 1.3$$

Hydrodynamic Force: $F_{d.PBTE} := 0.5 \cdot \rho_s \cdot C_{d.PBTE} \cdot b \cdot \Delta z \cdot u_x^2 = 587.899\text{lb}$

Hydrostatic Force: $F_{hs.PBTE} := 0.5 \cdot \rho_s \cdot g \cdot b \cdot \Delta z^2 = 1.717 \times 10^3\text{ lb}$

$$F_{H.PBTE} := F_{d.PBTE} + F_{hs.PBTE} = 2.305 \times 10^3\text{ lb}$$

$$\beta := \frac{\Delta z}{h_{\max}} = 0.567$$

$$C_{u.PBTE} := \begin{cases} \beta \cdot \frac{3}{0.5} & \text{if } \beta < 0.5 \\ 3 & \text{if } 0.5 < \beta < 1.5 \end{cases} = 3$$

Buoyant Force: $F_b.PBTE := \gamma_s \cdot V = 386.208\text{lb}$

Uplift Force: $F_u.PBTE := 0.5 \cdot C_{u.PBTE} \cdot \rho_s \cdot u_x^2 \cdot A_v = 4.338 \times 10^3\text{ lb}$

$$F_V.PBTE := F_b.PBTE + F_u.PBTE = 4.724 \times 10^3\text{ lb}$$

4. The Recommended Approach for estimating tsunami forces on bridge superstructures

$$C_{d,\text{recommend}} := 1$$

$$\text{Hydrostatic Force: } F_{\text{hs.recommend}} := [1 + C_r \cdot (N - 1)] \cdot \gamma_s \cdot \Delta z \cdot A_h = 7.049 \times 10^3 \text{ lb}$$

$$\text{Hydrodynamic Force: } F_{\text{d.recommend}} := 0.5 \cdot C_{d,\text{recommend}} \cdot \rho_s \cdot b \cdot \text{flux}_{\text{max}} = 413.724 \text{ lb}$$

$$F_{\text{H.recommended}} := F_{\text{hs.recommend}} + F_{\text{d.recommend}} = 7.462 \times 10^3 \text{ lb}$$

$$u_{\text{x.out}} := 3.5 \cdot u_x = 49.423 \frac{\text{ft}}{\text{s}}$$

$$\text{Buoyant Force: } F_{\text{b.recommend}} := \gamma_s \cdot \Delta z \cdot A_v = 1.098 \times 10^4 \text{ lb}$$

$$\text{Uplift Force: } F_{\text{u.recommend}} := 0.5 \cdot \rho_s \cdot u_{\text{x.out}}^2 \cdot A_v = 1.771 \times 10^4 \text{ lb}$$

$$F_{\text{V.recommend}} := F_{\text{b.recommend}} + F_{\text{u.recommend}} = 2.869 \times 10^4 \text{ lb}$$

Note that, all forces calculated above are based on unit length of the bridge and show the estimated force due to tsunami loading on one inch length of the bridge.

APPENDIX D
A CASE STUDY OF SPENCER CREEK BRIDGE, OREGON
– REVISITED

As mentioned earlier, this research is an extension of the case study of the Spencer Creek Bridge conducted by Nimmala et al. (2006). Compared to the four bridges on Siletz Bay, the Spencer Creek Bridge is located at a different area on the Oregon Coast subjected to different tsunami load pattern. Since the bridge location is open to the Pacific, the tsunamis quickly travel across the bridge without trapping water as presented in the Siletz Bay area. Other than the bridge location and tsunami pattern, the cross-section of the Spencer Creek Bridge is quite unique. The bridge superstructure consists of a deck with crossbeam supporting the deck and arch structure supporting the crossbeam as shown in Figure D.1 and Figure D.2.



Figure D.1: Model of Spencer Creek Bridge [ref: <ftp://ftp.wsdot.wa.gov/public/Bridge/WBES2007>]



Figure D.2: Spencer Creek Bridge [ref: <http://bridgehunter.com/photos/>]

The tsunami sources for numerical models of the Spencer Creek Bridge were provided by Professor Cheung and associate from University of Hawaii. The provided tsunami data were obtained from two different numerical models, Cornell model and FVWAVE model. Nimmala et al. (2006) performed finite-element based numerical models of tsunami impact on the Spencer Creek Bridge under provided tsunami conditions from both Cornell and FVWAVE models. The numerical results by Nimmala et al. (2006) are shown in Figure D.3 and Figure D.4. These results were revisited in this research to help in studying the application of the recommended formulation, provided in section 5 in the manuscript, to a bridge superstructure with different geometry.

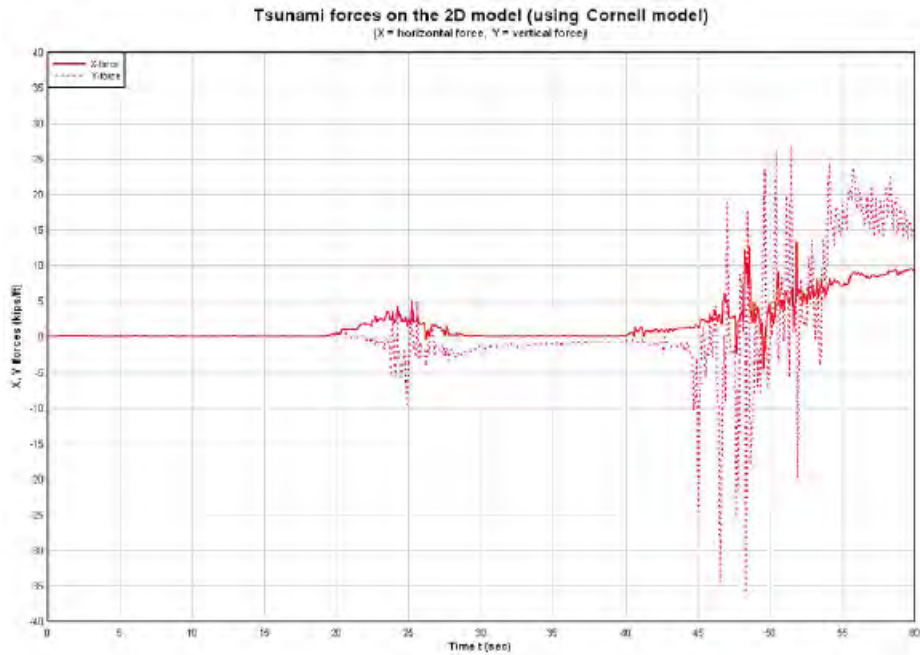


Figure D.3: Horizontal and vertical force time-histories based on Cornell tsunami model

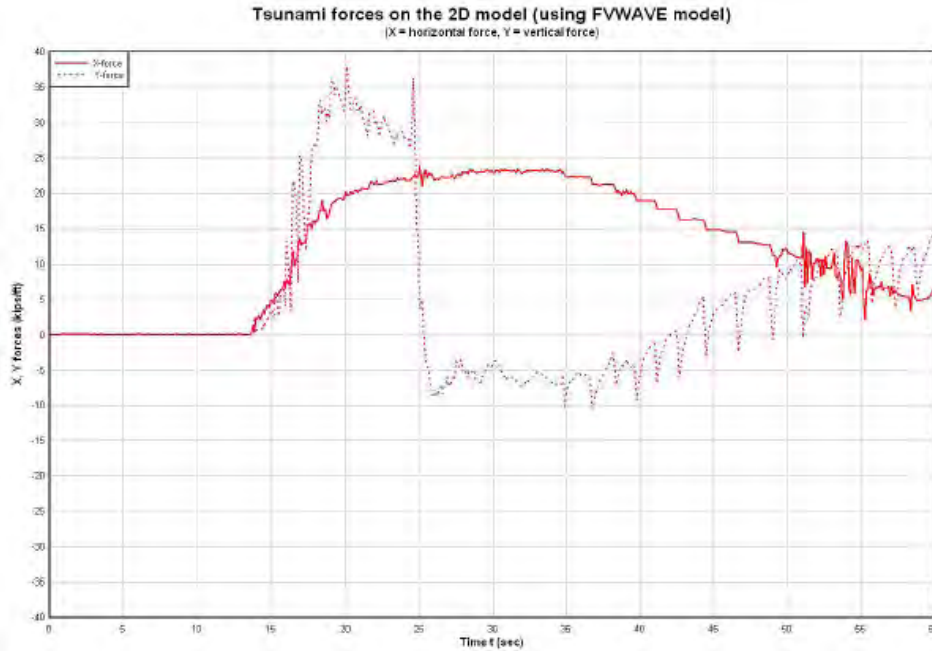


Figure D.4: Horizontal and vertical force time-histories based on FVWAVE tsunami model

An example calculation of tsunami forces on the deck of the Spencer Creek Bridge is described in this section. In this case, the bridge superstructure consists of the deck and crossbeam without a girder. Therefore, the term that accounting for distributing forces on the internal girders must be canceled; or, the bridge superstructure can be thought of as a bridge deck with a single girder ($N = 1$).

Given :

Bridge Properties

$$h_{br} := 50\text{ft} \quad N := 1 \quad b := 3\text{in}$$

$$A_v := 1920\text{in}^2 \quad A_h := 215.76\text{in}^2 \quad V := 124800\text{in}^3$$

Tsunami Conditions

$$h_{max} := 669.2\text{in} \quad u_x := 321.0 \frac{\text{in}}{\text{s}} \quad u_v := 16.6 \frac{\text{in}}{\text{s}}$$

$$a_{max} := 844.2 \frac{\text{in}}{\text{s}^2} \quad \text{flux}_{max} := 6395 \cdot 10^3 \frac{\text{in}^3}{\text{s}^2}$$

General Conditions

$$g := 386 \frac{\text{in}}{\text{s}^2} \quad \gamma_w := 62 \frac{\text{lb}}{\text{ft}^3} \quad \gamma_s := 1.2 \cdot \gamma_w = 74.4 \frac{\text{lb}}{\text{ft}^3}$$

$$\rho_s := 1.2 \cdot \frac{\gamma_w}{g} = 2.313 \frac{\text{lb} \cdot \text{s}^2}{\text{ft}^4}$$

1. Douglass et al. (2006)'s method for estimating wave forces on bridge decks

$$C_r := 0.4 \quad C_{h.va} := 1 \quad C_{h.im} := 6$$

$$C_{v.va} := 1 \quad C_{v.im} := 3$$

$$\Delta z := h_{max} - h_{br} = 5.767\text{ft}$$

$$F_{H,Douglass} := \left[\left[1 + C_r \cdot (N - 1) \right] \cdot C_{h.va} + C_{h.im} \right] \cdot \gamma_s \cdot \Delta z \cdot \frac{A_h}{b} = 1.8 \times 10^4 \frac{\text{lb}}{\text{ft}}$$

$$F_{V,Douglass} := (C_{v.va} + C_{v.im}) \cdot \gamma_s \cdot \Delta z \cdot \frac{A_v}{b} = 9.153 \times 10^4 \frac{\text{lb}}{\text{ft}}$$

2. FEMA P646 (2008), Guidelines for Design of Structures for Vertical Evacuation from Tsunamis

$$C_d := 2 \quad C_u := 3$$

$$\text{Hydrostatic Force : } F_{hs} := \gamma_s \cdot \Delta z \cdot A_h = 642.845 \text{ lb}$$

$$\text{Hydrodynamic Force: } F_d := 0.5 \cdot \rho_s \cdot C_d \cdot b \cdot \text{flux}_{\max} = 2.14 \times 10^3 \text{ lb}$$

$$\text{Impulsive Force: } F_i := 1.5 \cdot F_d = 3.21 \times 10^3 \text{ lb}$$

$$F_{H.FEMA} := \frac{(F_{hs} + F_d + F_i)}{b} = 2.397 \times 10^4 \frac{\text{lb}}{\text{ft}}$$

$$\text{Buoyant Force: } F_b := \gamma_s \cdot V = 5.373 \times 10^3 \text{ lb}$$

$$\text{Uplift Force: } F_u := 0.5 \cdot C_u \cdot \rho_s \cdot A_v \cdot u_v^2 = 88.522 \text{ lb}$$

$$F_{V.FEMA} := \frac{(F_b + F_u)}{b} = 2.185 \times 10^4 \frac{\text{lb}}{\text{ft}}$$

3. Performance-Based Tsunami Engineering (PBTE): Tsunami bore on vertical wall and slab

Bridge Longitudinal Span Length: $L := 210\text{ft}$

Width to inundation depth ratio: $R := \frac{L}{\Delta z} = 36.416$

$$C_{d.PBTE} := \begin{cases} 1.25 & \text{if } 1 < R < 12 \\ 1.3 & \text{if } 12 < R < 20 \\ 1.4 & \text{if } 20 < R < 32 \\ 1.5 & \text{if } 32 < R < 40 \\ 1.75 & \text{if } 40 < R < 80 \\ 1.8 & \text{if } 80 < R < 120 \\ 2.0 & \text{if } R > 120 \end{cases} = 1.5$$

Hydrodynamic Force: $F_{d.PBTE} := 0.5 \cdot \rho_s \cdot C_{d.PBTE} \cdot b \cdot \Delta z \cdot u_x^2 = 1.79 \times 10^3 \text{ lb}$

Hydrostatic Force: $F_{hs.PBTE} := 0.5 \cdot \rho_s \cdot g \cdot b \cdot \Delta z^2 = 309.266 \text{ lb}$

$$F_{H.PBTE} := \frac{(F_{d.PBTE} + F_{hs.PBTE})}{b} = 8.395 \times 10^3 \frac{\text{lb}}{\text{ft}}$$

$$\beta := \frac{\Delta z}{h_{\max}} = 0.103$$

$$C_{u.PBTE} := \begin{cases} \beta \cdot \frac{3}{0.5} & \text{if } \beta < 0.5 \\ 3 & \text{if } 0.5 < \beta < 1.5 \end{cases} = 0.62$$

Buoyant Force: $F_{b.PBTE} := \gamma_s \cdot V = 5.373 \times 10^3 \text{ lb}$

Uplift Force: $F_{u.PBTE} := 0.5 \cdot C_{u.PBTE} \cdot \rho_s \cdot u_x^2 \cdot A_v = 6.846 \times 10^3 \text{ lb}$

$$F_{V.PBTE} := \frac{(F_{b.PBTE} + F_{u.PBTE})}{b} = 4.888 \times 10^4 \frac{\text{lb}}{\text{ft}}$$

4. The Recommended Approach for estimating tsunami forces on bridge superstructures

$$C_{d,\text{recommend}} := 3.5$$

$$\text{Hydrostatic Force: } F_{\text{hs.recommend}} := [1 + C_r \cdot (N - 1)] \cdot \gamma_s \cdot \Delta z \cdot A_h = 642.845 \text{ lb}$$

$$\text{Hydrodynamic Force: } F_{\text{d.recommend}} := 0.5 \cdot C_{d,\text{recommend}} \cdot \rho_s \cdot b \cdot \text{flux}_{\text{max}} = 3.745 \times 10^3 \text{ lb}$$

$$F_{\text{H.recommended}} := \frac{(F_{\text{hs.recommend}} + F_{\text{d.recommend}})}{b} = 1.755 \times 10^4 \frac{\text{lb}}{\text{ft}}$$

$$u_{\text{x.out}} := 1.0 \cdot u_x = 26.75 \frac{\text{ft}}{\text{s}}$$

$$\text{Buoyant Force: } F_{\text{b.recommend}} := \gamma_s \cdot \Delta z \cdot A_v = 5.721 \times 10^3 \text{ lb}$$

$$\text{Uplift Force: } F_{\text{u.recommend}} := 0.5 \cdot \rho_s \cdot u_{\text{x.out}}^2 \cdot A_v = 1.103 \times 10^4 \text{ lb}$$

$$F_{\text{V.recommend}} := \frac{(F_{\text{b.recommend}} + F_{\text{u.recommend}})}{b} = 6.702 \times 10^4 \frac{\text{lb}}{\text{ft}}$$

Note that the method proposed by Bea et al. (1999) is for estimating wind-induced wave forces on a platform deck of offshore structures which is not applicable to the tsunami case.

A comparison of the example calculations for the Schooner Creek Bridge and the Spencer Creek Bridge shows that the total horizontal force for the Schooner Creek Bridge is mainly influenced by the hydrostatic force, while for the Spencer Creek Bridge, the hydrodynamic force is a major contribution to the total horizontal force. This behavior is caused by the differences between (1) the tsunami flow fields (water elevation and velocity) for two bridge sites, (2) the bridge elevations, and (3) the applied drag coefficients computed from numerical modeling. In general, for high bridges subjected to less inundation (e.g. Spencer Creek Bridge) the hydrodynamic force is the dominant effect on the total horizontal force and the hydrostatic force is the second most influential. However, for short bridges (e.g. Schooner Creek Bridge) facing large inundation, the hydrostatic force plays the main role due to the significant difference between bridge elevation and water surface elevation.

**APPENDIX E:
DRAWINGS OF SELECTED BRIDGES**

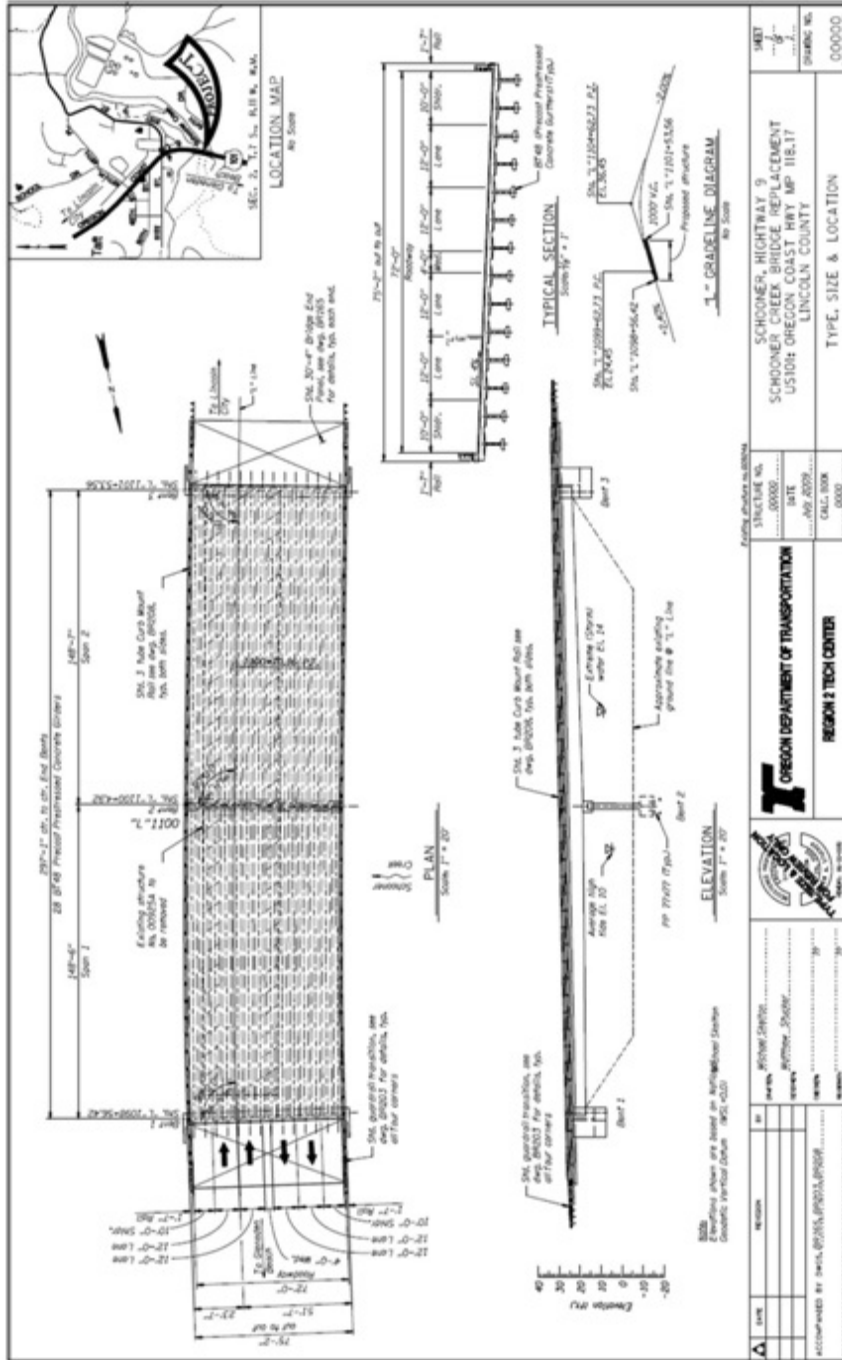


Figure E.1: Preliminary drawing of Schooner Creek Bridge (deck-girder)

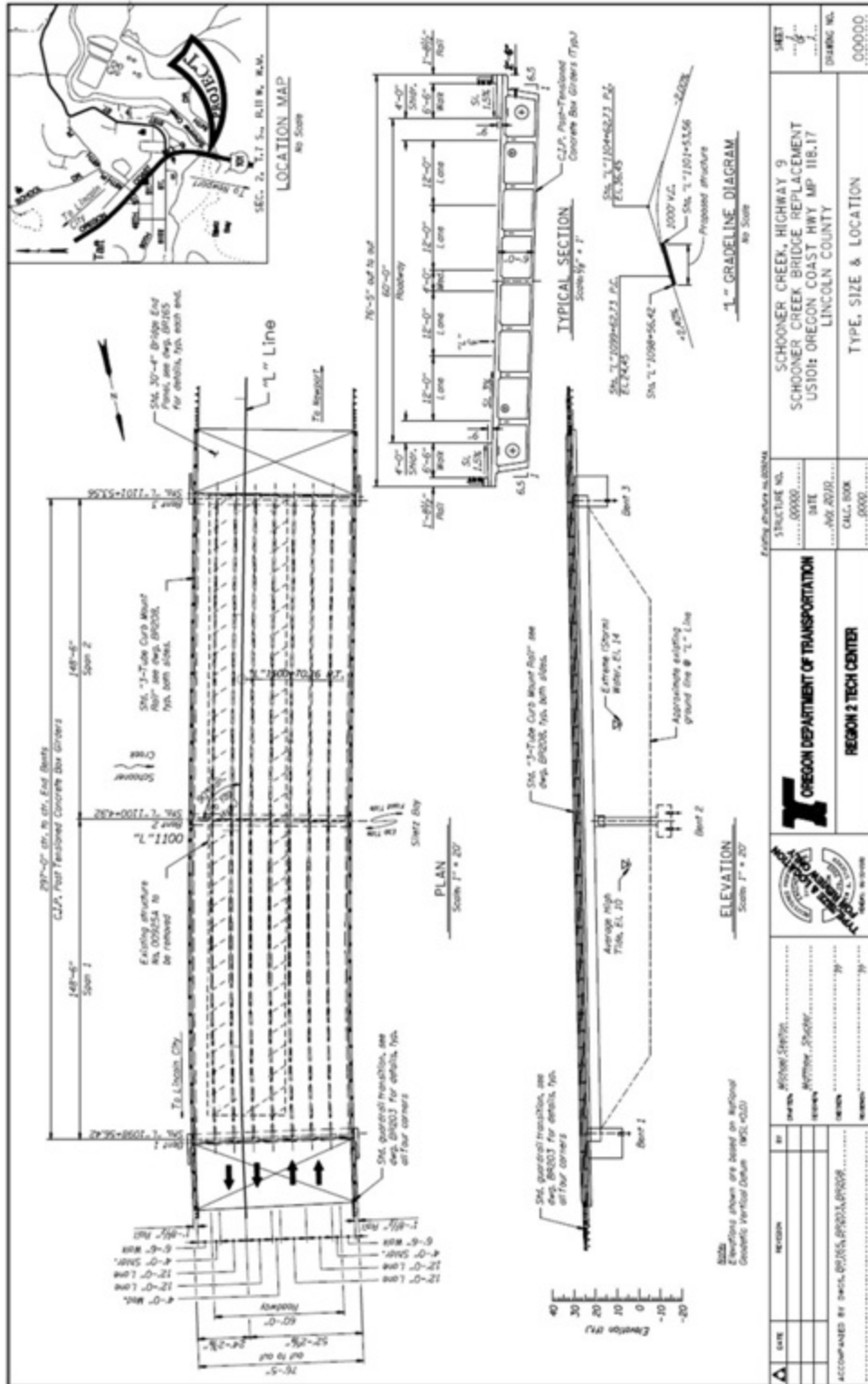
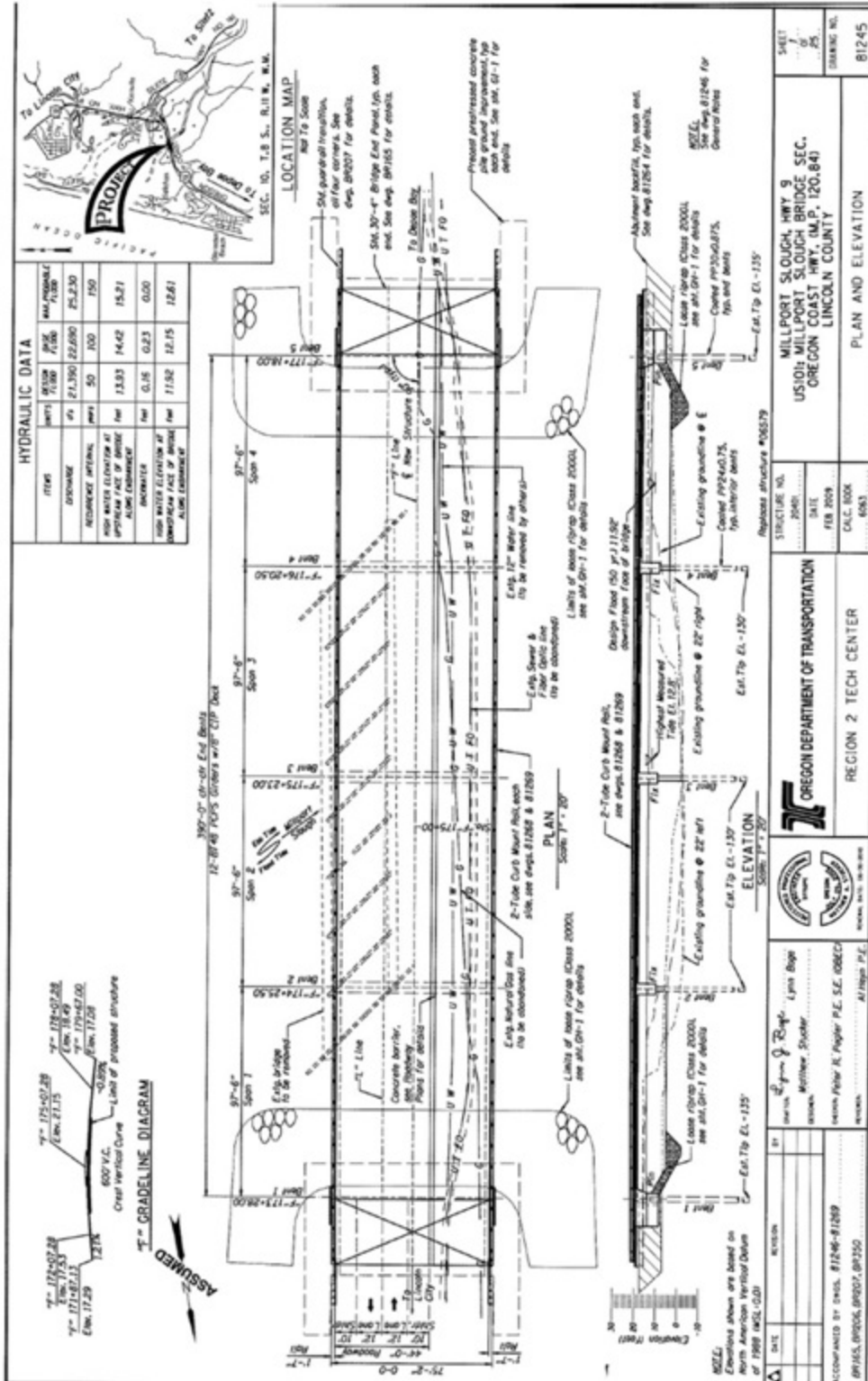


Figure E.2: Preliminary drawing of Schooner Creek Bridge (box-section)



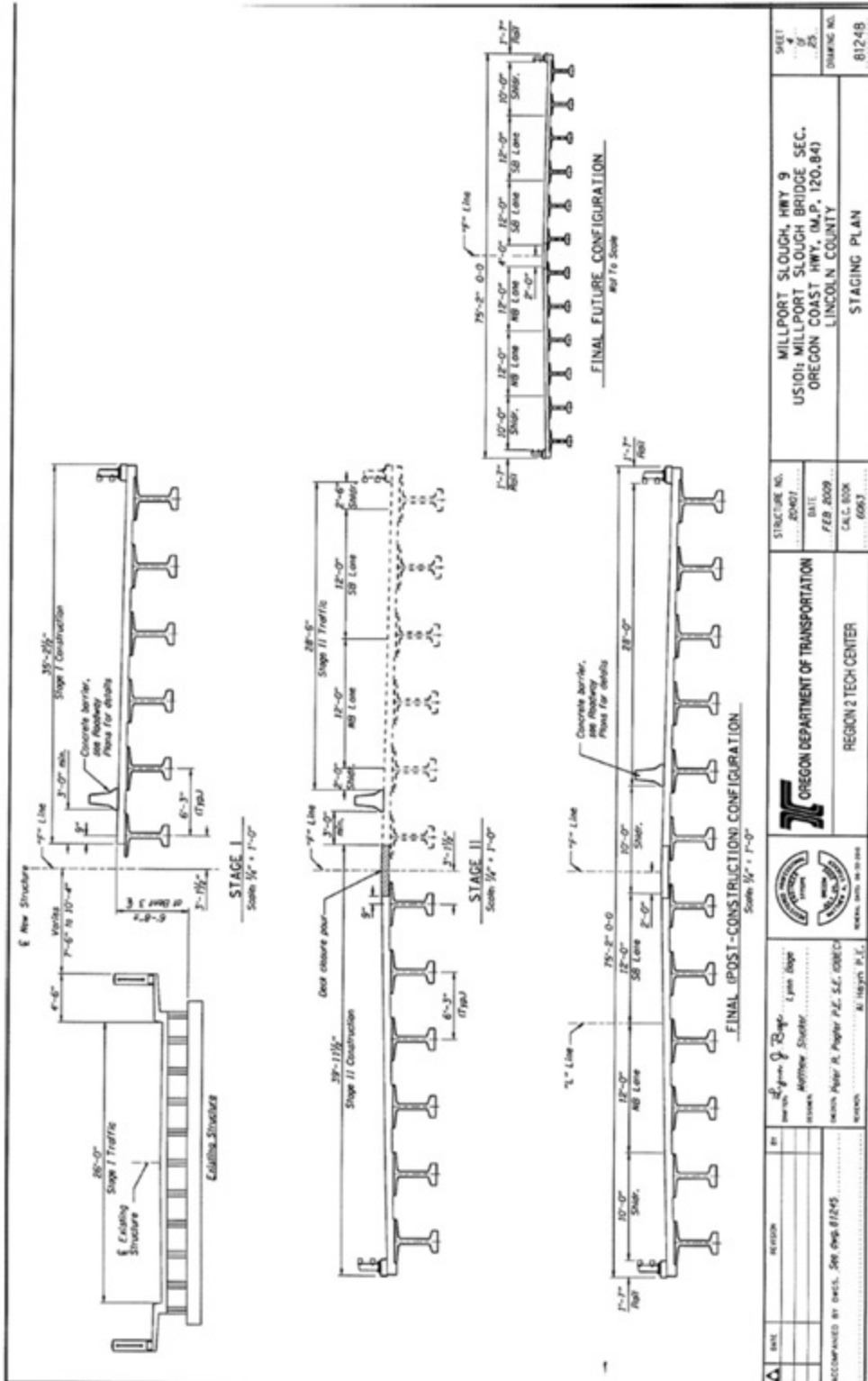


Figure E.5: Staging plan of new Millport Slough Bridge

**APPENDIX F:
MODELING OF 500-YEAR CASCADIA TSUNAMIS AND INNUNDATION
AT SILETZ BAY, OREGON**

F-1 CASCADIA EARTHQUAKE SCENARIOS

The documentation for the 2008 update of the National Seismic Hazard Maps describes the Cascadia subduction zone and its implementation in the Pacific Northwest seismic source model (Petersen et al. 2008). Figure F.1 shows the rupture boundaries of the 500-year earthquake that extend about 1,100 km from Cape Mendocino in northern California to Vancouver Island in British Columbia. The western boundary of the rupture is along the trench at the base of the continental slope. A 500-year rupture involves the entire locked zone (LZ) and may extend to the midpoint (MT) and the base (BT) of a plastic transition zone (Wang et al. 2003). In addition, global analogs (GA) of shallow-dipping subduction zones from Tichelaar and Ruff (1993) place the eastern boundary of the rupture at 123.8°W around a depth of 30 km. The logic tree in the Pacific Northwest seismic source model assigns occurrence probabilities of 0.1, 0.2, 0.2, and 0.5 to the LZ, MT, BT, and GA rupture configurations and a probability of 0.6 to moment magnitude Mw 9.0 versus 0.2 to Mw 8.8 and 9.2. Table F.1 provides the joint probability distribution of the rupture configuration and magnitude of the 500-year event.

The ground surface deformation, which includes uplift, subsidence, and offset, is a linear function of the slip and dimensions of the fault. Superposition of planar faults thus describes ground surface deformation due to more general rupture configurations. Figure F.2 shows mosaics of 50 to 550 planar faults that model the four rupture configurations of the 500 year Cascadia earthquake.

Figure F.2 also shows the slip distributions of the four rupture configurations for Mw 9.0. The slip in the locked zones of the MT, BT, and GA ruptures decreases from 21.0 to 15.4 m due to the increasing size of the transition zone. Superposition of the planar fault solutions from the subfaults gives the earth surface deformation. Figure F.3 shows the computed vertical displacement of the seafloor for the four rupture configurations at Mw 9.0. Because of the depth of the faults, the granularity of the rupture model does not seem to affect the surface deformation appreciably. The dip angle of the subduction zone results in uplift on the ocean side and a large area of subsidence extending to the coastlines. The LZ rupture has the highest uplift and subsidence of 10.7 m and 6.7 m. The uplift of MT, BT, and GA decreases from 8.4 to 6.2 m and the subsidence decreases from 4.5 to 2.3 m due to the increasing size of the transition zone. The uplift and subsidence of the seafloor displace the ocean water and generate a tsunami. Earthquakes typically have rupture durations of minutes, which can be considered as instantaneous comparing to the time scale of the subsequent tsunamis. The Cascadia Subduction Zone, however, may have a long rupture time similar to that of the 2004 Sumatra earthquake. It is a concern whether a slow rupture may result in different tsunami impacts. In the present study, the initial tsunami waveform assumes the vertical component of the seafloor deformation. This approach is conservative as it generates a near-field tsunami that hits the entire coast at the same time, but has been the standard in modeling tsunamis for hazard assessment and emergency planning.

Table F.1: Joint Probability of Rupture Scenarios from the 2800 National Seismic Hazard Maps

Rupture	Moment Magnitude, M_w			<u>Total</u>
	8.8	9	9.2	
LZ	0.02	0.06	0.02	0.1
MT	0.04	0.12	0.04	0.2
BT	0.04	0.12	0.04	0.2
GA	0.1	0.3	0.1	0.5
<u>Total</u>	0.2	0.6	0.2	1

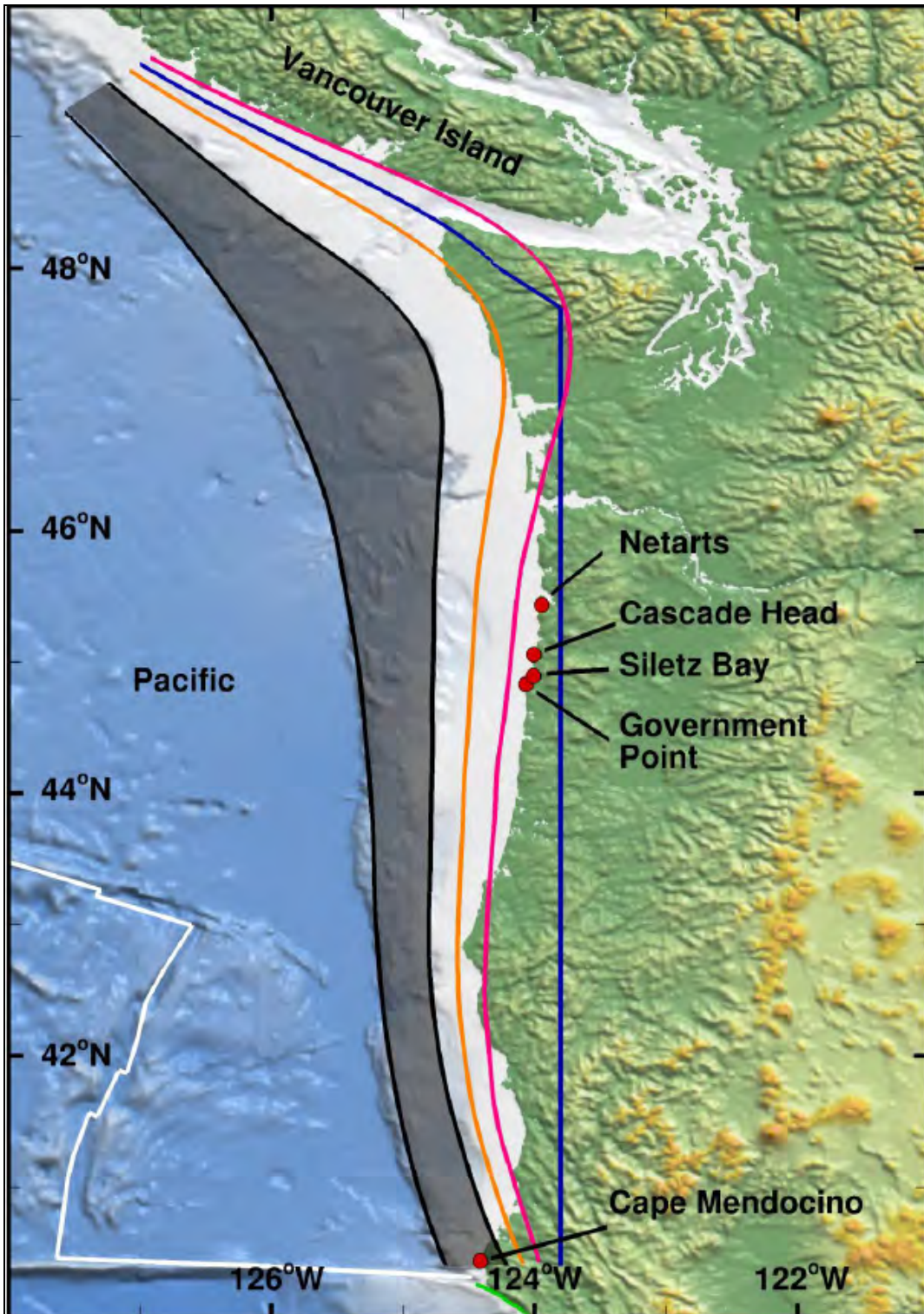


Figure F.1: Boundaries of the Cascadia Subduction Zone inferred from the 2008 National Seismic Hazard Map. Black line indicates west and east boundaries of locked zone (LZ); orange line indicates middle of transition zone (MT); pink lines indicates base of transition zone (BT), and blue line indicates 30-km depth based on global analog (GA).

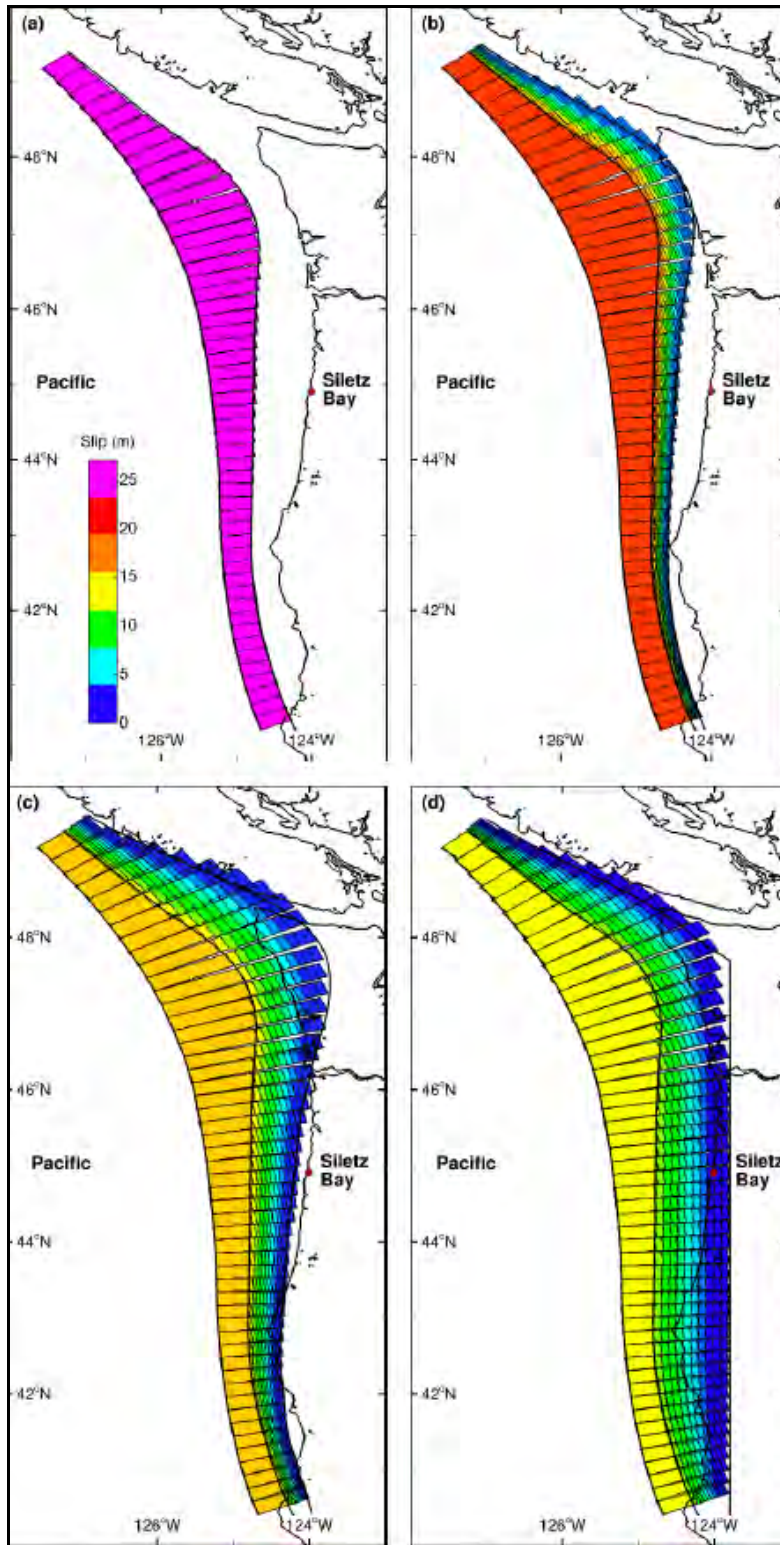


Figure F.2: Implementation of the planar fault model for 500-year Cascadia rupture configurations. (a) Rupture of locked zone only (LZ). (b) Rupture extending to the middle of transition zone (MT). (c) Rupture extending to the base of transition zone (BT). (d) Rupture extending to the 30-km depth (GA).

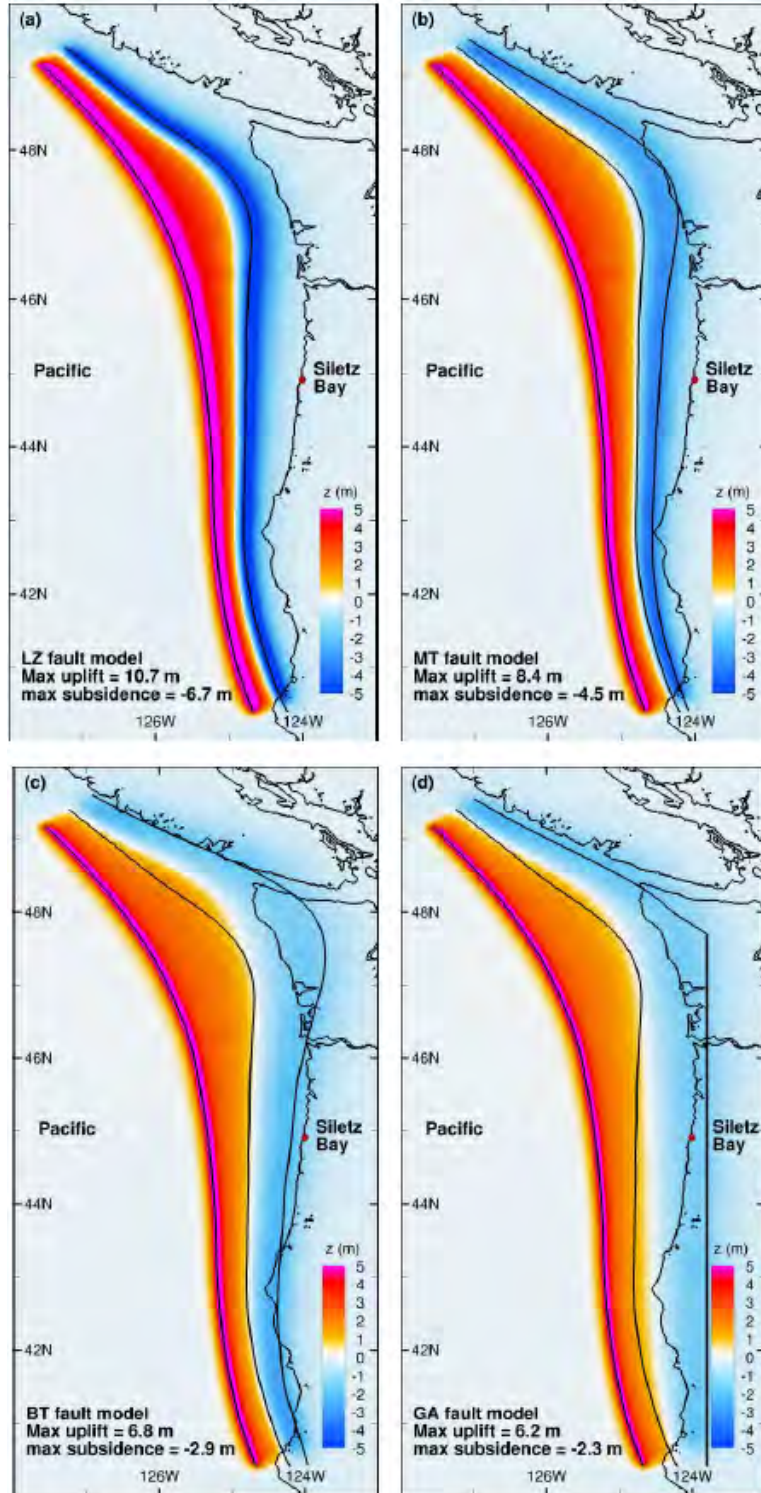


Figure F.3: Earth surface deformation due to earthquake ruptures at Mw 9.0. (a) Rupture of locked zone only (LZ). (b) Rupture extending to the middle of transition zone (MT). (c) Rupture extending to the base of transition zone (BT). (d) Rupture extending to the 30-km depth (GA).

F-2 SITE CHARACTERIZATION

The Pacific Northwest coast consists of long stretches of beaches separated by massive headlands. The embayments form a series of self-contained littoral cells, which typically include estuaries, barrier beaches, and inlets. Siletz Bay is a salt marsh in the littoral cell between Government Point and Cascade Head (see Figure F.1). Information on the physical environment, coastal morphology, and paleotsunami deposits is available in the technical literature for this region.

Figure F.4 shows an aerial view of Siletz Bay as well as the locations of the four bridges along the US 101 Pacific Coast Highway. The image comprises aerial photos probably taken at low tides. The un-vegetated inter-tidal flats are exposed and the channels clearly discernable. A sand spit extending from the south separates the bay from the Pacific Ocean. An inlet channel at the north end allows exchange of tidal and freshwater. The mixed semi-diurnal tides have a full tide range of 2.1 m at Netarts 60 km to the north. The tides transport a portion of the longshore sand via an east-west flood channel to the inter-tidal flat between Taft and Cutler City and to the downdrift coast through the north-south ebb channel. The sand wave pattern at the inter-tidal flat adjacent to the inlet channel demonstrates the seasonal effects of the bypassing processes. The shores to the south of Cutler City show predominantly terrestrial deposits with vegetation growth and appear to be more stable and unaffected by the inlet processes.

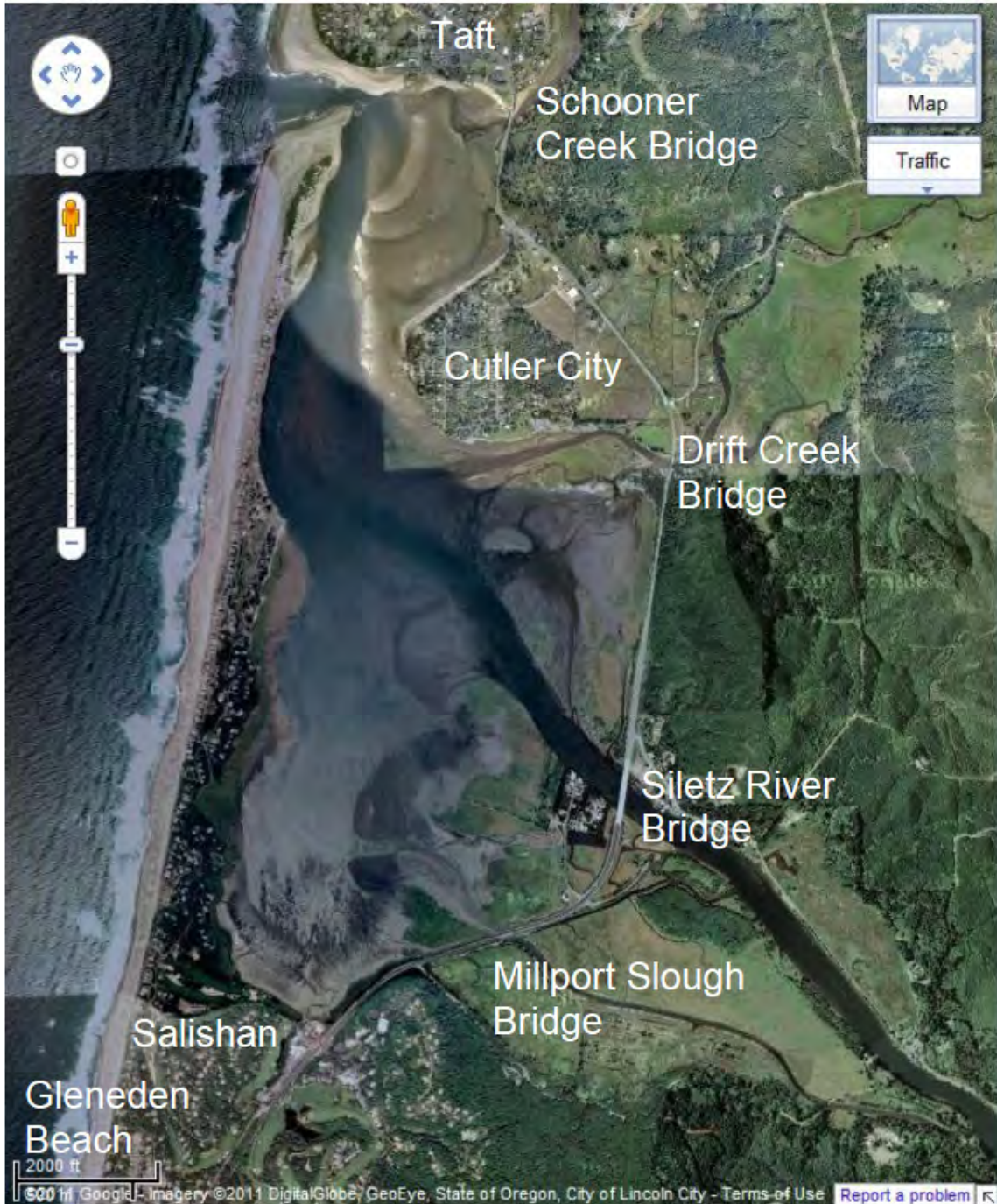


Figure F.4: Aerial photo of Siletz Bay from Google Map.

F-3 TSUNAMI MODELING

The nonlinear shallow-water equations have many applications in modeling of long waves such as tides, storm surge, and tsunamis. The finite difference method, owing to its simplicity in formulation and ease of implementation, is widely used in the solution of the nonlinear shallow

water equations. Researchers have made significant efforts in improving numerical schemes and boundary treatments to model tsunami propagation and inundation.

These explicit schemes provide efficient solutions for large computational problems, thereby enabling their extensive application in modeling of tsunamis and the associated flood hazards. The commonly used finite difference schemes, however, are non-conservative leading to volume loss and energy dissipation as the wave steepness increases and the flow approaches discontinuous. This turns into an important modeling issue when tsunami bores or hydraulic jumps develop near-shore and the results become grid-size dependent.

F-4 DIGITAL ELEVATION MODEL

Modeling of tsunami propagation and inundation requires accurate bathymetry across the ocean and high-resolution topography near the coast. We utilize four levels of nested computational grids in spherical coordinates with increasing resolution from the northeastern Pacific to Siletz Bay as shown in Figure F.5. The system of grids captures bathymetric and topographic features at scales and resolution appropriate to the physical processes. The National Geophysical Data Center (NGDC) Global Relief Model ETOPO1 at 1' (~1800-m) resolution and the Coastal Relief Model at 3" (~90-m) resolution define the topography and bathymetry in the first three levels of computational grids. The level-1 grid covers the northeastern Pacific Ocean at 1' resolution and provides an open boundary condition for offshore propagation of tsunami energy. The grid includes sufficient details such as the Juan de Fuca Ridge and the adjacent fracture zones that would modify the near-field tsunami. The level-2 grid captures tsunami transformation over the continental margin off the Washington and Oregon coasts at 15" (~450-m) resolution. Vertical walls are applied along the coastlines at the level-1 and 2 grids to avoid excessive and unrealistic waterline movements associated with the large grid size. The level-3 grid describes tsunami transformation along the coast at 3" (~70 to 90-m) resolution. The moving boundary conditions are applied at level 3 to model flow conditions at the shores adjacent to Siletz Bay, where high-resolution inundation calculation is performed. The level-4 grid covers Siletz Bay at 0.3" (~7 to 9-m) resolution for computation of detailed flow conditions at the four bridge sites. The grid also covers the dune system at Glenedan beach and the area upstream of Millport Slough.

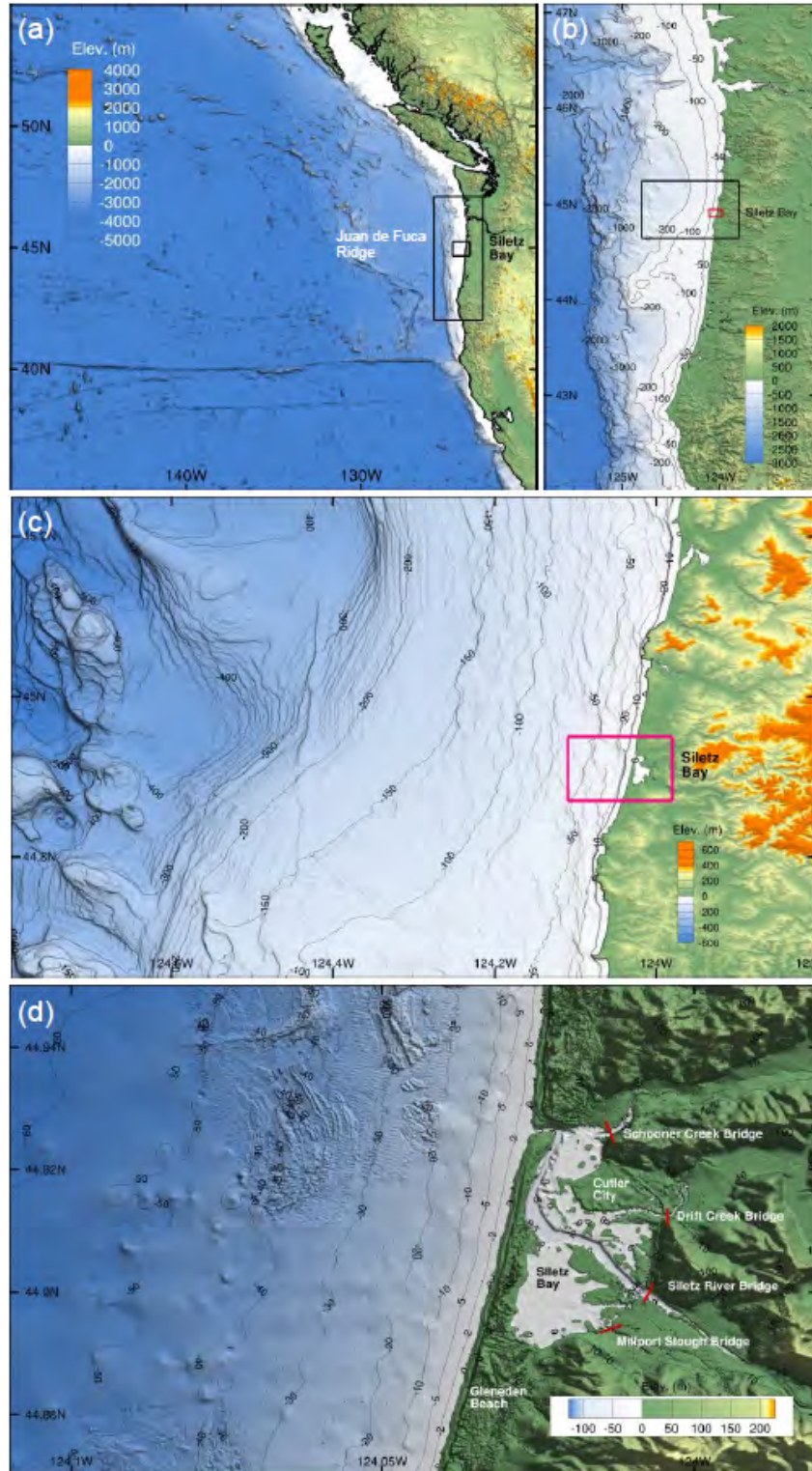


Figure F.5: Four levels of two-way nested computational grids. (a) Northeast Pacific. (b) Continental Shelf. (c) Oregon Coast. (d) Siletz Bay.

F-5 TSUNAMI SCENARIOS

The National Seismic Hazard Maps includes 12 scenarios of the 500-year Cascadia earthquake in the Pacific Northwest seismic source model as summarized in Table F.1. The GA rupture has the highest probability of 0.5 among the four configurations and an M_w 9.0 earthquake has a probability of 0.6. For illustration, we present the results of the four rupture configurations at M_w 9.0 to cover the uncertainty in defining the transition zone as well as the results of the GA rupture at M_w 8.8 and 9.2 to account for the range of potential earthquake magnitude. The initial conditions correspond to the mean higher high water (MHHW) level with the earth and sea surface deformations associated with the earthquake. The subsidence at Siletz Bay ranges from 0.3 to 1.5 m for the four ruptures at M_w 9.0 and from 0.74 to 3.0 m for the GA rupture at M_w 8.8 to 9.2. The subsidence lowers the bridges, while the water-level definitions, such as MSL and MHHW, remain unchanged by the earth surface deformation.

We first examine the tsunami resulting from the GA rupture at M_w 9.0. This rupture causes 1.46 m of subsidence at Siletz Bay consistent with that postulated for the paleotsunami events (Peterson et al. 1993). Figure F.6 and Figure F.7 show the surface elevations over the level-1 and 4 grids when successive waves arrive at Siletz Bay. The rupture generates tsunami waves in two offshore directions resulting in a prominent initial crest in the overlapping region. The onshore wave overtops the spit in 30 minutes after the earthquake. The high-speed flows through the inlet channel and over the spit develop into a series of hydraulic jumps and bores in the initially quiescent bay. The headland adjacent to Schooner Creek and a 90° bend at 1 km upstream reflect the tsunami bores forming a complex flow pattern near the inlet channel and flooding the Taft area to the west of the creek. A component of the flood waves propagates south reinforcing the bores generated by overtopping of the spit to inundate Cutler City. The reflected waves from the coastline show characteristics of bores and a component of the reflected energy propagates along the shore as edge waves. At $t = 53$ min, the reflected waves from the coast reach the continental margin, while the Juan de Fuca Ridge begins to reflect the offshore component of the tsunami back to the coast. An edge wave overtops the northern tip of the spit and produces a second series of bores, exacerbating the flood conditions in Siletz Bay.

The continental margin resembles the open boundary of a basin in the classical harbor resonance problem. The shallow and wide continental shelf along the Oregon and Washington coasts traps a significant amount of tsunami energy from the onshore component of the initial wave as well as the reflection from the Juan de Fuca Ridge. The prominent headlands along the Pacific Northwest coast form a series of embayments prone to standing tsunami edge waves.

Figure F.6 shows significant large-scale wave activities along the Washington and Oregon coast more than 2.5 hours after the earthquake. The standing wave at the embayment between Government Point and Cascade Head reaches 3 m amplitude outside the inlet and injects additional floodwater into the bay. This type of regional resonance has produced persistent and large-scale oscillations over continental and insular shelves in the aftermath of tsunamis (e.g., Munger and Cheung 2008; Roeber et al. 2010; Yamazaki and Cheung 2011). Since the outflow through the inlet channel is slow, the water level in the bay continues to rise for a few hours after the initial wave.

We next examine the sensitivity of the 500-year Cascadia tsunami to rupture configuration and earthquake magnitude. Figure F.8 shows the maximum surface elevation and flow speed at Siletz Bay generated by the GA rupture. At M_w 8.8, the 6 to 7-m amplitude tsunami at the shore overtops the northern tip and a mid section of the spit. This supplies enough floodwater to cover most of Cutler City and part of the downstream alluvial plains. The tsunami generated by the M_w 9.0 earthquake reaches over 10 m elevation on the shores and overtops the entire sand spit. The floodwater reaches an elevation of 7 m near Schooner Creek Bridge and inundates all areas below the 4.5-m elevation contour. The surge covers Cutler City and Millport Slough and propagates upstream of Schooner Creek, Drift Creek, and Siletz River. High-speed flows are evident at the inlet channel, the spit as well as Salishan, where the floodwater overtops the 6-m dune and rushes down into the bay. The tsunami generated by the M_w 9.2 rupture produces a 15 to 20 m amplitude wave at the shore. The wave overtops a 16-m high section of the sand dune at Gleneden Beach and the floodwater in the low-lying backshore area flows into Siletz Bay along the US 101 Highway. High-speed flows associated with the tsunami waves extend to the back valleys and produce extensive flooding of the region beyond Siletz Bay.

Figure F.9 shows the maximum surface elevation and flow speed at Siletz Bay from the tsunamis generated by the BT, MT, and LZ ruptures at M_w 9.0. These tsunamis are more severe than that generated by the GA rupture, because the smaller fault areas result in higher initial wave amplitudes for the same earthquake magnitude. The higher amplitude and flow speed come with shorter periods of the tsunami waves. For a small coastal feature such as Siletz Bay, the wave amplitude and flow speed rather than the period determine the overall impact. The BT, MT, and LZ ruptures generate tsunamis reaching 13, 17, and 20 m elevation outside Siletz Bay that overtop the entire spit as well as a low section of the sand dune at Gleneden Beach. The floodwater flows along the US 101 Highway into the bay from the south. The flood waves propagate to the back valley areas of Drift Creek and deep into the Schooner Creek and Siletz River valleys in all three scenarios. The tsunami generated by the LZ rupture at M_w 9.0 produces higher flood levels and similar flow speeds in the bay compared to those of the GA rupture at M_w 9.2. The latter, however, generates a tsunami with longer periods that drives the floodwater further upstream of the rivers and creeks.

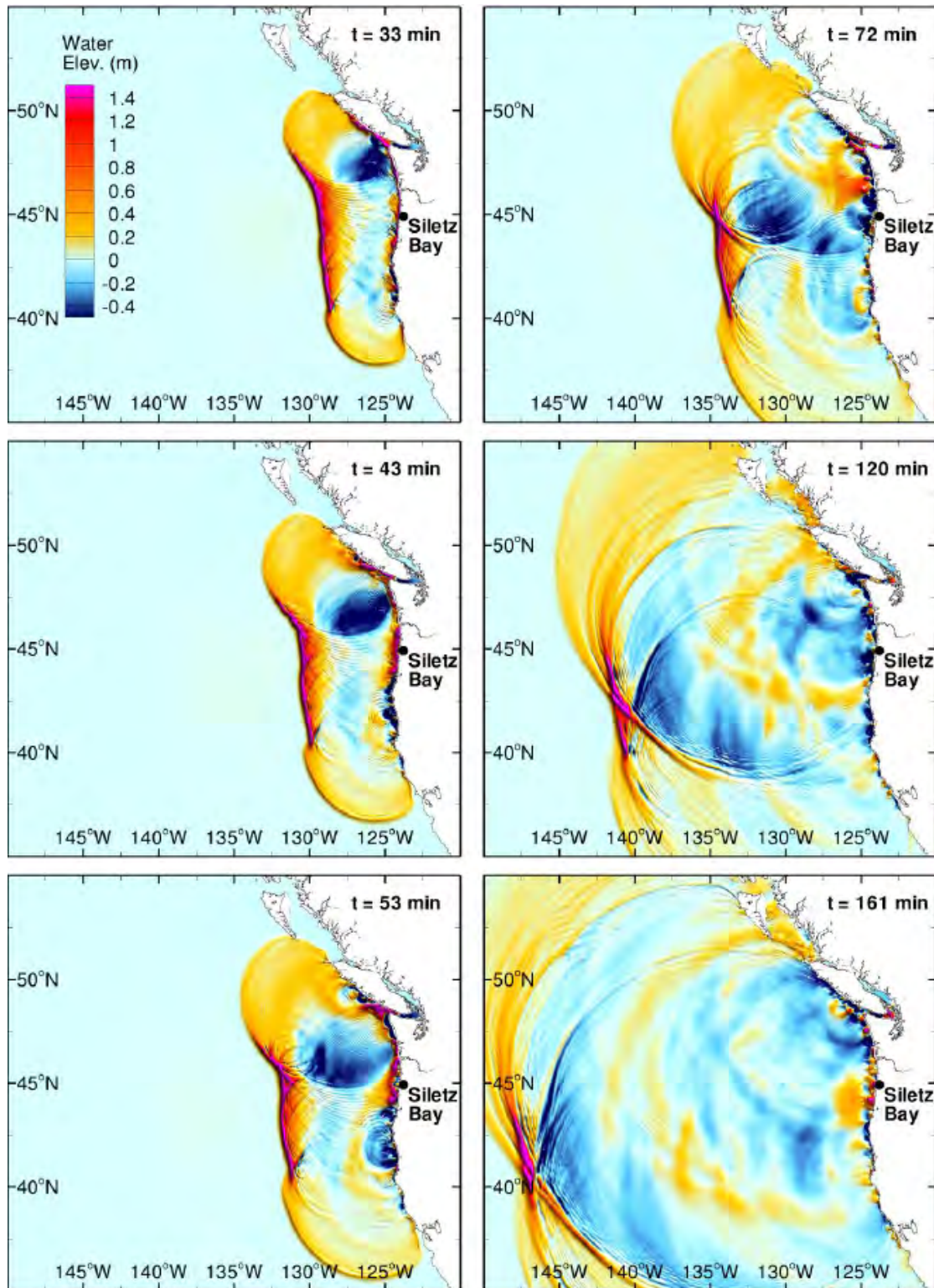


Figure F.6: Computed surface elevation in level-1 grid for the GA rupture at Mw 9.0.

F-6 DESIGN FLOWS AND IMPLEMENTATION

The modeled tsunami scenarios provide the 500-year flow conditions for bridge design and assessment. Figure F.10 to Figure F.13 present the results at the four bridge sites along the shore of Siletz Bay from north to south. The water surface elevation is positive above MSL. The velocity components are normal and tangential to each bridge and are positive in the upstream direction and toward the right (when facing upstream). For each tsunami scenario, the initial water level drops from the MHHW immediately after the rupture due to ground subsidence. The computation provides four hours of event time until the wave activities subside and the water level shows sign of decrease. The abrupt increase of the surface elevation and flow speed from the initial quiescent conditions indicates the tsunami waves overtop the spit and propagate across the shallow bay as bores in the more severe scenarios. The results show a general decline of the impact from north to south because of the increasing height of the spit and the distance from the inlet channel.

Schooner Creek Bridge, which is located directly in front of the inlet channel, is open to the incoming tsunami waves and subject to the largest wave amplitude. Figure F.10 shows time series of the water surface elevation and velocity components at mid span of the bridge. For the GA and BT ruptures with larger transition zones, the tsunami initially produces a gradual increase of the flow at the site. Figure F.7 shows the arrival of the crest generates a bore locally at the inlet channel for the GA rupture at Mw 9.0 and provides an explanation for abrupt increase of the water level and flow speed to the peak. The tsunamis generated by the MT and LZ ruptures approach the bay as bores causing a sudden increase in the surface elevation and flow velocity at the bridge. Figure F.7 shows the 90° bend immediately upstream of the creek reflects part of the initial wave and provide an explanation for the large outflow velocity after the first peak in all the scenarios. The tangential velocity is small but not negligible because of the terrain and the bridge alignment with the creek. A steady outflow gradually develops for the more severe events in which the initial wave floods an extensive area upstream of the creek.

Figure F.11 shows a different time history of the flow at Drift Creek, which is located south of Cutler City in a more open area. At Mw 9.0 or higher, the tsunami overtops Siletz Spit as shown in Figure F.8 and generates a bore across the bay that causes an abrupt increase of the flow at Drift Creek. The initial wave propagates upstream without significant reflection from the wide alluvial plain. Figure F.12 depicts similar, but less severe flow conditions at Siletz River. The flow speed shows effects of the initial shock wave. The subsequent tsunami waves, however, have little impact to the site other than increasing the water level. At Millport Slough, the flow pattern is more complex as shown in Figure F.13. While the water level time history is similar to those at Siletz River and Drift Creek, the velocity components show significant oscillation due to reflection from the steep mountain slopes to the south. For the GA rupture at Mw 9.0, Figure F6 and Figure F7 show an edge wave over the continental shelf generates a surge into the bay around $t = 2:41$. The surge develops into a bore over Millport Slough that is subsequently reflected by the mountain slope causing the unusual flow velocity toward the end of the time series.

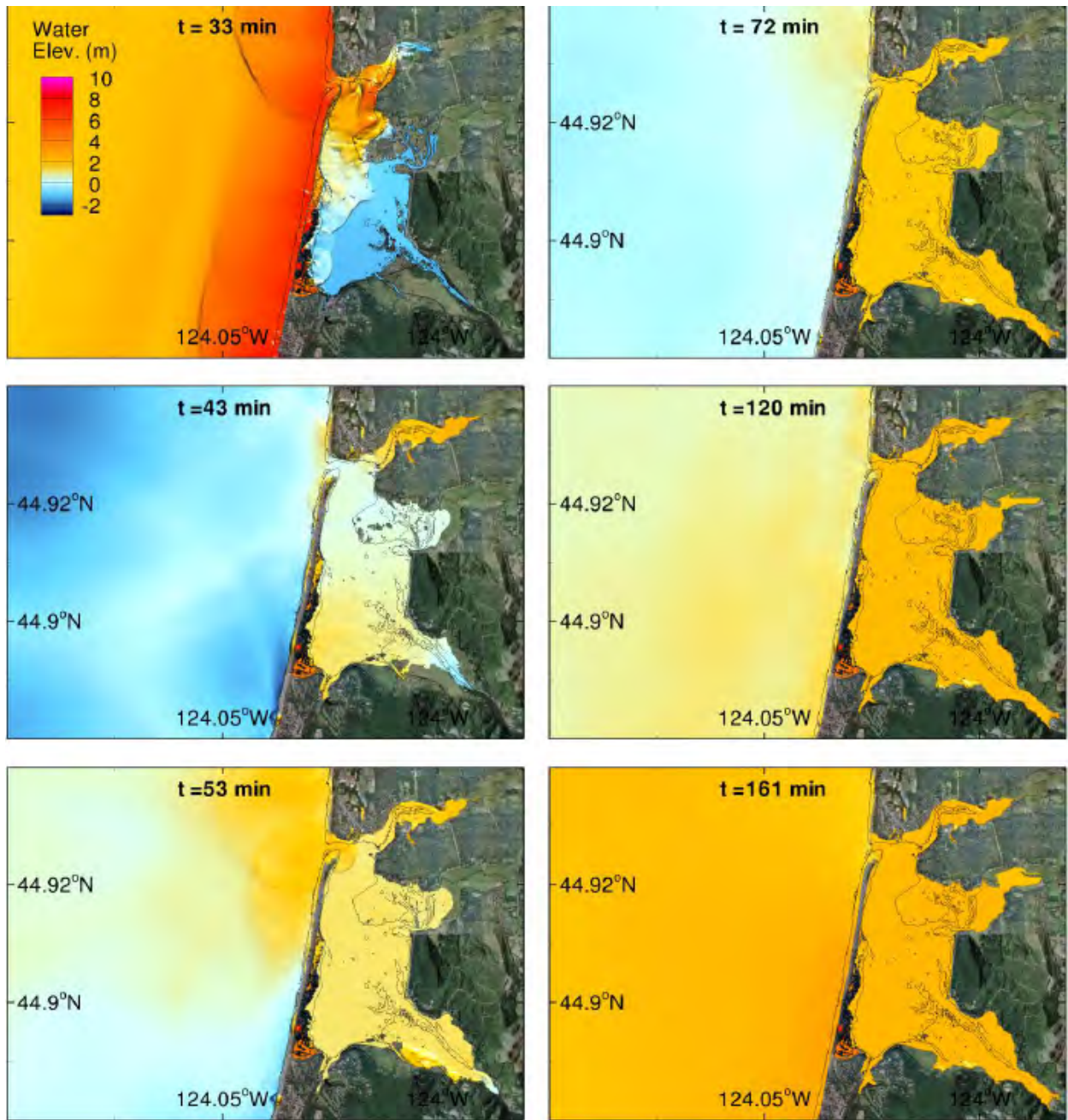


Figure F.7: Computed surface elevation in level-4 grid for the GA rupture at Mw 9.0.

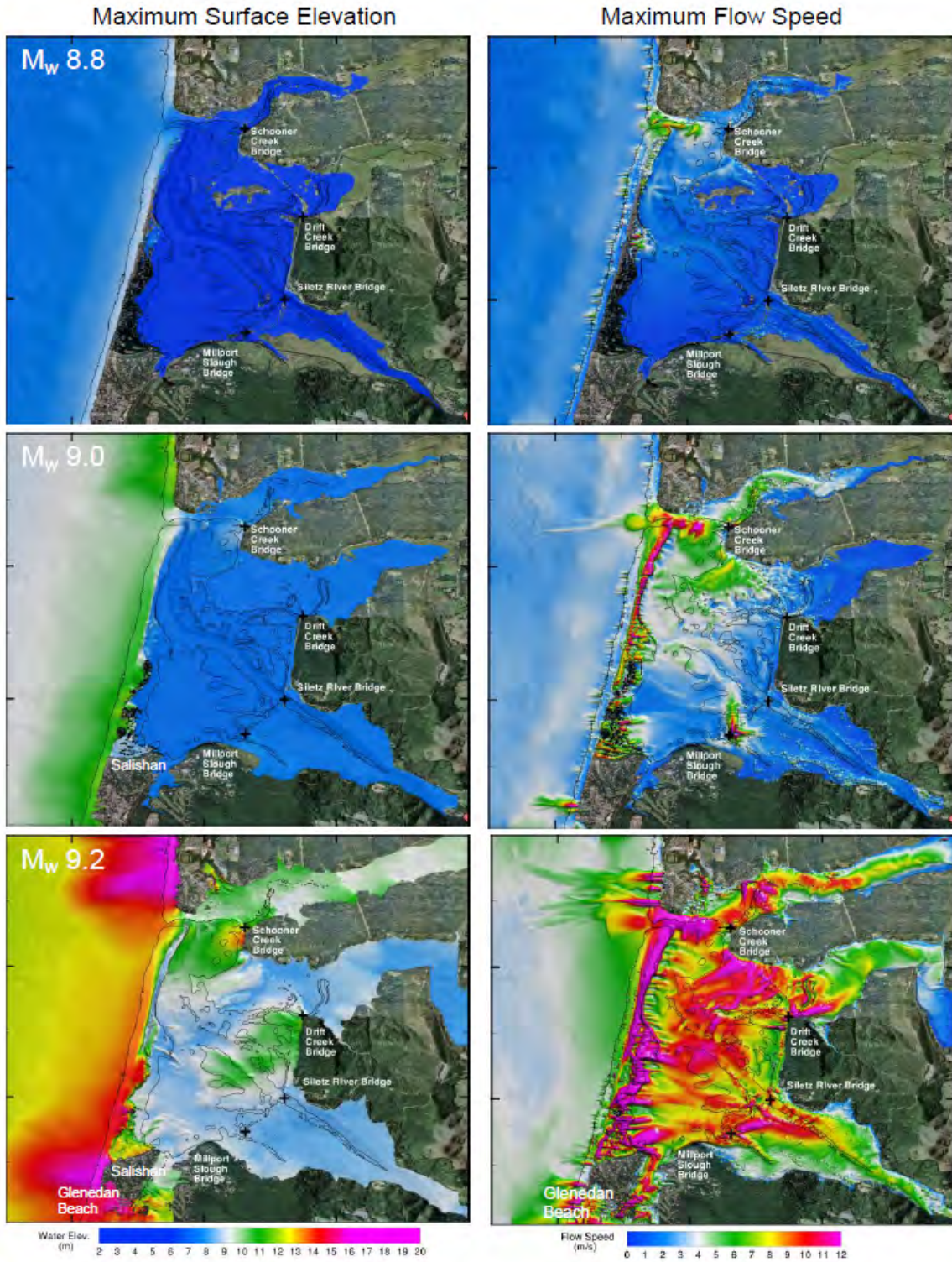


Figure F.8: Flow conditions at Siletz Bay for the GA rupture at M_w 8.8, 9.0, and 9.2.

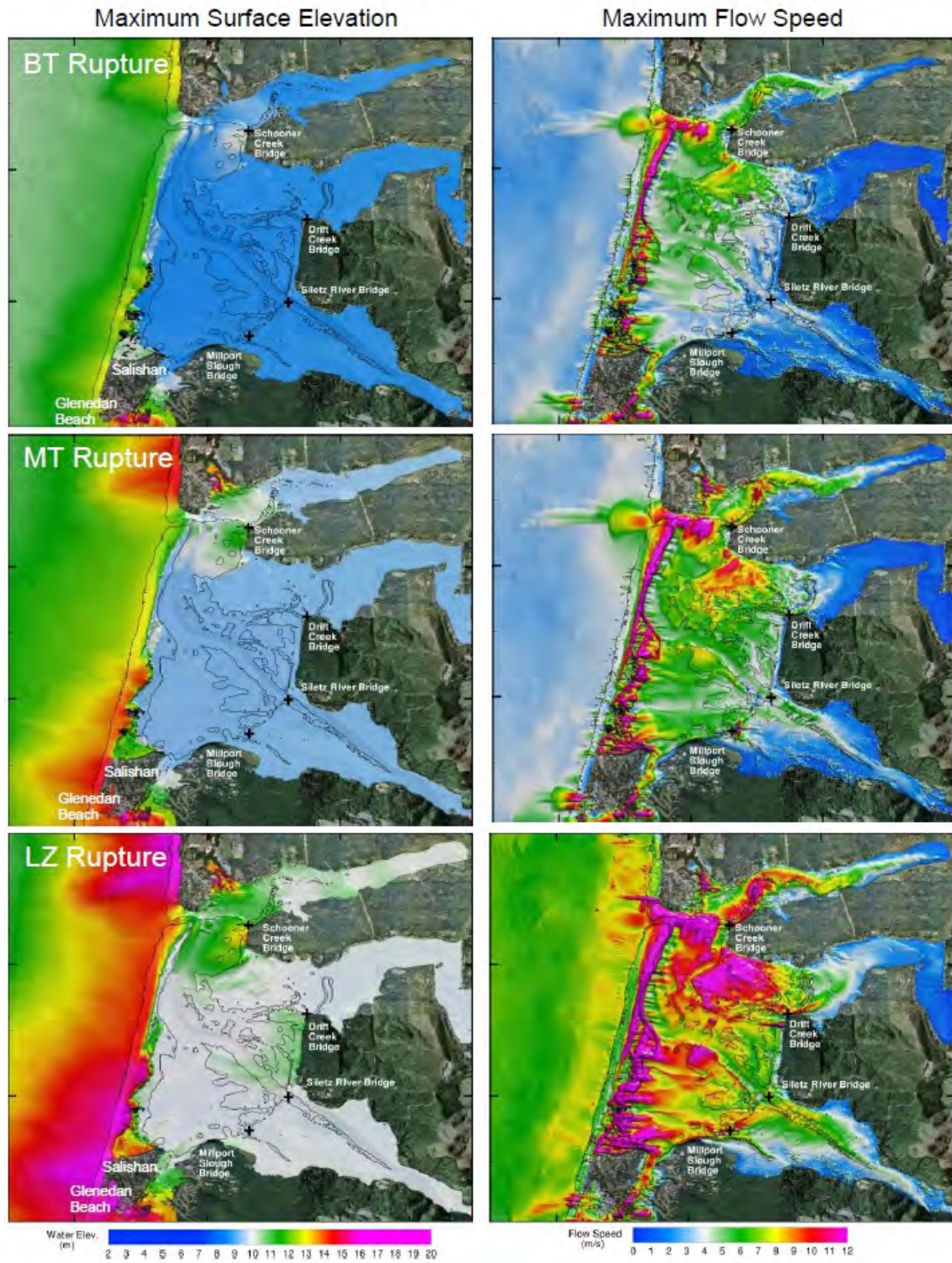


Figure F.9: Flow conditions at Siletz Bay for the BT, MT, and LZ ruptures at Mw 9.0.

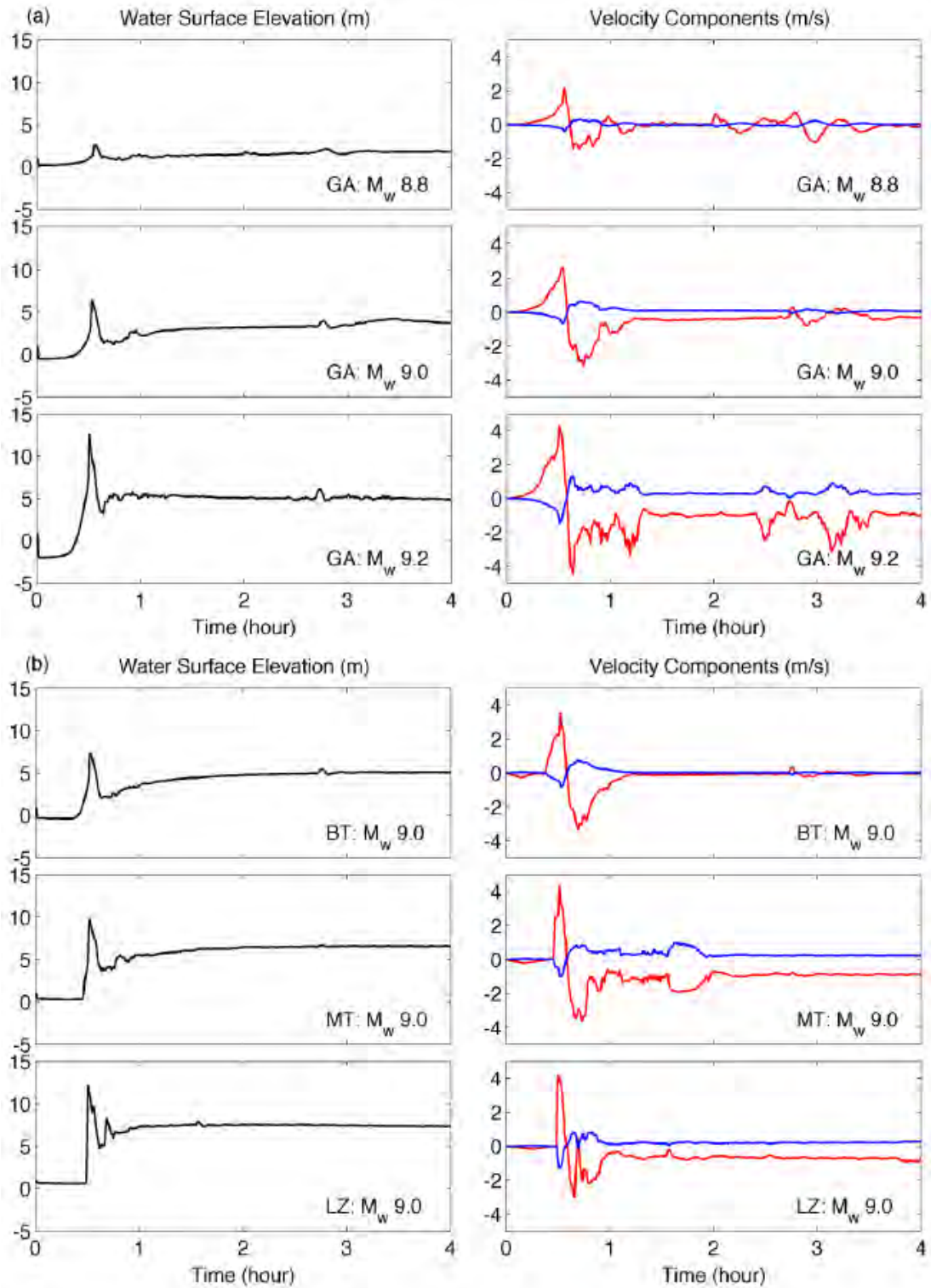


Figure F.10: Surface elevation and flow velocity at Schooner Creek Bridge. (a) GA rupture at Mw 8.8, 9.0, and 9.2. (b) BT, MT, and LZ ruptures at Mw 9.0. Red and blue lines indicate normal and tangential velocity components to the bridge.

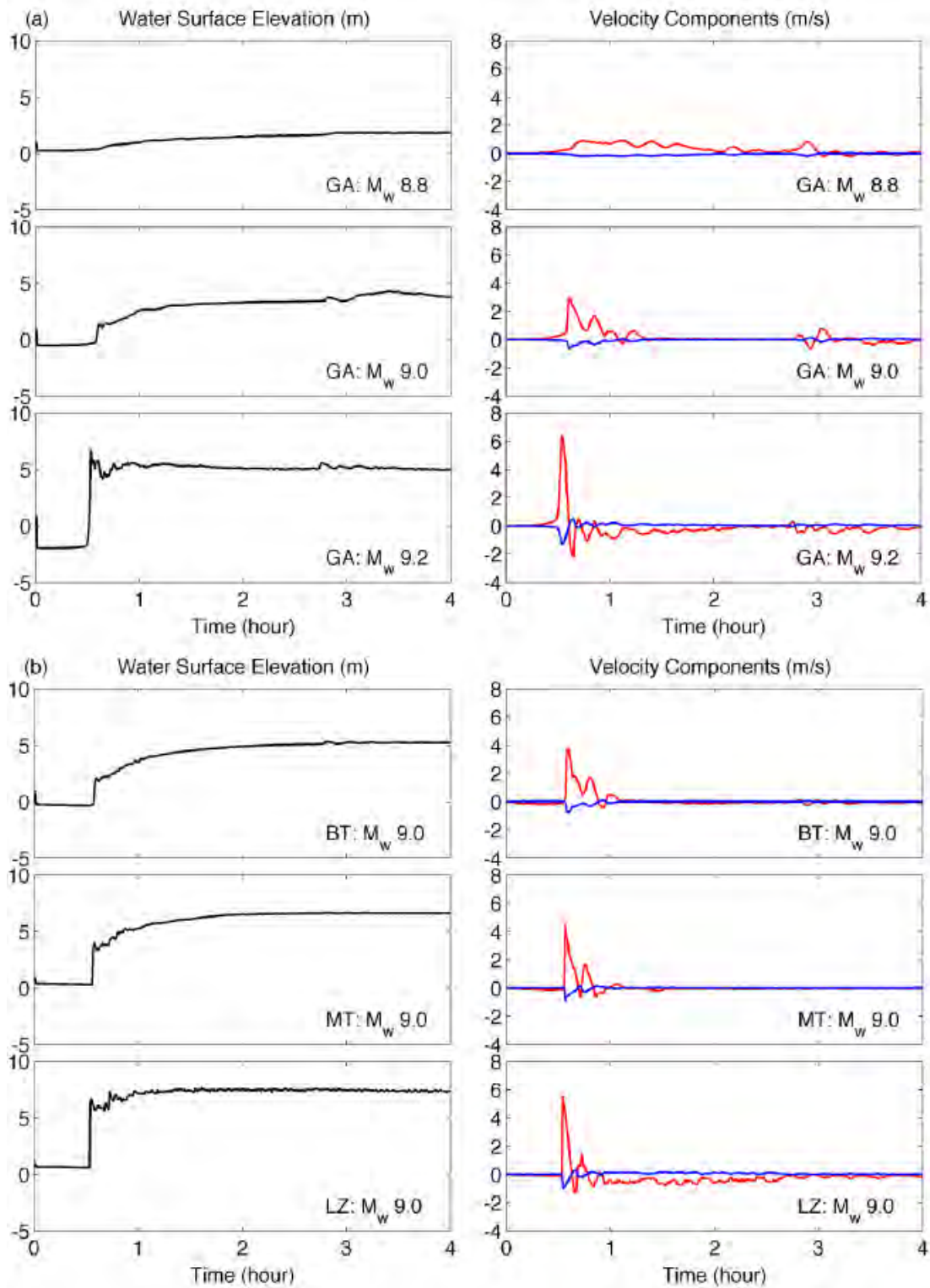


Figure F.11: Surface elevation and flow velocity at Drift Creek Bridge. (a) GA rupture at M_w 8.8, 9.0, and 9.2. (b) BT, MT, and LZ ruptures at M_w 9. Red and blue lines indicate normal and tangential velocity components to the bridge.

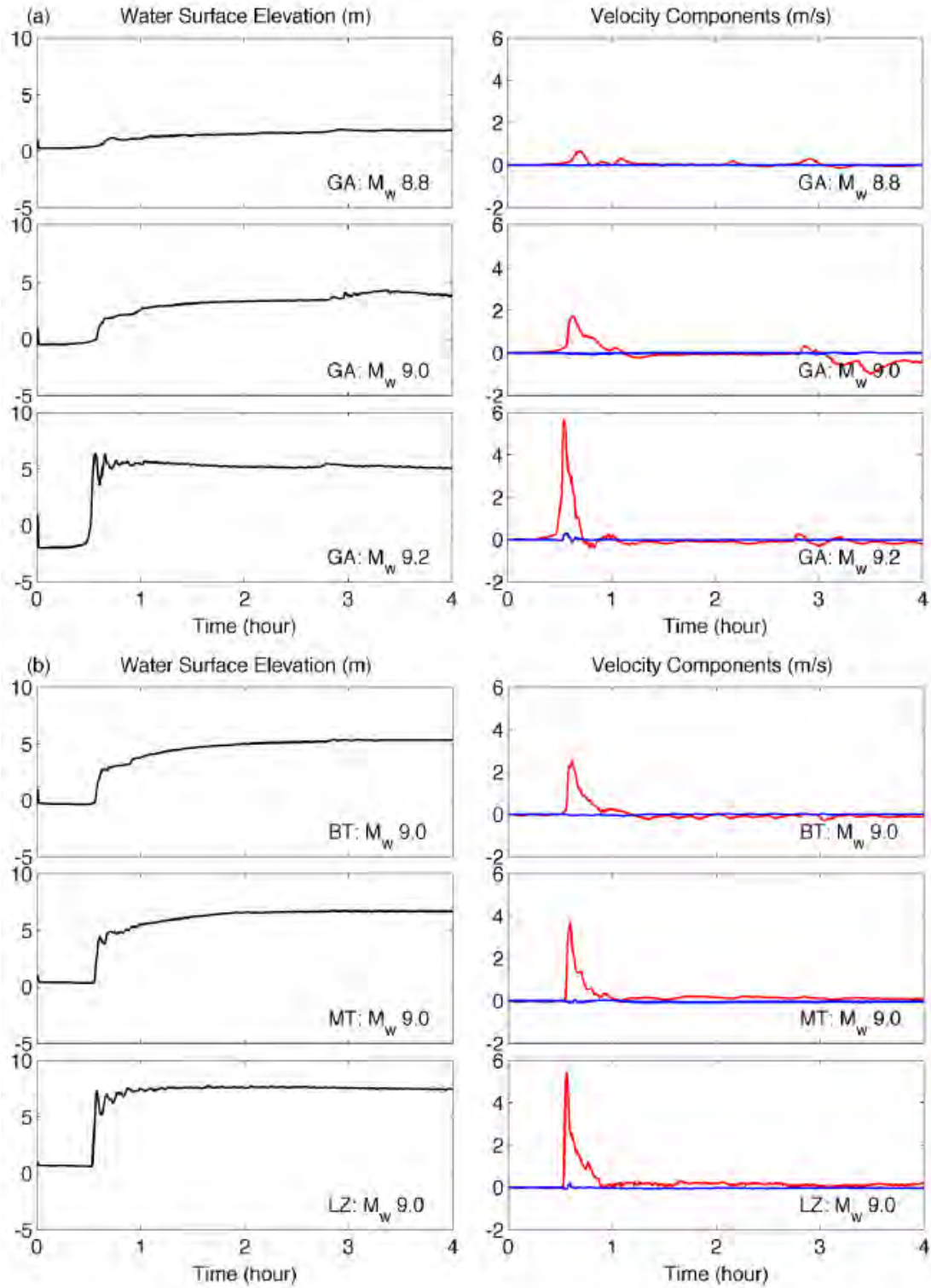


Figure F.12: Surface elevation and flow velocity at Siletz River Bridge. 564 (a) GA rupture at Mw 8.8, 9.0, and 9.2. (b) BT, MT, and LZ ruptures at Mw 9.0. Red and blue lines indicate normal and tangential velocity components to the bridge.

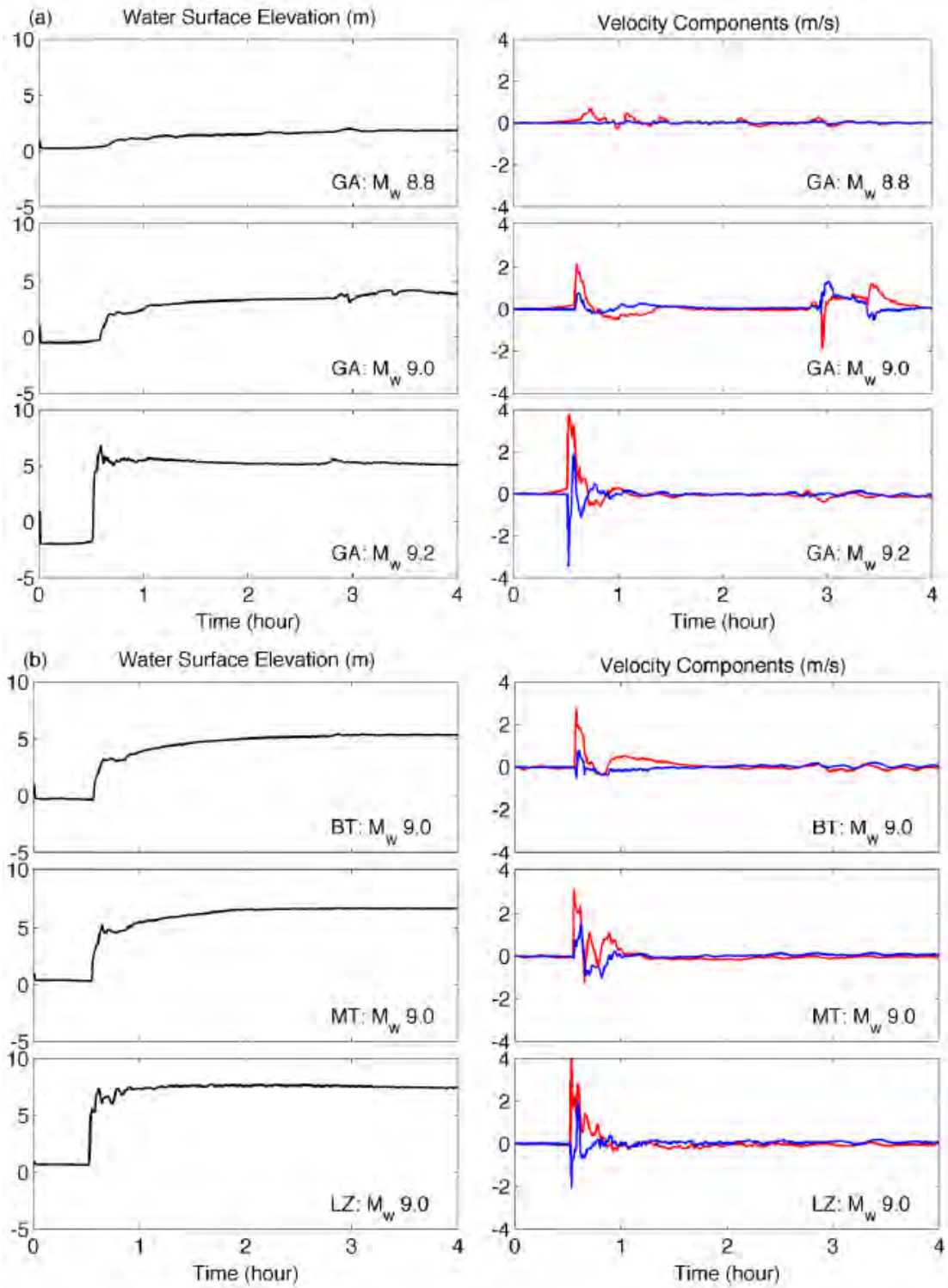


Figure F.13: Surface elevation and flow velocity at Millport Slough Bridge. (a) GA rupture at Mw 8.8, 9.0, and 9.2. (b) BT, MT, and LZ ruptures at Mw 9.0. Red and blue lines indicate normal and tangential velocity components to the bridge.